2012

FILM DEPOSITION AND MICROFABRICATION OF MAGNETIC TUNNEL JUNCTIONS WITH AN MgO BARRIER

Du, Yuqing

http://hdl.handle.net/10026.1/1174

http://dx.doi.org/10.24382/4190
University of Plymouth

FILM DEPOSITION AND MICROFABRICATION OF MAGNETIC TUNNEL JUNCTIONS WITH AN MgO BARRIER

by

Yuqing Du

A thesis submitted to the University of Plymouth

in partial fulfilment for the degree of

DOCTOR OF PHILOSOPHY

School of Computing and Mathematics

Faculty of Science and Technology

2012

Film deposition and microfabrication of magnetic tunnel junctions with an MgO barrier

Yuqing Du

Abstract

Magnetic tunnel junctions (MTJs), which consist of a thin insulation layer sandwiched by two ferromagnetic (FM) layers, are among the key devices of spintronics that have promising technological applications for computer hard disk drives, magnetic random access memory (MRAM) and other future spintronic devices. The work presented here is related to the development of relevant techniques for the preparation and characterization of magnetic films, exchanged biased systems and MTJs. The fabrication and characterization of PtMn/CoFe exchange biased systems and MTJs with Al-O barriers were undertaken when the new Aviza StratIon *fxP* ion beam deposition tool was developed by the project consortium funded by DTI MNT. After the Nordiko 9550 spintronic deposition tool was installed at Plymouth, the work focused on the development of MTJ multilayer stacks with layer structures of CoFeB/MgO/CoFe/IrMn and IrMn/CoFeB/MgO/CoFeB to achieve coherent tunneling with a crystalline MgO barrier. The film deposition, microfabrication, magnetic field annealing, microstructural and nano-scale characterization, magnetic and magneto-transport measurement for these devices have been systematically studied to achieve smooth interfaces and desired crystallographic textures and magnetic properties of layer stacks. Magnetoresistance (MR) of up to 200% was obtained from MTJs with a layer structure of Ta/CuN/Ta/CoFeB/MgO/CoFe/IrMn/Ta and a CuN bottom electrode. Enhanced exchange anisotropy from the bottom pinned IrMn/CoFeB stacks has been obtained, which demonstrated the possibility of fabricating MTJs with CoFeB as both the top and bottom FM electrodes with strong exchange bias. The origin of the enhanced exchange

bias field was studied by employing high resolution transmission electron microscopy (HRTEM) and x-ray magnetic circular dichroism (XMCD) to examine the mmicrostructure properties and element specific magnetic properties of the stacks. Results demonstrate that the enhanced exchange anisotropy in the IrMn/CoFeB system is closely associated with the increased uncompensated interfacial spins. MTJs with layered structures of IrMn/CoFeB/MgO/CoFeB were prepared based on this exchange bias system. However, further work is required for the optimisation of the (001) crystallographic textures of the CoFeB/MgO/CoFeB stack to achieve coherent tunneling.

Table of contents

List of Figures

List of Tables

Acknowledgements

This work would not have been possible without the support of a number of people. Thanks will go to the following persons:

I would firstly like to thank my supervisor and director of study, Professor Genhua Pan, for his help, support, generosity and ideas over the years. I would also like to thank the other two supervisors, Dr. Roy Moate and Dr. Zhengqi Lu for their valuable discussions and suggestions on my research work. I also thank Dr. Hendrik Ohldag from Stanford for XMCD measurements and valuable discussions, Dr. Amit Kohn and Dr. Andras Kovacs from Oxford for TEM work.

I would like to thank my friends and colleagues at CRIST for their help and inspiration. I thank Mr. Phil Brown and Mr. Nick Fry for their huge support on my research. I also thank to my fellow group members Mr. Yun Zhou, Mr. Anthony Dyson for their support and help. I had a really good time working with them.

I would also like to thank Mrs Carole Watson and Mrs Lucy Cheetham from the research office for their encouragement and support.

I am very grateful to the financial support from the DTI MNT grant (CHBS/004/00033C) and the University of Plymouth for partially supporting me during my PhD research.

Furthermore, I would like to thank my family and friends for their immeasurable support.

Thank all of you; this PhD would not have been possible without you.

Author's Declaration

At no time during the registration for the degree of Doctor of Philosophy has the author been registered for any other University award without prior agreement of the Graduate Committee.

This study was partially financed under the DTI MNT grant (CHBS/004/00033C) for "300-mm ready ion beam deposition system for spintronics and MRAM", Principal Investigator Professor Genhua Pan.

A programme of advanced study was undertaken, which included the extensive reading of literature relevant to the research project, training for the operation of research equipment & instrumentation, and for the writing of journal publications, and attendance at international conferences.

Word count of main body of thesis: (approximate) 29,384

Signed Yuqing Du

Date 22/08/2012

1 Introduction

1.1 Motivation

The magnetic tunnel junction (MTJ) is one of the key devices of spintronics with technological applications in computer hard disk drives, magnetic random access memory (MRAM) and other spintronic devices. Driven by the ever increasing demand for storage density in computer hard disk drives and MRAM technology, and by the requirement of new spintronic devices, there is always a constant need to develop new MTJ materials and layer structures for ever increasing tunnel magnetoresistance (TMR) and more robust process conditions for integration of MTJs on Si wafers. These in turn inspire the need for basic research to improve understanding of the science of the relevant physical phenomena associated with these devices. It is the purpose of this work to address these issues for the development of MTJ devices for technological applications. The challenges related to this have been identified and addressed. These include the development of basic film deposition process conditions for MTJs with an MgO barrier, new exchange bias multilayer stacks with enhanced exchange anisotropy, the understanding of the origin of the exchange bias phenomenon, CoFeB ferromagnetic (FM) layers with atomic smoothness and well defined textures, and the microfabrication techniques for these devices.

1.2 Thesis outline

The thesis is organised as follows.

Chapter 2 gives a brief introduction to the background knowledge of the relevant topics including ferromagnetism, MTJs, their theories and historical development and the exchange bias phenomenon. A review of the state-of-the-art is also given.

Chapter 3 presents the experimental techniques and research facilities employed for the work including thin film deposition techniques, magnetic field annealing, photolithography and ion milling, magnetic and magneto-transportation characterisation techniques.

Chapters 4 – 6 present detailed results obtained in this work including the DTI MNT project for the successful development of the world's first 300 mm IBD tool for MRAM and spintronics, in which the author contributed to the characterisation and microfabrication of films and devices, the enhanced exchange bias in IrMn/CoFeB systems and the results on MgO MTJs obtained from the Nordiko 9550 tool, which form the major achievements of the PhD work.

Finally, the conclusions drawn from the work are given in Chapter 7 together with some suggested future work.

2 Background

The possibility of using the spin degree of freedom of electrons to achieve faster and multifunctional electronic devices that consume less energy is a central concept of "spintronics". In recent years, there have been rapid developments in spintronics as it could provide a major breakthrough in technologies involving conventional electronics. The MTJ is one of the most important spintronic devices due to its significance in basic research as well as in industrial applications, such as non-volatile magnetic random access memories (MRAMs), hard disk drives and magnetic sensors. Basic concepts and theory about MTJ and exchange bias are introduced in this Chapter. Factors and process conditions for producing MTJs with high TMR are discussed and open issues related to the origin of exchange bias are also presented.

2.1 Magnetic tunnel junctions

An MTJ consists of three essential layers, i.e. a thin insulating layer (a tunnel barrier) sandwiched between two FM layers. The TMR of MTJs depends on the relative magnetic alignment of the two electrodes. When the magnetisations are parallel, the resistance is low, and when anti-parallel, the resistance is high. The ratio $(R_{AP} - R_P)/R_P$, defined as the TMR, is one of the most important parameters of an MTJ, where R_P and R_{AP} denote the resistance when the magnetisations of the two FM layers are parallel and anti-parallel, respectively. It would be appropriate to review the understanding of magnetism, spin polarization, tunneling effect and TMR before introducing the theory of MTJs. The historic development of MTJs is also given below.

2.1.1 Introduction to magnetism

Magnetism, which exists in all materials, is due to the orientation of the tiny magnetic moments in the material. These tiny magnetic moments are the sum of orbital magnetic

moments and spin magnetic moments of all the electrons in the atoms. Orbital magnetic moment arises from the motion of the electrons around the nucleus, which constitutes a current and gives a magnetic moment perpendicular to the orbit plane. Spin magnetic moment is created due to the intrinsic angular momentum of the electrons. The strength of the magnetism of a material is described by the magnetization M, which is defined as the magnetic moment per unit volume of a magnetic substance. When a material is placed in an external magnetic field M, there is an approximate linear relationship between M and H:

$$\vec{M} = \chi\vec{H} \tag{1}$$

Where χ is called magnetic susceptibility. Materials can be categorized into diamagnetic, paramagnetic, FM, anti-ferromagnetic (AFM) and ferrimagnetic materials according to the sign and order of magnitude of χ. For diamagnetic material, χ is negative and in the order of 10^{-5}, which is the contribution of the orbital magnetic moments. Diamagnetism exists in all substances. However, it is so weak that it is overwhelmed by paramagnetism or ferromagnetism in most cases. Paramagnetism, for which magnetization is proportional to the external field and the magnetic susceptibility is in the order of 10^{-3} to 10^{-5}, is due to the spin moments of unpaired electrons in the atoms or ions. These spin moments are isolated from each other and produce a very weak magnetization when placed in a magnetic field. When the external field is removed, because of thermal agitation, the magnetization will be zero. Although the order of magnitude of the magnetic susceptibility is quite small for diamagnets or paramagnets, their effect on the overall magnetic signal of samples with very thin FM layers may still be non-negligible. Therefore it is very important to select the right materials for the sample holder or sample rod when building highly sensitive magnetometers, such as a vibrating sample magnetometer (VSM).

For MTJs, we are mainly concerned with ferromagnetism and antiferromagnetism. In ferromagnets and antiferromagnets, the magnetic ordering is spontaneous since no external field is needed to introduce magnetization. According to Weiss's molecular field theory and Heisenberg's quantum mechanical exchange interaction theory[1; 2], the spontaneous magnetization in magnetic materials originates from the exchange interactions between the spin moment of unpaired electrons of the neighboring atoms, which produces an internal quantum mechanical force by which the individual atomic moments are aligned into a parallel or anti-parallel state, known as magnetic ordering. Fig. 2.1 shows two forms of magnetic ordering, i.e. (a) FM ordering and (b) AFM ordering.

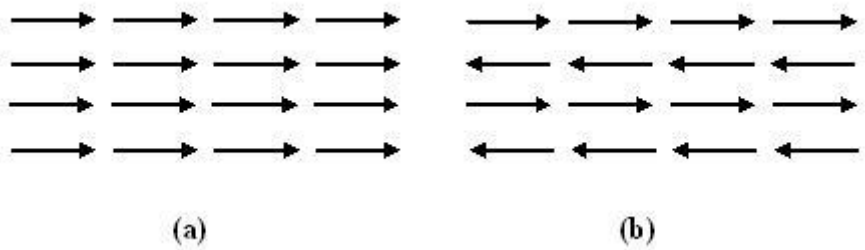

Fig. 2.1. Schematic illustrations of magnetic ordering. (a) The magnetic moments are aligned parallel in a FM material due to the strong positive exchange interactions between the spin moments. (b) The magnetic moments are aligned anti-parallel in an AFM material due to the strong negative exchange interactions between the spin moments.

In FM ordering, the spin moments of neighboring atoms align parallel with each other in small regions due to the strong positive exchange interactions, or FM coupling, as shown in Fig.2.1 (a). These regions are known as magnetic domains. Although the magnetic moments in a FM material are naturally aligned within each domain, it is possible that ferromagnetic material may exhibit no magnetization in the absence of a magnetic field due to the random orientations of the domain magnetizations. The magnitude of the magnetization of a single domain is called the spontaneous

magnetization, or saturation magnetization M_s. Above a critical temperature, the saturation magnetization vanishes due to the thermal effect. The critical temperature at which the saturation magnetization vanishes is called the Curie temperature (T_C).

In contrast to a ferromagnet, the coupling between the adjacent atomic moments in an antiferromagnet is negative and the spin moments of one layer are anti-parallel to those of its neighbors, as shown in Fig.2.1 (b), resulting in zero net magnetization. Above a certain temperature, known as Neel temperature (T_N), AFM ordering becomes random and the material becomes paramagnetic. One of the typical applications of AFM material is in an exchange biased system, which will be described in detail in Section 2.2.

A ferrimagnet can be viewed as a special antiferromagnet, where the spin moments in the neighboring atoms are aligned anti-parallel to each other due to the negative exchange interaction whilst the material has a net magnetization due to the unequal neighboring atomic moments.

The behavior of a FM material under an external applied magnetic field H can be described by a hysteresis loop or MH loop as shown in Fig.2.2. Starting from $H = 0$, the magnetisation of a FM material which has never been magnetized or demagnetized will follow the dashed line as H increases and reach saturation magnetization M_s, where the magnetizations of all the domains are aligned to the field direction ("a" in Fig. 2.2). Decreasing the applied field to zero, the magnetization remains non-zero in the material. The value of net magnetization at this point is called the remanent magnetization M_r, in which some of the domains remain aligned but some have lost their alignment. Reversing the magnetic field to point b, the magnetization reduces to zero. The value of

magnetic field needed to reduce the magnetization zero is called the coercivity H_c. As the field in the opposite direction increases in strength, the domains again become aligned and saturated in the opposite direction at point c. Reversing the field once more, the magnetisation will again reduce reaching point d where the applied field is H_c and the magnetism is zero once more. Typical examples of FM materials are Ni, Co, Fe and their alloys.

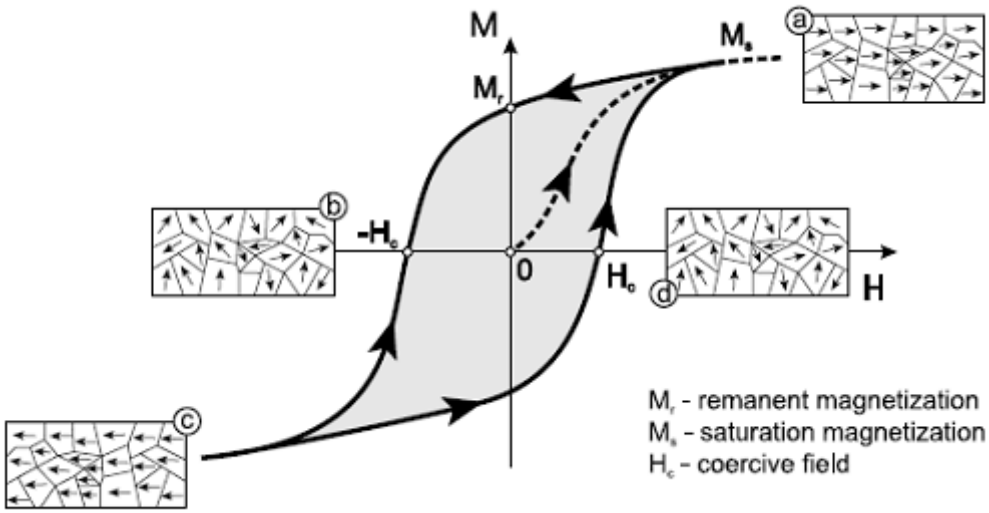

Fig. 2.2. Hysteresis loop of a FM material[3].

2.1.2 Ferromagnetism in transition 3d metals and spin polarization

Transition metals, Ni ($3d^8 4s^2$), Co ($3d^7 4s^2$) and Fe ($3d^6 4s^2$), have partially filled 3d bands. Fig. 2.3 is a schematic illustration of the density of states (DOS) diagram for the 3d bands the transition metals. All the electrons are filled up to the Fermi level E_F. Because of the exchange interactions, the two 3d sub-bands are split, resulting in an imbalanced number of spin-up and spin-down states. The number of states filled is shown by the shaded area in Fig. 2.3, denoted by $N_\uparrow$ and $N_\downarrow$ for the spin up and spin down sub-bands. Different metals have different number of empty and occupied states.

The difference in the number of spin up states and spin down states is responsible for the magnetic moments of the transition metals m, given by:

$$m = (N_{\uparrow} - N_{\downarrow})\mu_B \tag{2}$$

Where μ_B is the Bohr magnetron.

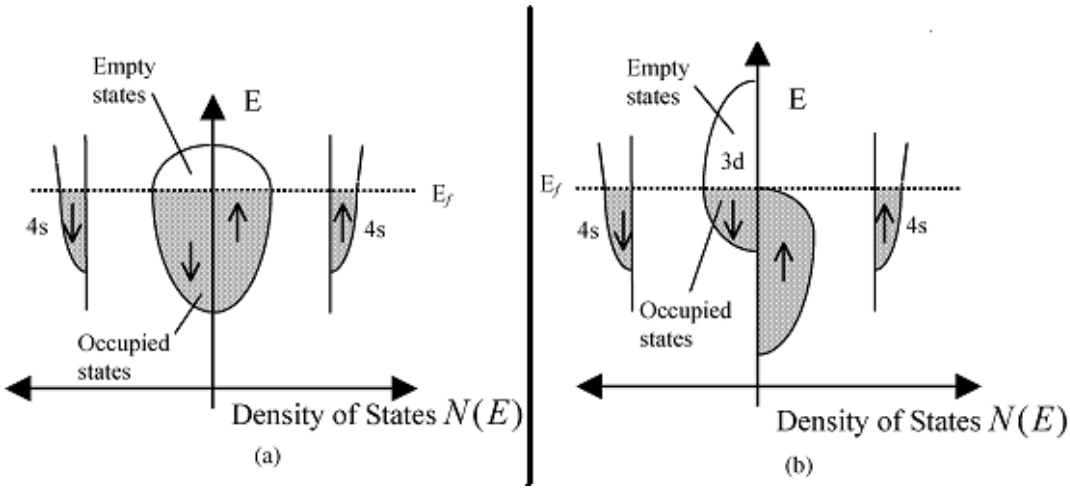

Fig. 2.3. Schematic illustrations of the electronic band diagrams[4], (a) before exchange interaction and (b) after exchange interaction. As a result of exchange interaction, the 3d band is split into two sub-bands with opposite spins. The Fermi level $E_F$is indicated by the dashed line.

The band theory usually predicts that the magnetic moments are non-integer values, which agrees with experiment data[5]. Fig. 2.4 shows the calculated complex band structure of Ni. It is clearly seen that it is unlikely to produce integer values for the magnet moments. The experimental values of FM moments per atom are [6]: Ni, 0.6 μ_B ; Co, 1.72 μ_B ; and Fe, 2.2 μ_B .

The split of the 3d bands also introduces spin polarization for the FM metals, which is an important parameter in TMR. Spin polarization P is defined as the spin asymmetry in the DOS at E_F:

$$P = \frac{N_{\uparrow}(E_F) - N_{\downarrow}(E_F)}{N_{\uparrow}(E_F) + N_{\downarrow}(E_F)} \tag{3}$$

Although there is a good agreement between experimental values and calculated data for the magnetic moments, there is significant discrepancy in experimental measurement and theory prediction for the polarization. The spin polarization of a FM material at low temperature can be directly measured using FM/Al-O tunnel junctions [7]. The spin polarizations of Ni, Co and Fe are always positive and usually between 0 and 0.6 at temperatures below 4.2 K measured in this way [8]. However, the theoretical prediction, even the sign of spin polarization, differs from the experimental results. For example, according to the band structure of Co and Ni, spin polarizations for both metals are negative. As noticed in the calculated band structure of Ni in Fig. 2.4, $N_{\downarrow}$ outnumbers $N_{\uparrow}$ at E_F, which will result in a negative spin polarization according to Equation (3). This discrepancy between experiment and theory, one of the most fundamental questions with regard to the TMR effect, will be discussed in Section 2.1.

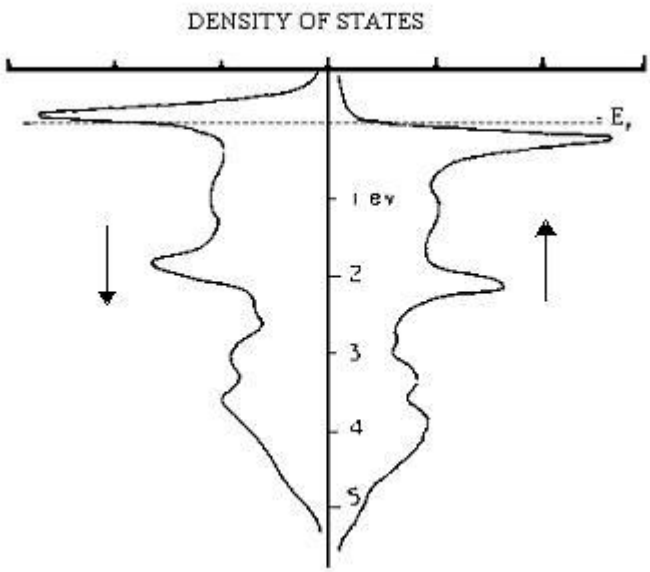

Fig. 2.4. Calculated band structure of Ni[9].

2.1.3 Tunneling effect

The tunneling effect is a quantum mechanical effect that means an electron can transmit through a barrier that is higher than its kinetic energy. This phenomenon cannot be explained by classical physics. According to quantum mechanics, considering the wave properties of the electron, there is a possibility that the wave can transmit through the barrier. In the following, the tunneling effect is illustrated by the possibility of having an electric current flow through a thin insulating layer between two metals. A number of assumptions to simplify the problem are considered where the metals are identical and have perfect interfaces. Fig. 2.5 shows the rectangular barrier describing the metal-insulator-metal situation. Electrons with energy of $E < V_0$ travel along x in the rectangular barrier:

$$V(x) = \begin{cases} V_0, & 0 \leq x \leq a \\ 0, & x < 0, x > a \end{cases} \tag{4}$$

where V_0 is the energy height of the barrier.

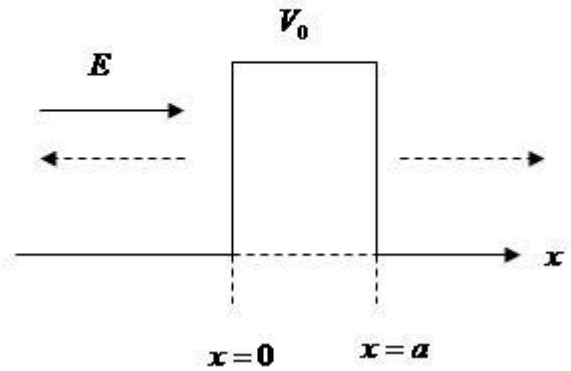

Fig. 2.5. Rectangular tunneling barrier.

By solving the time independent one dimensional Schrődinger equation:

$$E\psi(x) = \left[-\frac{\hbar^2}{2m}\nabla^2 + \mathrm{V}_0\right]\psi(x) \tag{5}$$

Where $\hbar = h/2\pi$, h is Planck's constant and m is the mass of the particle. The solutions are:

$$\psi(x) = \begin{cases} Ae^{ik_1x} + Be^{-ik_1x}, & (x \leq 0) \\ Ce^{ik_2x} + De^{-ik_2x}, & (0 \leq x \leq a) \\ Fe^{ik_1x}, & (x \geq a) \end{cases} \tag{6}$$

Where k_1 and k_2 are the wave numbers with $k_1 = \sqrt{2mE/\hbar^2}$ and $k_2 = \sqrt{2m(V_0 - E)/\hbar^2}$. In the area of $x \leq 0$, both incident wave Ae^{ik_1x} and reflected wave Be^{-ik_1x} exist, while in the area of $x \geq a$, only the transmitted wave Fe^{ik_1x} exists. Due to the conditions that exist at the boundaries of the barrier, both the wave functions and their differentials must be continuous, the constants B, C, D and F are found to be correlated to A. The ratio of the transmitted current density $|F|^2$ to the incident current density $|A|^2$ is defined as the transmission coefficient :

$$T = \frac{|F|^2}{|A|^2} = \frac{4{k_1}^2{k_2}^2}{({k_1}^2 + {k_2}^2)^2 sin^2 k_2 a + 4k_1k_2} \approx \frac{16E(V_0 - E)}{{V_0}^2} e^{-\frac{2a}{\hbar}\sqrt{2m(V_0 - E)}} \tag{7}$$

It can be seen that the incident electron can be transmitted despite the barrier height exceeding its energy, and the transmission T is dependent on the barrier width α, $(V_0 - E)$, incident particle mass m, decreasing exponentially as α increases.

2.1.4 MTJ and its historical development

In this section, an introduction to the concept of MTJs and the TMR effect will be given, followed by a brief account of the historical development of MTJs from metal-insulator-superconductor (MIS), superconductor-insulator-superconductor (SIS), superconductor-insulator-ferromagnet (SIF) junctions to ferromagnet-insulator-ferromagnet MTJs. Recent development of MTJs with amorphous Al-O and crystalline MgO barriers are also reviewed.

2.1.4.1 The TMR effect

An MTJ consists of a thin insulating layer (a tunnel barrier, normally Al-O or MgO) sandwiched by two FM layers. The two FM layers are designed in a way that the switching field for each FM layer is different, which means that H_c for each FM layer is different. The one with a lower or smaller H_c is called the soft layer (or free layer) and the other one with a higher or larger H_c is called the hard layer (or pinned layer if the exchange bias effect is used). There are several methods of producing H_c for the two FM layers. One is to choose different FM materials with different H_c. The second is to utilize different shape anisotropy for the same FM layer but with different thicknesses or shapes. Considering practical applications in the electronic industry, the most effective way to get a well defined switching at a low field is to fix (or pin) the magnetization of one of the FM layers by exchange bias provided by an adjacent AFM layer. The unpinned FM layer is called the free layer and the exchange-biased layer is called the pinned layer, as shown in Fig.2.6. This exchange bias phenomenon in an AFM/FM bilayer system will be fully discussed in Section 2.2. A typical dependence of the magnetization alignments of the free layer and pinned layer on the applied field is shown in Fig.2.7 (a), where there are two hysteresis loops: the one around zero field is the contribution from the free layer and the one around H_{ex} is the contribution of the

pinned layer due to the exchange bias effect. H_{ex} is the exchange bias field produced in the AFM/FM bilayer system.

The dependent resistance of an MTJ on the relative magnetic alignment of the pinned layer and free layer is shown in Fig.2.7 (b). When the magnetizations of the two FM layers are parallel, the MTJ is in a low resistance state and when the magnetizations are anti-parallel, the MTJ is in a high resistance state. The TMR is defined by Equation (8).

$$TMR = \frac{R_{AP} - R_P}{R_P} \tag{8}$$

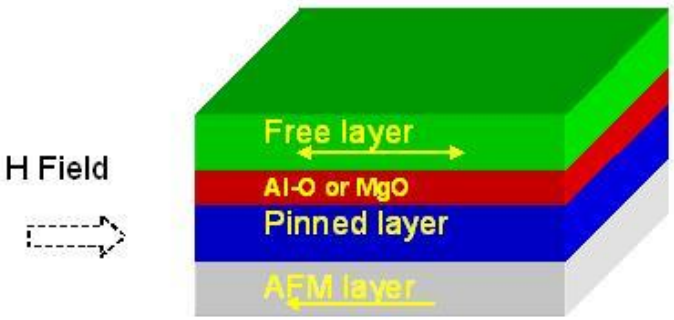

Fig. 2.6. Schematic illustration of MTJ consisting of free layer/Al-O or MgO/pinned layer pinned by an AFM layer.

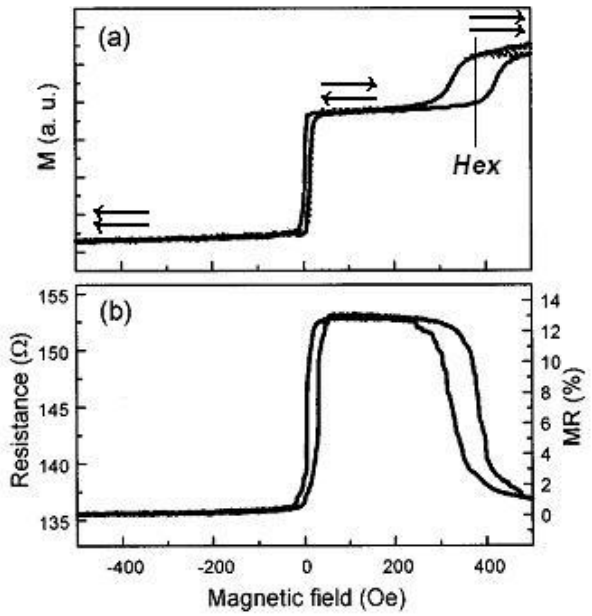

Fig. 2.7. (a)MH loop illustration of MTJ with free layer/Al-O/pinned layer pinned by AFM layer; (b) the field dependence of tunnel resistance of MTJ [10].

2.1.4.2 The historical development of MTJs

The history of MTJs can be dated back to 1960 when Giaever [11] found that electrons could tunnel between a metal and a superconductor through a thin Al_2O_3 barrier. As explained in Section 2.1.3, an electron tunneling through a barrier is a quantum mechanical phenomenon. When two metal electrodes are separated by a thin insulating barrier, there is a finite probability that an electron with energy E in one electrode to appear in the available energy states in the other. In 1962, Josephson junctions were proposed, in which super-current tunneling was observed between two superconductor electrodes separated by a thin Al-O barrier [12]. Josephson junctions are the basis for the superconductor quantum interference device (SQUID), which is still the most sensitive magnetometer and can be used to detect extremely small magnetic fields [13]. Spin dependent tunneling was discovered in 1971 by Tedrow and Meservey [14] in ferromagnet-insulator-superconductor Ni/Al-O/SC junctions. The technique has been widely used for measurement of spin polarization of FM materials [15; 16].

The first TMR effect was first observed in 1975 by Julliere [17] in a Fe/Ge/Co MTJ. The samples were oxidized at room temperature in dry oxygen after semiconductor Ge deposition to prevent shorting due to the pinholes in the Ge film. For this reason, some researchers [18; 19] would like to use Fe/oxidized Ge/Co when citing Juliere's work. A TMR ratio of 14% was observed at 4.2 K. Twenty years later in 1995, Miyazaki *et al* [20] and Moodera *et al* [21] independently observed TMR ratio as high as 18% at room temperature in FM/Al_2O_3/FM junctions. This development sparked great interest in these devices. Further advances in MTJ structures were enabled by optimizing the FM materials and the deposition conditions for the amorphous Al-O barrier. A TMR ratio for Al-O MTJs of 70% [22] have been obtained by introducing a CoFeB amorphous FM layer. MTJs with a crystalline MgO tunnel barrier were predicted by the first-principle calculations to give MR ratio in excess of 1000% in 2001[23; 24]. In 2004, room temperature MR ratio of 180% was first observed by Yuasa *et al* [25] for Fe/MgO/Fe with a crystalline MgO (001) barrier. In 2005, a TMR of 230% was obtained in CoFeB/MgO/CoFeB MTJs by Djayaprawira *et al* [26], followed by ones of 361%, 472% and 604% obtained by Lee *et al* [27] in 2006, Ikeda *et al* [28; 29] in 2007 and 2008, respectively. The huge TMR in CoFeB/MgO/CoFeB is of great significance not only for device applications but also for clarifying the physics of spin tunneling. In the following section, a review of theoretical background for Al-O and MgO MTJs will be presented.

2.1.5 Theory of magnetic tunneling

2.1.5.1 Julliere model

When the TMR effect was first observed by Julliere in 1975, a simple phenomenological model was proposed at the same time based on two assumptions. The first assumption is that the spin is conserved during tunneling and the tunneling processes of spin up and spin down electrons are independent. According to Julliere, the

conduction electrons can only tunnel to the energy band with the same spins when a voltage is applied between the two electrodes FM1 and FM2 as shown in Fig. 2.8. In the case of parallel alignment of the two FM electrodes, spin up electrons tunnel through the barrier from the majority band of FM1 to the majority band of FM2, and spin down electrons, from the minority band of FM1 to the minority band of FM2. In the case of antiparallel alignment, spin up electrons from the majority band of FM1 through the barrier to the minority band of FM2, and spin down electrons from the minority band of FM1 to the majority band of FM2. The second assumption is that tunneling conductance ($\sigma_{\uparrow\uparrow}$ and $\sigma_{\uparrow\downarrow}$) for each spin configuration is proportional to the product of the corresponding DOS in the two FM electrodes at E_F, i.e. $N_{i\uparrow}(E)$ and $N_{i\downarrow}(E)$:

$$\sigma_{\uparrow\uparrow} \propto N_{1\uparrow}(E_F)N_{2\uparrow}(E_F) + N_{1\downarrow}(E_F)N_{2\downarrow}(E_F) \tag{9}$$

$$\sigma_{\uparrow\downarrow} \propto N_{1\uparrow}(E_F)N_{2\downarrow}(E_F) + N_{1\downarrow}(E_F)N_{2\uparrow}(E_F) \tag{10}$$

The TMR is thus given by

$$TMR = \frac{(\sigma_{\uparrow\uparrow} - \sigma_{\uparrow\downarrow})}{\sigma_{\uparrow\downarrow}} = \frac{[N_{1\uparrow}(E_F) - N_{1\downarrow}(E_F)][N_{2\uparrow}(E_F) - N_{2\downarrow}(E_F)]}{N_{1\uparrow}(E_F)N_{2\downarrow}(E_F) + N_{1\downarrow}(E_F)N_{2\uparrow}(E_F)} = \frac{2P_1P_2}{1 - P_1P_2} \tag{11}$$

Where P_1 and P_2 are the spin polarization for FM_1 and FM_2, respectively. P is calculated from the spin dependent DOS at E_F as defined in Equation (3):

$$P_i = \frac{N_{i\uparrow}(E_F) - N_{i\downarrow}(E_F)}{N_{i\uparrow}(E_F) + N_{i\downarrow}(E_F)}, i = 1, 2$$

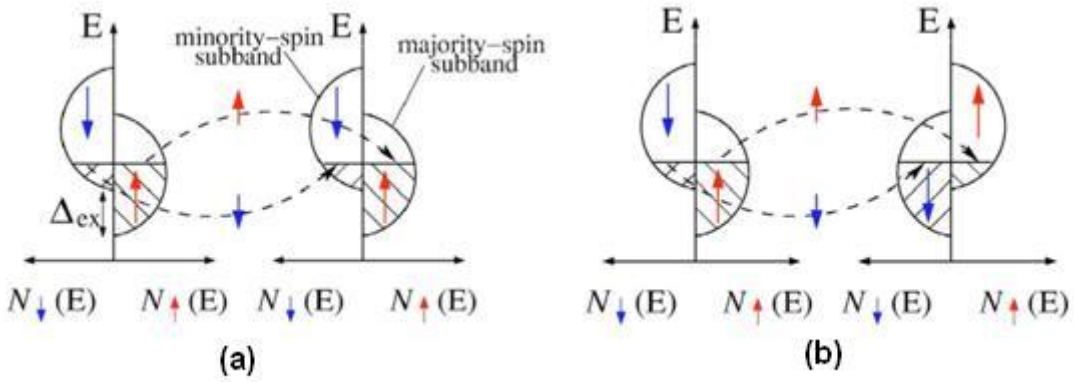

Fig. 2.8. Schematic illustration of spin dependent tunneling in an MTJ: (a) parallel and (b) antiparallel alignment of the two FM electrons.

Equation (11) indicates that TMR depends on the polarization of the FM layers. Spin polarization is an intrinsic property for FM material. When the material is nonmagnetic, $P = 0$. When the material is a half metal, which is fully spin polarized, $|P| = 1$. According to Equation (11), higher spin polarization materials will give higher TMR and if half metals are used, there will be indefinite TMR. Very high TMR have been obtained from MTJs with half metals at low temperatures [30; 31]. However, a high TMR at room temperature for MTJ with half metal electrodes has never been observed yet.

Julliere's model is an approximate description of the TMR effect. The 70% TMR for MTJs with 3d FM alloy electrodes is close to the Julliere limit estimated from experimental values of the spin polarization. However, the model cannot explain the ultra-high value of TMR in MTJs with MgO barriers. This is due to the fact that the Julliere model does not consider the effect of the tunnel barrier on the TMR.

2.1.5.2 Incoherent and coherent tunneling

Julliere's model focuses on the effect of the spin polarization or the DOS of the FM electrodes on the TMR, but that of the tunneling barrier has been neglected. Although

this approach is effective for explaining the TMR effect in MTJs with amorphous barrier layers, it is inadequate for understanding tunneling via a crystalline MgO barrier. According to recent theory[23; 24], the properties of both FM electrodes and the barrier are important in determining the tunneling conductance and thus the TMR ratio of MTJs. There exist two tunneling mechanisms – coherent and incoherent tunneling. Coherent tunneling occurs in MTJs with a crystalline MgO barrier and incoherent tunneling, in MTJs with an amorphous Al-O barrier.

Before discussing the tunneling mechanisms in detail, it is necessary to introduce the crystalline structure of 3d FM electrodes and their Bloch states (or wave functions) Δ_1, Δ_2 and Δ_5 as well as their crystalline symmetries. The wave functions of the conduction electrons in a periodic potential (crystalline structure) can be expressed by Bloch functions, for example in a one-dimensional periodic potential $(x) = V(x + na)$, where n is an integer and a is the periodic length, the wave function can be expressed as:

$$\varphi(x) = \sum_k A_k \, \phi_k(x) = \sum_k A_k \, e^{ikx} \mu_k(x) \qquad (12)$$

where A_k are constants;

$$\phi_k(x) = e^{ikx} \mu_k(x) \qquad (13)$$

$\phi_k(x)$ is a Bloch function with μ_k a periodic function having the same periodicity as the periodic potential $\mu_k(x) = \mu_k(x + na)$; k is the Bloch function wave vector. From Equation (12), we can see that both k and $k + 2n\pi/a$ satisfy this equation, so one only needs to consider the wave vectors within $\left[-\frac{\pi}{a}, \frac{\pi}{a}\right]$, which is called the first Brillouin zone in k space. This is a consequence of the translation a symmetry of the crystal.

The above results can be easily generalized to three dimensions. Fig.2.9 shows the first Brillouin zone of a body-centered cubic (bcc) lattice and the high symmetries points and lines. The centre of the Brillouin zone is always denoted by Γ; the high symmetry points and lines inside the Brillouin zone by Greek letters (Γ, Λ, Δ and Σ) and the points on the surface of the Brillouin zone by Roman letters (N, P and H). The points with high symmetry, called critical points[32], are tabulated in Table 2.1 for a simple cube (sc), face-centered cubic (fcc), bcc and hexagonal crystal lattices.

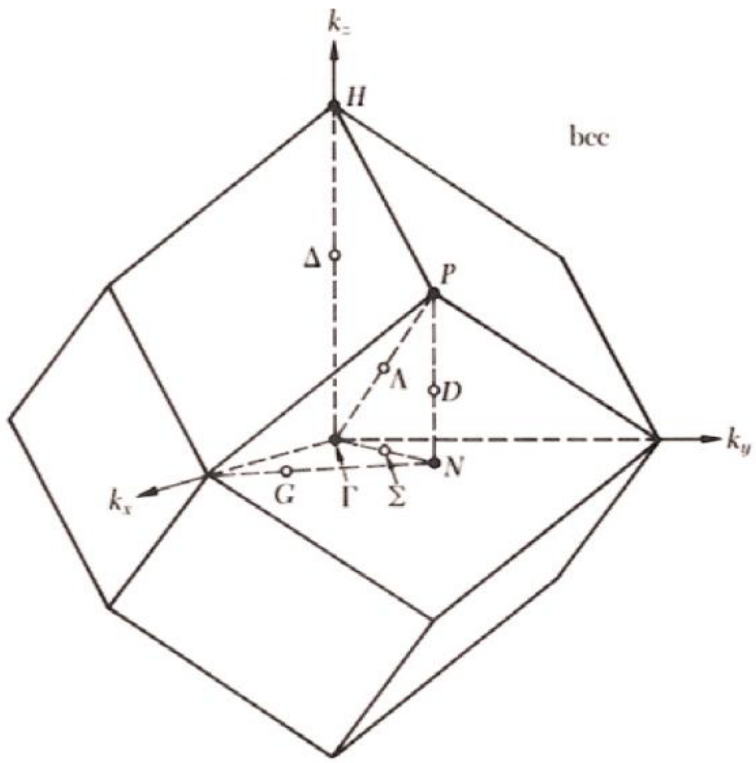

Fig. 2.9. First Brillouin zone for bcc lattice crystal structure[6]. Spatial high-symmetry points are denoted by Γ, *N*, *P* and *H*; high symmetry lines joining some of the points are labelled as Λ, Δ and Σ.

$\Gamma \underset{\Lambda}{\rightarrow} P$; $\Gamma \underset{\Delta}{\rightarrow} H$ and $\Gamma \underset{\Sigma}{\rightarrow} N$ respectively refer to the three high–symmetry directions [111], [100] and [110] in the Brillouin zone of the bcc lattice. The Brillouin zone is highly symmetric and it is unchanged by certain operations. The symmetry of the Brillouin zone is caused by the symmetry of the lattice and it is therefore related to the symmetry of the crystals.

The symmetries of the Bloch function are closely related to the symmetries of the crystal structure. For bcc Fe (001), there exist Bloch states with symmetries Δ_1 (spd hybridized states), Δ_2 (d states) and Δ_5 (pd hybridized states) in the direction of [100]. Bloch states with Δ_1 symmetry are largely positive spin polarized and Bloch states with Δ_2 are negatively polarized at E_F .

Symbol	**Description**
Γ	Centre of the Brillouin zone
Simple cube (sc)	
M	Center of an edge
R	Corner point
X	Centre of a face
Face-centered cubic (fcc)	
K	Middle of an edge joining two hexagon faces
L	Centre of a hexagonal face
U	Middle of an edge joining a hexagonal and a square face
W	Corner point
X	Centre of a square face
Body-centered cubic (bcc)	
H	Corner point joining four edges
N	Centre of a face
P	Corner point joining three edges
Hexagonal	
A	Centre of a hexagonal face

H	Corner point
K	Middle of an edge joining two rectangular faces
L	Middle of an edge joining a hexagonal and a rectangular face
M	Centre of a rectangular face

Table 2.1. Symbols for the high symmetry points for the Brillouin zone for simple cube (sc), face-centered cubic (fcc), bcc and hexagonal lattices.

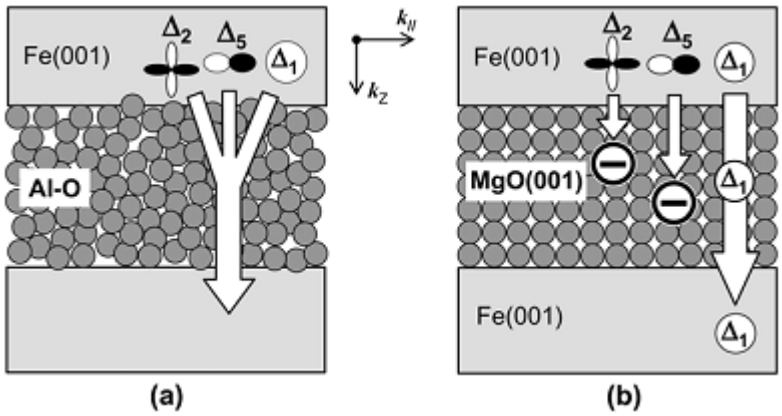

Fig. 2.10. Schematic illustrations of electron tunneling through (a) an amorphous Al-O barrier and (b) a crystalline MgO (0 0 1) barrier[33].

Fig.2.10 is a schematic illustration of the two different tunnel mechanisms in MTJs with Al-O barrier (a) and with MgO barrier (b). For MTJ with an amorphous Al-O barrier, Bloch states with different symmetries Δ_1 , Δ_2 and Δ_5 exist in the top electrode layer Fe (0 0 1) in $k_{\parallel} = 0$ direction. Because the tunnel barrier Al-O is amorphous and there is no crystallographic symmetry, tunneling through the barrier is incoherent, which means all the Bloch states with various symmetries can tunnel through the barrier. As discussed in Section 2.1.3, the measured spin polarization for Ni and Co using an Al-O barrier is positive[7; 8], contradicting the negative values predicted by theoretical calculations. This means that the tunneling probability is different for Bloch states with different symmetries. The Δ_1 Bloch states with larger positive spin polarization are thought to have higher tunneling probability than other Bloch states such as Δ_2 and

Δ_5[34; 35], which results in a net positive polarization for the electrodes. Due to the Bloch states with negative polarization, such as Δ_2, also contributing to the tunneling current, the net spin polarization of the electrode and TMR are reduced.

The situation is very different in the case of MTJs with a crystalline barrier as shown in Fig.2.10 (b), where there exist three types of evanescent states in the crystalline MgO (0 0 1) barrier i.e. Δ_1, Δ_2 and Δ_5, in the same $k_{\parallel} = 0$ direction. Tunneling through the barrier is coherent in this case, i.e., each Bloch state in the top electrode can only tunnel through the MgO barrier via the corresponding evanescent states with the same crystalline symmetry. As shown in Fig. 2.10 (b), because the Δ_1 evanescent states have the longest decay length (see below for more detail)[24], tunneling via Δ_1 becomes the dominant channel and tunneling via the other states is suppressed.

The effect of coherent tunneling on TMR can be further understood by Fig. 2.11[24], which shows the calculated tunneling DOS of Bloch states across the interfaces of an Fe(100)/MgO(001)/Fe(001) MTJ. The upper panels (a) and (b) show the tunneling DOS for the parallel magnetic alignment where the electrons tunnel from the majority bands to the majority bands and from the minority bands to the minority bands. In the case of antiparallel alignment, the electrons tunnel from the majority bands to the minority bands and from the minority bands to the majority bands, as shown in the lower panels (c) and (d). As stated previously, the Δ_1 Bloch states of Fe (001) are positively spin polarized, therefore they exist only in the majority bands. It can be seen from panels (a) and (c) that the Δ_1 states have the lowest decay rate in the MgO barrier in both magnetic configurations. The other states Δ_2 and Δ_5 all decay more quickly thanΔ_1. This suggests that $\Delta_1$is the dominant tunneling channel and the electron tunneling via other Bloch states is suppressed in the coherent tunneling. It is also worth noting that although in

both magnetic configurations the Δ_1 tunneling dominates, the tunneling probabilities of Δ_1 states are much higher in the parallel configuration than that in the antiparallel configuration. This results in a very high tunnel conductance for majority spin in the parallel configuration and very low tunnel conductance in the antiparallel configuration. The fact that the tunneling conductance in the parallel state is much higher than that in the antiparallel state makes the TMR ratio in coherent tunneling very large, and is known as giant TMR.

Another important point to note is that although the net spin polarization of Fe is small because both majority and minority spin bands having various Bloch states at E_F with positive or negative spin polarization; the Fe Δ_1 band is fully spin polarized at E_F ($P = 1$). Thus a very large TMR effect in Fe (001)/MgO (001)/Fe (001) is possible even if the net spin polarization is not unity. This applies to other transition metals and their alloys as well, such as Co, CoFe and CoFeB because the $\Delta_1$states in these materials at E_F are also fully spin polarized.

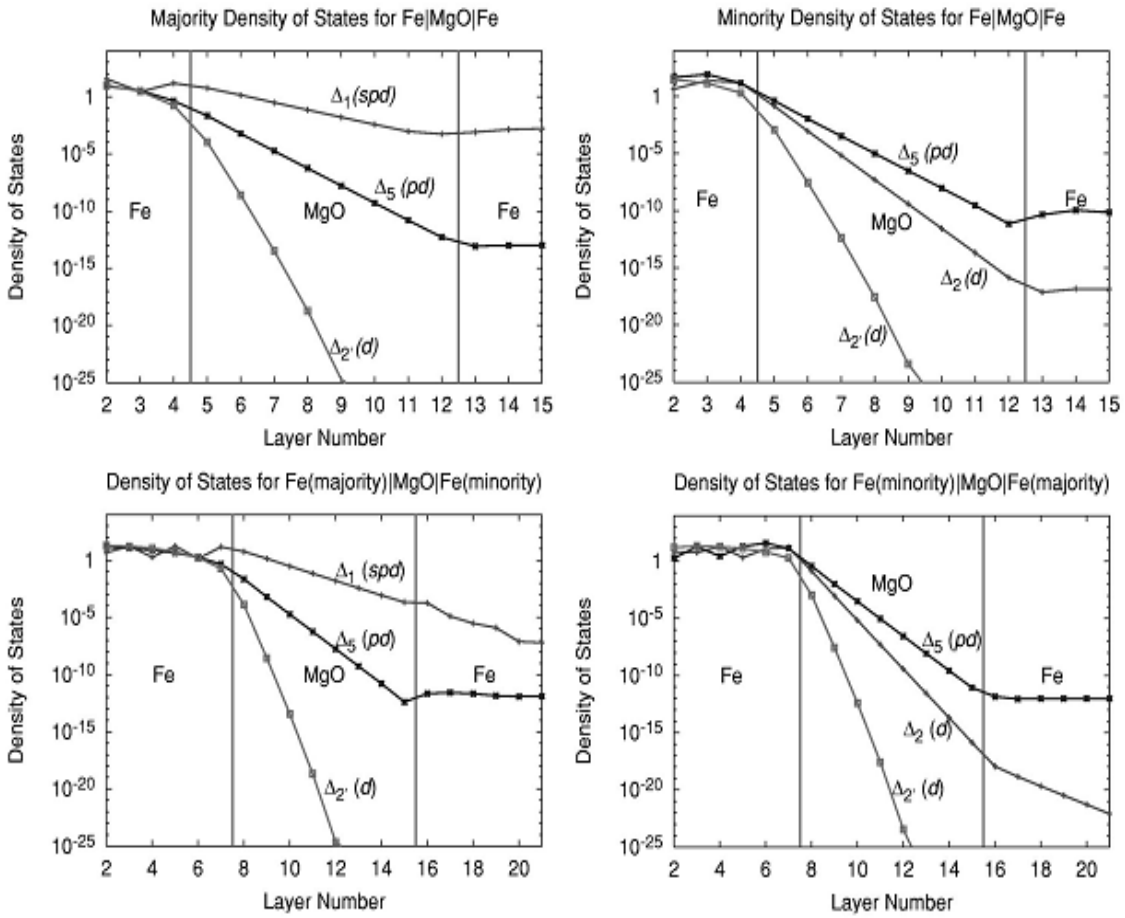

Fig. 2.11. Tunneling DOS for Fe(100)/MgO/Fe(100) for parallel alignment of magnetizations majority (a), minority (b), and antiparallel alignment of magnetizations (c) and (d)[24].

2.1.6 Requirements for MTJs with giant TMR

It is clear from the above discussion that MTJs with giant TMR can be obtained if the Δ_1 states in the FM electrodes are fully spin polarized at E_F and the Δ_1 states become the dominant tunneling channel. The first condition can be met by using FM electrode materials such as Co, Fe, CoFe and CoFeB, or Heusler alloys. The key to meeting the second condition is to make the FM/MgO/FM tunnel stack with (001) crystalline orientation. This needs to be achieved via the optimization of process conditions for film deposition and magnetic field annealing. For example, CoFeB is amorphous in an as-deposited state; it can be crystallized into the bcc (001) orientation after magnetic field annealing depending on the thickness and composition of the CoFeB[36], and the

crystal orientation of adjacent layers[27]. The formation of (001) oriented MgO is also affected by the adjacent FM layer[28].

The interfaces between the FM metal and the tunneling barrier should be clean and atomically flat so that the Δ_1 Bloch states in the FM electrodes can effectively couple with Δ_1 states in the tunneling barrier for coherent tunneling to take place. So far CoFeB is the best FM electrode material that has been found for achieving giant TMR due to its fully spin polarised Δ_1 states, its extremely smooth interfaces and its ability to be crystallised to a bcc (001) structure to form a four-fold symmetric CoFeB(001)/MgO(001)/CoFeB(001) coherent tunnel stack via solid phase epitaxy by magnetic field annealing.

In addition to the above, the film quality of the barrier layer is also important. Other crystalline tunnel barriers such as ZnSe (001)[37] or $SrTiO_3$ (001)[38] theoretically can also give giant TMR. However, due to the difficulties in fabricating high quality barriers without pinholes and interdiffusion at the interfaces for MTJs with ZnSe (001) or SrTiO3 (001) barriers [33], there will be still a way for these barriers to be applied in the real devices.

For device applications, the magnetization of one of the FM electrodes needs to be fixed by an AFM exchange bias layer. The strength of the exchange bias is another important parameter for MTJs as an increasingly large exchange bias field required for applications in advanced hard disk drives and MRAM continues to rise. The exchange bias phenomenon will be discussed in the following section.

2.2 Exchange bias phenomenon

MTJs consist of a pinned layer, a barrier and a free layer. A pinned layer is so called because it is exchange biased by an AFM layer. Exchange bias can occour in an AFM/FM or FM/AFM bilayer system. IrMn, PtMn or FeMn etc[39] is normally used as the AFM layer for exchange biasing in applications. In this section, the exchange bias phenomenon is first introduced followed by various models proposed to explain the phenomenon although the origin is still unclear.

2.2.1 The exchange bias phenomenon

Exchange bias refers to the shift of the center of a magnetic hysteresis loop from its normal position at $H = 0$ to $H_{ex} \neq 0$. It occurs in a system where an antiferromagnet is in atomic contact with a ferromagnet if the sample is grown or after the system is cooled through the Néel temperature of the AFM material in an external field. The phenomenon of exchange bias was first discovered in 1956 by Meiklejohn and Bean[40] when they observed a shift of the hysteresis loop in a sample of nominally Co nanoparticles after cooling in an applied field. It was subsequently established that the Co particles had been partially oxidized to CoO, which is thought to be AFM material.

The shifted loop (1) in Fig. 2.12 was measured at 77K for a compact of fine partially oxidized Co particles (10-100 nm) after cooling in a field of 10 kOe; the symmetric loop (2) was measured after cooling in zero field. Meiklejohn and Bean[40] showed that the loop shift was equivalent to the unidirectional anisotropy existing in the AF/FM system. An intuitive picture will be introduced in Section 2.2.

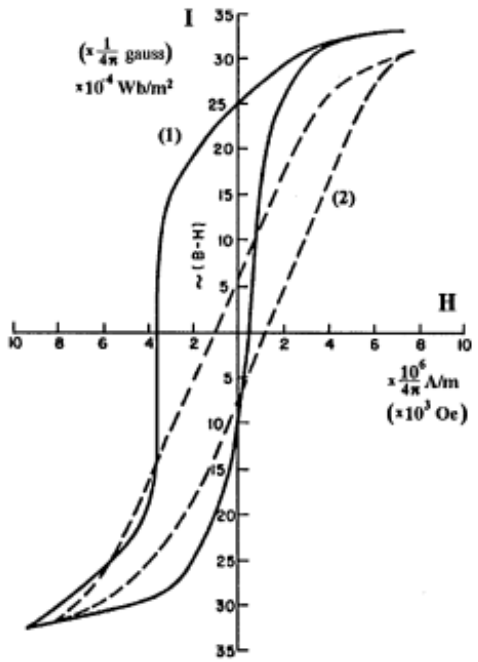

Fig. 2.12. Hysteresis loops of partially oxidized Co particles, from which the exchange bias phenomenon was discovered[40].

There are a large variety of systems where exchange bias has been observed, including clusters or small particles [41; 42], thin films deposited on single crystal or polycrystalline AFM [43; 44], and FM/AFM thin film bilayers [45; 46; 47]. This work focuses mainly on an AFM/FM layered structure.

The basic parameters to characterize exchange biased systems are the following:

(1) The pinning field or exchange bias field H_{ex}, which is a measure of the exchange coupling strength of the AFM/FM interface. It is measured by the unidirectional shift from the origin of the hysteresis loop of the exchange biased system, as shown in Fig. 2.12. H_{ex} is FM layer thickness dependent, and it decreases with increasing FM layer thickness.

(2) Interfacial coupling energy J_k (erg/cm^2), which is an alternative way of describing the interface exchange coupling strength, given by

$$J_k = H_{ex} M_s t_{FM} \quad (14)$$

Where M_s and t_{FM} are the saturation magnetization and thickness of the FM layer, respectively.

(3) Blocking temperature T_B, at which H_{ex} becomes zero. H_{ex} usually decreases with increasing temperature and mainly depends on the crystal phase structure of the material.

(4) Critical AFM layer thickness. There is always a minimum AFM layer thickness requirement for obtaining H_{ex}, below which H_{ex} will start to fall off.

All these parameters are of great application significance to realize high-density data storage devices such as reader heads and MRAMs. Especially, large H_{ex} or J_k is required in miniaturization of elements in hard disc drives and MRAMs to get high sensitivity for storage.

2.2.2 Understanding of exchange bias

Since the discovery of the phenomenon of exchange bias, the pursuit of the mechanism behind this phenomenon has never stopped. Early work by Meiklejohn and Bean[40] suggested that unidirectional exchange anisotropy was due to the presence of interfacial uncompensated AFM spins. The idea of interfacial uncompensated spin has attracted much attention especially in very recent years due to the availability of element specific x-ray magnetic circular dichronism (XMCD) [48; 49; 50; 51; 52], neutron diffraction and other depth sensitive techniques[53; 54; 55; 56; 57; 58] to study the buried layers or interfaces. Other models, such as the interfacial AFM domain wall and random field model [59; 60; 61; 62; 63; 64; 65; 66] were also proposed. These models will be reviewed in this section, especially the uncompensated spins model. Although much progress has been made, the origin of the phenomenon is still open to discussion.

2.2.2.1 Meiklejohn's fully uncompensated intuitive picture

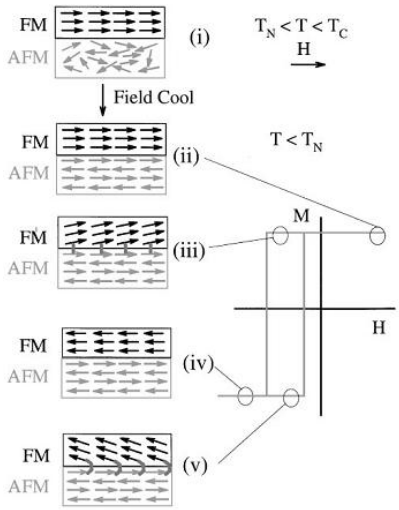

Fig. 2.13. Schematic diagram of the spin configuration of an FM/AFM bilayer (i) at different stages of an exchange biased hysteresis loop (ii) – (v)[67].

An exchange bias system consists of two basic layers in the form of FM/AFM (top pinned) or AFM/FM (bottom pinned). The AFM material, magnetically ordered below its Néel temperature T_N, with the spins parallel to each other on one plane, and anti-parallel in alternate planes, exhibits zero net magnetic moment. The FM layer is ordered up to its Curie temperature T_C, which is higher than T_N. When a field is applied to an AFM/FM system in the temperature $T_N < T < T_C$, the FM magnetization will align in the field direction while the AFM spins stay random (Fig. 2.13(i)). When the system is cooled to $T < T_N$, the AFM spins at the interface will couple to the aligned FM spins ferromagnetically due to the field. In this case, the interfacial AFMs are fully uncompensated. The other spins in the AFM are in antiferromagnetically ordered and produce zero net magnetization (Fig. 2.13(ii)). When the field is reversed, the FM spins begin to rotate. The AFM spins remain unchanged due to the large AFM anisotropy (Fig. 2. 13(iii)). The AFM spins at the interface exert a torque on the FM spins to keep them aligned in the direction of the cooling field. When the reversed field is strong enough to overcome the torque or coupling between the AFM and FM layers, the FM layer

reverses completely (Fig. 2.13(iv)). When the field is rotated to its original direction, the FM spins easily switch to their original alignment due to the interaction with the AFM spins (Fig. 2.13(v)). The AF/FM system behaves as if there was an internal biasing field and the FM hysteresis loop is shifted in the field axis, which is called exchange bias[40; 42].

This simple phenomenological model gives an intuitive picture, but there is little quantitative understanding of this phenomenon.

2.2.2.2 Models and theories

(a) Meiklejohn's model

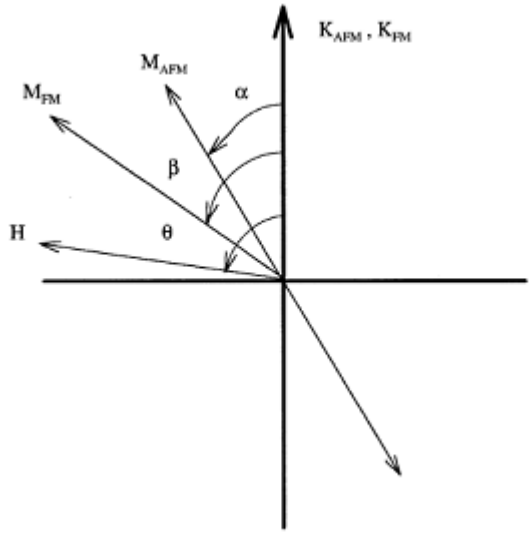

Fig. 2.14. Schematic diagram of vectors involved in an FM/AFM exchange biased system. It is assumed that the AFM and FM anisotropy axes are collinear[67].

Meiklejohn and Bean[40; 42] made the first attempt to propose an intuitive model to explain the origin of exchange bias. It was assumed that there is a coherent rotation of the magnetizations of FM and AFM layers, and the energy per unit area of an exchange bias system, can be written as

$$E = -HM_{FM}t_{FM}\cos(\theta - \beta) + K_{FM}t_{FM}sin^2(\beta) + K_{AFM}t_{AFM}sin^2(\alpha) - J_k\cos(\beta - \alpha) \quad (15)$$

Where H is the applied field; M_{FM} the saturation magnetization of the FM layer; t_{FM} (t_{AFM}), the thickness of the FM (AFM) layer; K_{FM} (K_{AFM}), the anisotropy of the FM (AFM) layer and J_k, the interfacial exchange coupling constant. α, β and θ are the angles between the AFM sub-lattice magnetization and the AFM anisotropy axis, the FM magnetization and the FM anisotropy axis, and the applied field and the FM anisotropy axis, respectively (Fig 2.14). The first term accounts for the effect of the applied field on the FM layer; the second term is the effect of the FM anisotropy; the third term takes into account the AFM anisotropy and the last is a consideration of the interfacial coupling. It is generally thought that the FM uniaxial anisotropy K_{FM} is negligible comparing to K_{AFM} ($K_{FM}t_{FM} \ll K_{AFM}t_{AFM}$), and minimize the energy with respect to α and β, the shift or the exchange bias that Meiklejohn found was[42]

$$H_{ex} = \frac{J_k}{M_{FM}t_{FM}} \quad (16)$$

The condition $K_{AFM}t_{AFM} \geq J_k$ is required in the minimization for the observation of exchange bias[42]. In this condition, the system energy is minimized by keeping α independent of β . But if $J_k \geq K_{AFM}t_{AFM}$, it is more favourable to keep $(\beta - \alpha)$ small and the AFM spins rotate together with FM spins, thus no loop shift would be observed.

According to this ideal and fully uncompensated model, the observed H_{ex}, however, is typically less by several orders of magnitude of the experimental result [68]. This simple ideal model does not represent the AFM/FM interfacial environment. The magnitude of the exchange bias depends on the value J_k. This discrepancy has invoked considerable research interest to account for the reduction of J_k by considering parameters such as interfacial contamination or roughness[69]. The hysteresis loops of

exchange bias systems have also been modelled by using different approximations of the energy equation, including the formation of domains in the AFM or FM layer [69; 70], random anisotropy in the AFM layer [71], grain size distribution and induced thermo-remanent magnetization in the AFM layer [72].

(b) Interfacial AFM domain wall

Mauri *et al* [71] put forward a model that would effectively lower the interfacial energy cost of reversing the FM layer without removing the condition of strong interfacial AFM/FM coupling. In this model, a planar domain wall is formed at the interface either in the AFM or FM layer or both of them wherever the energy is lower when the applied field is reversed. The formation of the domain wall will cost energy which will result in a reduction of the total energy in the AFM/FM system. For a domain wall formed on the AFM side of the interface, with the magnetization reversal of the FM layer the increase in interfacial exchange energy would be equal to the energy per unit area of an AFM domain wall, $4\sqrt{A_{AFM}K_{AFM}}$, where A_{AFM} and K_{AFM} are the exchange stiffness ($\sim J_{AFM}/\alpha$ where J_{AFM} is the AFM exchange integral parameter, and α is the AFM lattice parameter) and AFM magnetocrystalline anisotropy, respectively. The exchange bias would be:

$$H_{ex} = \frac{2\sqrt{A_{AFM}K_{AFM}}}{M_{FM}t_{FM}} \tag{17}$$

(c) Random field model

Rejecting the assumption of an atomically perfect uncompensated boundary exchange, Malozemoff [69] proposed a random field model of exchange anisotropy suggesting that the AFM/FM compensated and uncompensated interfaces originate from features such as roughness and structural defects. The random interface roughness creates a

random magnetic field that acts on the interfacial uncompensated spins, yielding unidirectional anisotropy, which causes H_{ex}.

(d) Uncompensated spins model

In Meiklejohn's model, it was suggested that exchange bias was a consequence of the presence of interfacial uncompensated AFM spins. In 1997, Takano et al. [72] demonstrated the experimental correlation between the interfacial uncompensated CoO spins and the exchange bias field in polycrystalline CoO/permalloy bilayer films. They measured thermo-remanent magnetization (TRM) of the uncompensated spins on the surfaces of antiferromagnetic CoO after field cooling a series of CoO/MgO multilayers from a temperature above T_N. This uncompensated moment is interfacial and is about 1% of the spins in a monolayer of CoO from neutron data[73]. The temperature dependence of the TRM is similar to the temperature dependence of the exchange bias of NiFe/CoO bilayers after field cooling. This suggests that uncompensated interfacial AFM spins appears to be responsible for the unidirectional anisotropy. Also, the observation that ~1% of the interfacial AFM spins are uncompensated is consistent with measured NiFe/Co exchange bias field of ~1% of the interfacial ideal uncompensated model. A linear relationship was also determined between the strength of the exchange bias field and the CoO grain diameter, $H_{ex} \propto L^{-1}$, where L is the grain diameter. This suggests a structural origin for the density of uncompensated spins.

Later in 2003, Ohldag et al.[51] reported the correlation between the exchange bias and the pinned interfacial uncompensated AFM spins, characterised as a vertical off-set of the AFM Mn hysteresis loops obtained by element specific XMCD in several exchange biased systems. The pinned uncompensated interfacial spins constitute only a fraction of a monolayer and do not rotate in an external magnetic field because they are tightly locked to the antiferromagnetic lattice. They also found that the coupling between the FM and AFM layers is parallel or ferromagnetic. Not clear about the origin of the

pinned spins, they speculated that the pinned interfacial uncompensated spins might be located at the grain boundaries of the AFM films. There have been very recent reports to give more intuitive pictures of the pinned interfacial spins and their relations with H_{ex} based on element specific XMCD and depth profile measurements of $Mn_{52}Pd_{48}$/Fe and permalloy/CoO bilayers[53; 58], respectively. However, such an understanding is still far from conclusive. In $Mn_{52}Pd_{48}$/Fe, there is a complex magnetic interfacial configuration, consisting of a 2-monolayer thick induced ferromagnetic region, and pinned uncompensated Mn moments that reach for ~13 Å, both in the side of antiferromagnetic layer at the interface. There is a direct relationship between the magnitude of the exchange bias and the pinned uncompensated Mn moments. In the permalloy/CoO system, it was identified by soft x-ray resonant reflectivity that there was a 5Å thin layer containing uncompensated Co magnetization at the interface with the permalloy. The majority of this magnetization follows the external field, however, ~10% of the moments in this interfacial layer that are pinned antiparallel to the cooling field. This part of pinned Co spins are antiferromagnetically coupled to the FM layer. Tsunoda el at[48] reported in 2006 from their element specific XMCD measurement of the IrMn/CoFe bilayer system with significantly different H_{ex} values, that Ohldag's model is not applicable to the giant exchange anisotropy of a IrMn/CoFe bilayer with a chemically ordered IrMn layer. The observed XMCD signal of Mn suggests that there are induced uncompensated Mn spins at the interface. However, unlike Ohldag's experiment, no vertical offset of the Mn hysteresis was observed for either the disordered or the ordered IrMn/CoFe systems. This suggests that insignificant uncompensated Mn spin was pinned at the interface to introduce exchange bias on the CoFe layer.

3 Equipment and experimental methods

The equipment and experimental methods employed during this work are introduced in this Chapter. First in Section 3.1 substrate preparation methods are discussed. Deposition process and factors are then considered in Section 3.2, followed by field annealing in Section 3.3 and fabrication techniques in Section 3.4 including photoresist spin-coating, lithography, ion milling and lift off. Lots of film and devices have been produced over this work. Specific issues of film deposition and device fabrication are discussed in Section 3.2.3. Characterization of films and devices are discussed in Section 3.5, starting with the analysis of properties of thin films using VSM, atomic force microscope (AFM) and x-ray magnetic circular dichroism (XMCD). MR measurement technique four point probe method is introduced at the end.

3.1 Substrate preparation

The quality of substrate is critical to producing good quality thin film devices. The substrate should be a good insulator to avoid short-circuits during MR testing. It also should be extremely smooth. Silicon wafers with a thermally oxidized SiO_2 layer are used in this work. Throughout this thesis, thermally oxidized silicon refers to Si substrates with a 100 nm-thick SiO_2 layer. The cleanness of substrates is extremely important for proper film adhesion. Substrates were cleaned prior to film deposition using an ultrasonic bath and appropriate solvents. The following procedure was followed before substrates were taken into the deposition chamber: submerge the substrates into a beaker of de-ionized (DI) water with several drops of “Decon Neutracon” solution (Decon Neutracon is a specialized surface active cleaning agent/decontaminant, near neutral concentration PH=7.) and agitate for 5 minutes in the ultrasonic bath to remove inorganic contaminants; rinse thoroughly with DI water and blow dry with a N_2 gun; submerge substrates again into a breaker of acetone, agitate for

5 minutes to remove organic impurities from the substrates, followed by agitation for 5 minutes in isopropyl alcohol (IPA) to get rid of the contaminated acetone from substrates; rinse substrates with DI water and blow dry with a N_2 gun; finally, bake the substrates in an oven at 100 ºC for 10 minutes to remove the residual moisture. An additional step in substrate surface cleaning was carried out by pre-sputter cleaning inside the chamber just before the film deposition.

3.2 Deposition of thin films

Magnetron sputtering in a high vacuum system was used to produce the films. This is one of the common techniques for thin film deposition. The sputtering system and related factors for the deposition of the films are introduced in this section.

3.2.1 The deposition system

The Nordiko 9550 physical vapor deposition (PVD) machine used in this work is shown in Fig.3.1. The system consists of one main chamber and a load-lock chamber connected by a gate valve. The advantage of two chambers is that a high vacuum can be maintained in the main chamber during loading/unloading of wafers. The wafers are transported from/to the load-lock by a robot arm. The ultimate base pressure of the tool is 2×10^{-8} Torr. Three cryo-pumps are used to evacuate the chambers, two for the main chamber and one for the load-lock chamber. Sputtering takes place in the main chamber, where six 10 inch targets are installed. Except for the MgO target, all the other targets, namely CoFeB, Cu, IrMn, CoFe and Ta are DC magnetron sputtered. The insulating target MgO is RF sputtered. There are four sputtering positions for 4 inch wafers in the main chamber. The sputtering process could be carried out either by setting the parameters such as Ar pressure, sputtering power, etc. manually or automatically by editing computer controlled functions and sequences.

Sputtering is based on a physical process whereby atoms ejected from a solid target by energetic particles are deposited on the substrate to form films. The energetic particles are usually ions of a gaseous material (usually Ar) accelerated in an electric field. As shown in Fig.3.2, the target is placed on the cathode (negative potential) and the substrate on the anode (positive). Both targets and substrates are enclosed in a chamber, which is evacuated by a pump system. Argon gas at a certain pressure is introduced into the chamber as a sputtering gas by which plasma is induced upon applying the sputtering power.

For DC sputtering, the glow discharge is maintained under the application of a DC voltage between the electrodes. Electrons accelerated in the electric field collide with Ar gas, producing ions Ar^+ and electrons:

$$e^- + Ar \rightarrow 2e^- + Ar^+ \qquad (18)$$

The produced electrons and ions are accelerated in the electric field, with electrons to the anode (substrates) and Ar^+ ions to the cathode (targets). The electrons on the way to anode cause further ionization. In this way, a current flows. Some of the target atoms will be sputtered off when the ions strike the cathode and will land on the anode or substrate to form a thin film. At the same time, while some of the target materials are being sputtered off, secondary electrons are also ejected from the targets and it is these secondary electrons which are responsible for maintaining the electron supply and sustaining the glow discharge [74]. The electrons or ions that are accelerated towards the substrates or targets produce a large amount of heat. For this reason, the substrates and targets are normally water cooled.

The glow discharge (i.e. current flow) is maintained between the metallic electrodes if the target in the DC sputtering system is composed of a metal. However, if the target is

an insulating material in the DC sputtering system, the sputtering discharge cannot be maintained due to the immediate buildup of a surface charge of positive ions on the insulator. To avoid the buildup of charge, an alternating voltage RF power supply is applied between the target and the substrate, so that the target is alternately bombarded by ions and then by electrons. Sputtering occurs when a negative potential is produced on the target surface, which serves as a sputtering potential [75].

By the use of magnetron sputtering, in which a magnetic field $\vec{B}$ is superimposed on the cathode, the deposition rate can be significantly increased. Both the magnetic field $\vec{B}$ and the electric field $\vec{E}$ act on the moving electrons in the discharge, causing the drift of motion along the $\vec{E} \times \vec{B}$ direction [76]. The electrons in plasma are confined in the vicinity of the target surface to form a high density electron region. The confined high density of electrons increase the rate of collisions with Ar, producing large numbers of Ar^+, which are then accelerated by the electric field towards to the target. According to Spencer [77], the highest density of electrons is in the region where $\vec{B}$ is parallel to the cathode target surface; it is there that the maximum sputtering rate occurs.

The PVD process can also be used to deposit films of alloys using a reactive or quasi-reactive deposition process [78]; CuN, for example, has been sputtered in this work by introducing a partial pressure of N_2 into the plasma during the Cu deposition process.
Pre-sputtering or sputter cleaning prior to deposition is needed for both the substrate and the target to remove contaminations. A shutter is used between the substrate and target to protect the substrate or target from cross-contamination during pre-sputtering. Sputter cleaning of the substrate is of significant importance in improving the adhesion between the substrate and the thin films and subsequent film properties. Experimental issues related to adhesion will be discussed in Section 3.2.3.

Fig. 3.1. Picture of Nordiko 9550 PVD sputtering system.

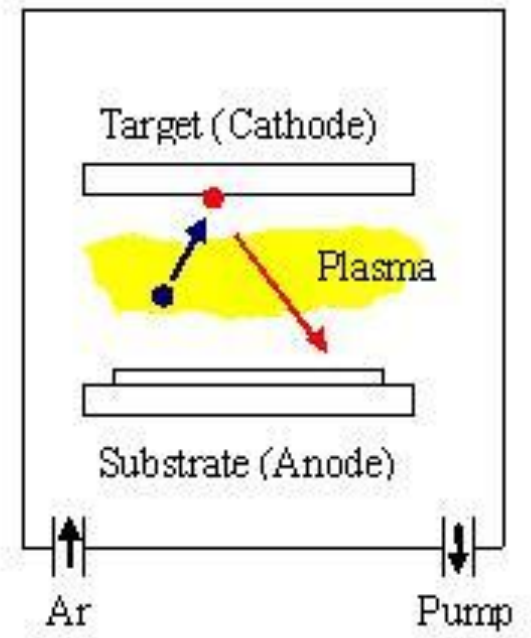

Fig. 3.2. Schematic illustration of the DC sputtering process

3.2.2 Deposition rate calibration

The deposition rate calibration of each film is established by measuring the thickness of the films after lift-off. The film thickness is measured by AFM, which is an effective tool to examine the film thickness as well as the surface morphology of thin films. The working principle and structure of AFM are described later in this Chapter. Fig. 3.3 shows a typical example of using AFM image and its line analysis software for film thickness measurement. The thickness difference could be calculated by selecting two positions as 1-2 and 1-1. The thickness of the film in Fig. 3.3 is 80.992nm as shown in the table. Alternatively, the cross-section of a film could be examined by high resolution transmission electron microscopy (HRTEM) to obtain the thickness of the film.

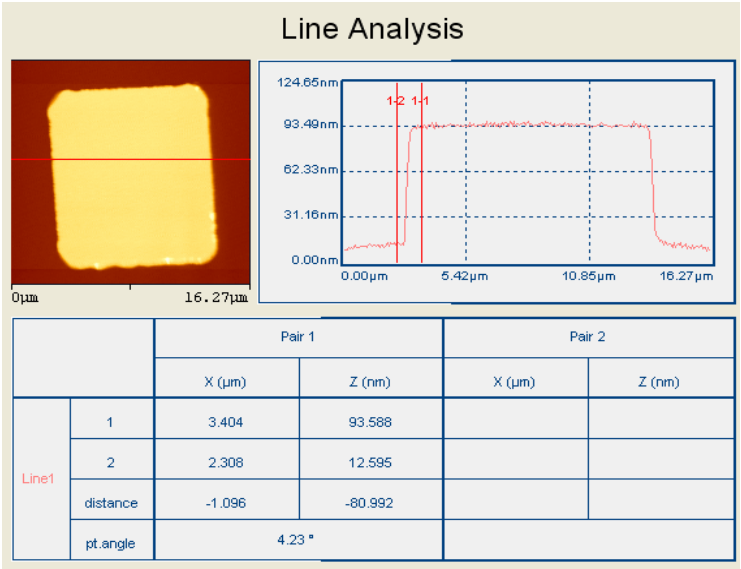

Fig. 3.3. Film thickness measurement using line analysis in the Nano-R AFM.

3.2.3 Optimization of deposition process

During the early stage of deposition of films by the Nordiko 9550 PVD sputtering machine, we observed circular blisters as shown in Fig. 3.4 on the multilayer films after magnetic field annealing at 350 ºC for one hour. These defects are not acceptable for device applications. Considerable effort has been devoted in trying to solve this problem.

It was believed that the formation of blisters was due to a combination of several factors: adhesion, stress and trapped Ar in the films, which are associated with the process parameters used during sputtering.

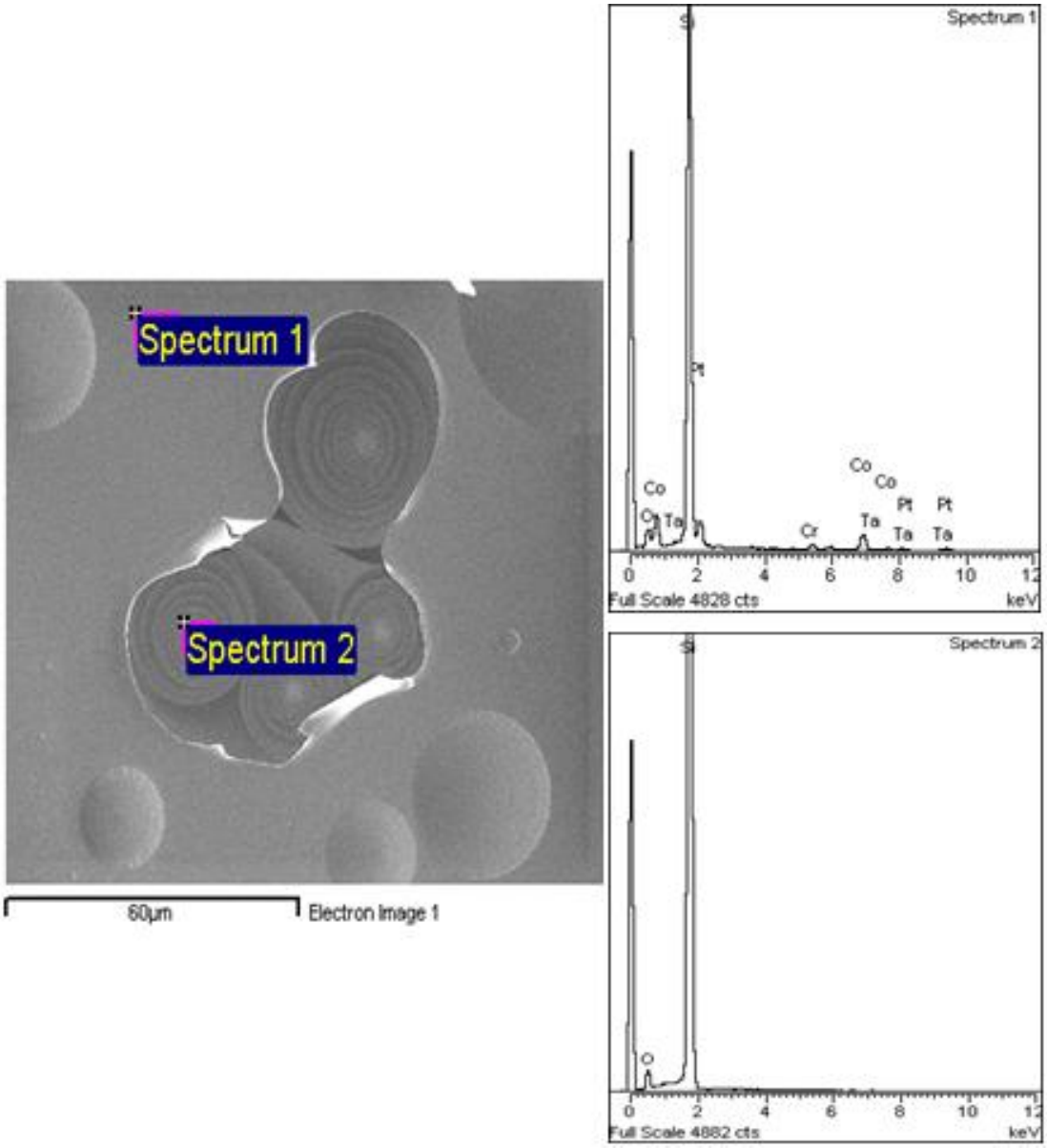

Fig. 3.4. SEM picture and energy dispersive x-ray spectroscopy (EDS) of an annealed sample with layer structure Si/SiO_2/Pt/CoCrTa/Ta. Spectrum 1 was taken on top of the film and spectrum 2, inside the broken blister.

A sample with blisters was first analyzed by a SEM equipped with energy dispersive x-ray spectroscopy (EDS), as shown in Fig 3.4. It can be seen from the EDS spectrum that the films in the blisters peeled off from the SiO_2 substrate surface, which suggests that it is associated with the film adhesion of the first layer.

In order to verify the possibility of trapped Ar in the films which may cause these blisters, samples with layer structure Ta (5 nm)/CoFe (3 nm)/IrMn (5 nm)/CoFeB (3 nm)/Ta (5 nm) were deposited and taken out of the machine immediately after deposition and put into the SEM for composition analysis by EDS. A typical spectrum is shown in Fig. 3.5. No Ar in the film was detectable or if there is any, it is non-detectable.

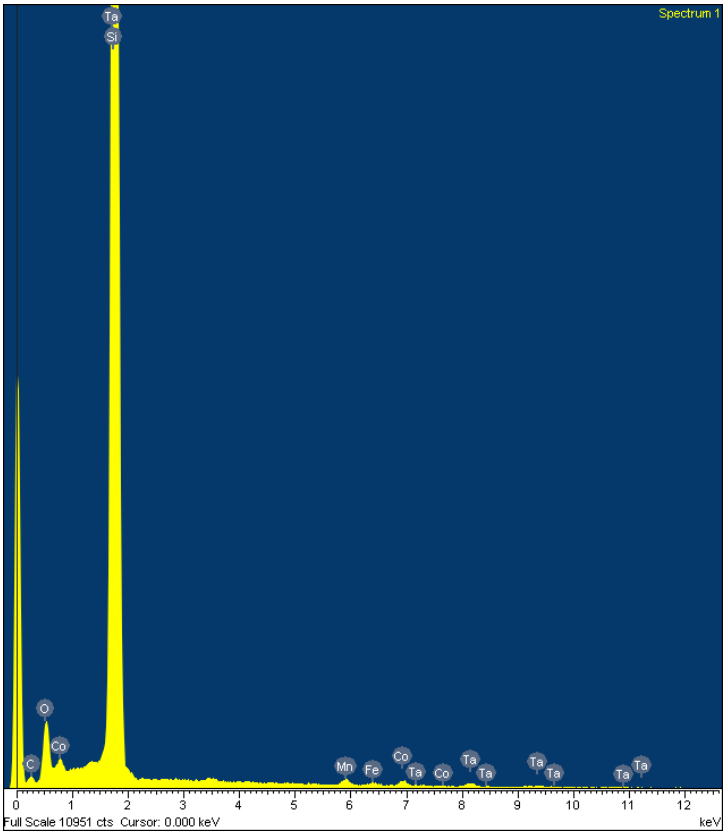

Fig. 3.5. EDS spectrum analysis for the sample with layer structure Ta (5 nm)/CoFe (3 nm)/IrMn (5 nm)/CoFeB (3 nm)/Ta (5 nm). The sample was taken out of the main chamber immediately for analysis and no Ar was detected.

A large number of samples have been studied with different pre-sputter cleaning and deposition conditions, such as power, time, Ar pressure and the time for the sample to be kept in the high vacuum main chamber after deposition in an attempt to resolve this issue. It was eventually concluded that the pre-sputter cleaning conditions (power and time) of the substrates are the key factors for eliminating these blisters in the films. The

results of a few typical samples are shown in Fig. 3.6 and Table 3.1 for samples with the layer structure Ta (5 nm)/CoFe (3 nm)/IrMn (5 nm)/CoFeB (3 nm)/Ta (5 nm) annealed at 350 ℃ for 1 hour. The surfaces of the films were examined using an optical microscope after annealing and the pictures are shown in Fig. 3.6. Samples (a) and (b), which were prepared with pre-sputter cleaning power of 60 W for 3 & 6 minutes, show considerable blisters but there is some reduction when the pre-sputter time increased from 3 to 6 minutes. An increase of pre-sputter cleaning power from 60 W to 80 W showed a further reduction of blisters as shown in Fig. 3.6 (c). A minimum of 100 W pre-sputter power for 3 minutes is required for obtaining blister-free films, as shown in Fig. 3.6 (d).

Sample	Pre-sputter cleaning power (W)	Pre-sputter cleaning time (minutes)
(a)	60	3
(b)	60	6
(c)	80	3
(d)	100	3

Table 3.1. Pre-sputter cleaning conditions of the samples (a)-(d) in Fig. 3.6.

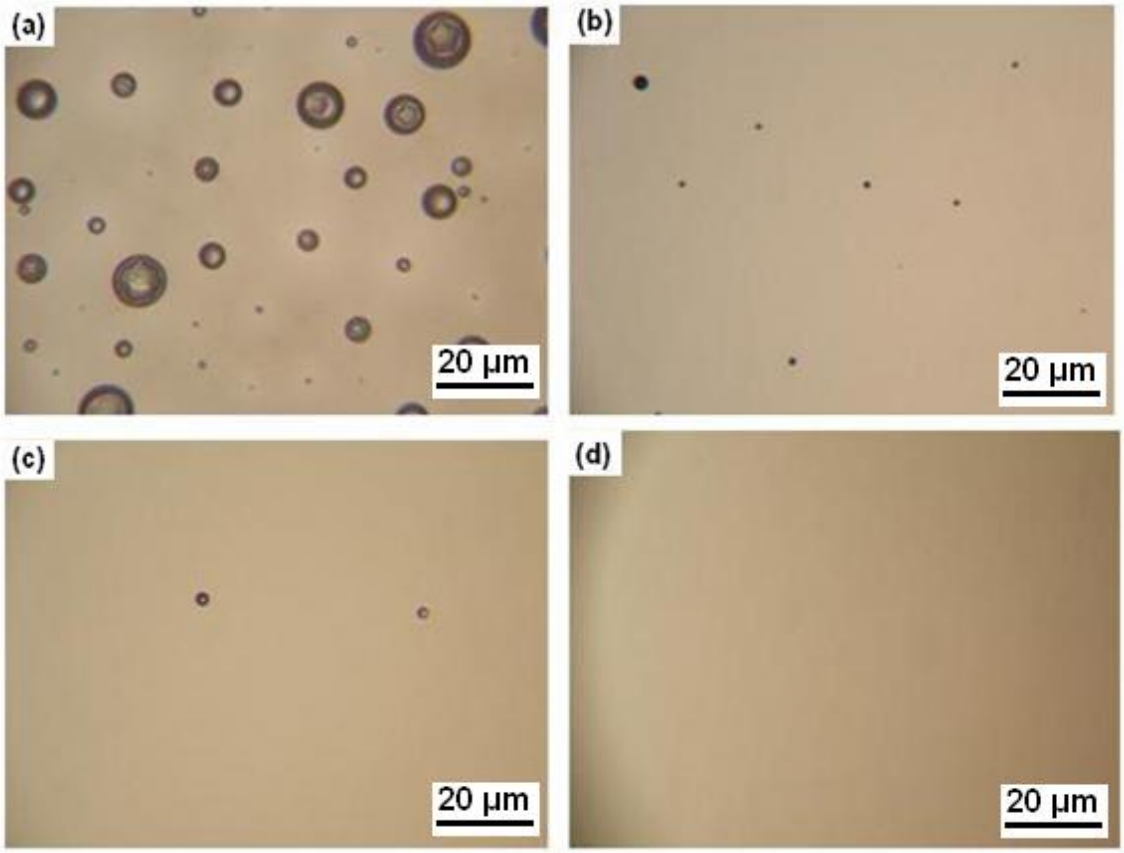

Fig. 3.6. Pictures of samples (a)-(d) taken at the same magnification by optical microscope after magnetic field annealing.

3.3 Magnetic field annealing

After film deposition, magnetic field annealing of a MTJ stack or AFM/FM bilayer system is required to establish the exchange bias field and improve other properties such as the crystallographic structure and orientation. For example, (001) orientated crystallization of CoFeB is required to obtain higher TMR for CoFeB MTJs. CoFeB is amorphous as deposited, and crystallization takes place when the annealing temperature (T_A) is beyond 250 ℃ [79; 80]. The TMR ratio depends on the annealing temperature [26; 29; 81; 82; 83]. Magnetic field annealing equipment in our lab is combined with a VSM (Fig. 3.9). The samples for annealing are placed in the middle of the magnetic field in a stainless steel box (for up to 2 inch square sample size) flushed with Ar gas. There are two pipes installed in the box, one inlet and one outlet for Ar. The Ar flow

can be checked occasionally by connecting the outlet pipe into a test tube containing paraffin. Normally, this pipe is disconnected during annealing to avoid back-streaming contamination of paraffin to the samples. The samples are placed so that the easy axis of the FM layer is parallel to the field. A magnetic field of up to 7 kOe could be applied during annealing through the electromagnet with a pair of 7 inch poles. The process for annealing includes temperature ramping up, keeping the temperature at a pre-set temperature for certain duration and temperature ramping down. The maximum T_a for this apparatus could be set to be up to 500 ℃. To ensure the quick ramping up and down, the steel box is wrapped with thermal insulation material maintaining the temperature during annealing and a fan is used to dissipate the heat during temperature ramping down. It takes about 45 minutes to reach 350 ℃ from room temperature and 1 hour to ramp down to room temperature.

3.4 Device microfabrication process

The MTJ devices are fabricated using standard clean room techniques. Fig. 3.7 shows the general route for the fabrication of an MTJ device, which includes the deposition of the MTJ stack, magnetic field annealing, photoresist spin-coating, mask aligning, exposure and developing of photoresist and ion milling to define device structures and bottom electrodes, photoresist removal, further spin-coating, exposure, develop, and film deposition and lift-off of SiO_2 insulation layers, and finally spin-coating of photoresist, exposure, development, and deposition and lift-off of the top and bottom electrodes.

It is critically important to develop well calibrated, reliable and repeatable processes and equipment in order to produce good quality devices. So optimization of the exact details

of the fabrication process and maintenance of the equipment were a large part of this work.

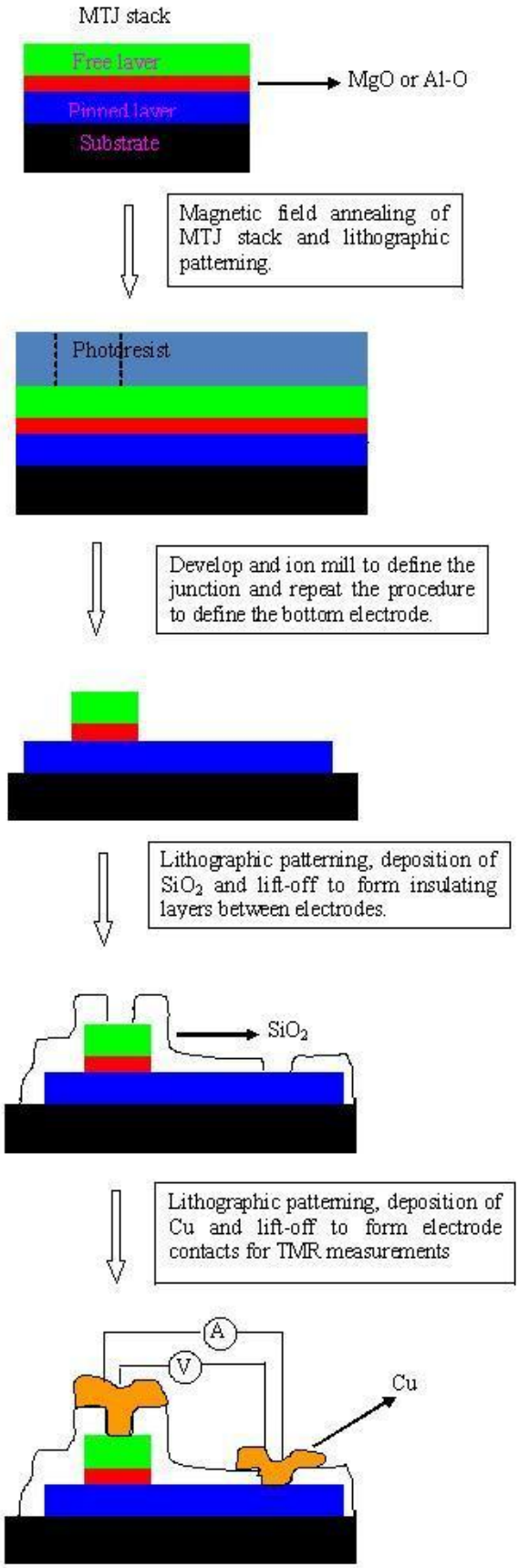

Fig. 3.7. Schematic diagram of the micro-fabrication process of MTJs.

3.4.1 Photolithography

Positive photoresist S1805 (Shipley's) has been used throughout this work. A positive photoresist is a type of photoresist in which the portion of the photoresist exposed to light (usually at wavelengths in the ultraviolet spectrum or shorter, <400 nm) becomes soluble in the photoresist developer, while the portion unexposed remains insoluble. S1805 was spun at 4 krpm for 1 minute to form a resist layer of ~0.5 μm thickness. Much care needs be taken to ensure the thickness uniformity of the photoresist film. The sample was then taken into an oven to pre-bake for 30mins at 95℃ before photolithography to drive away the solvent in the photoresist.

The photoresist patterning process was carried out on the OAI 500 mask aligner shown in Fig. 3.8, using chrome masks on a glass substrate, designed by L-editor and made by Compugraphics™. This contact mask aligner can produce a minimum feature size of 0.8 μm. It was used to define or align the patterns for the ion milling or lift off process. The alignment process involves several steps.

The model OAI 500 mask aligner incorporates an interchangeable mask/substrate chuck, a differential micrometer or motorized electronic motions for the x, y, and theta axis, an adjustable electronic clutch for setting the substrate to mask pressure and an exposure timer. It usually takes time to rotate the wafer to approximate alignment marks, align X-Y coordinates and finally align the wafer with the photomask using fine alignment marks. After the alignment, one must check the wafer is in the correct contact position and set the timer for exposure. The exposure time set for S1805 in our work is 4 seconds. One problem to which attention should be paid particular attention is that the photomask should be clean prior to its installation. Because the OAI 500 is a contact aligner, there may be traces of photoresist left on the photomask from the previous operation, which could result in un-wanted patterns on the substrates if these traces are not removed. After exposure, the sample is developed by immersion in the developer

(DI water: 351 developer equals to 4:1) for about 30 seconds. The sample is then rinsed thoroughly with DI water to remove traces of the developer and blow dry with a N_2 gun. Finally, it is very important to check the pattern under a microscope to ensure the quality. If the pattern is distorted, the photoresist must be removed with acetone and the process repeated.

Fig. 3.8. Picture of the OAI 500 mask aligner used for the work.

Fig. 3.9. Picture of the ion miller used for the work.

3.4.2 Ion milling

Ion milling is a physical technique to etch unwanted materials to obtain the desired device structures. In the microfabrication of MTJs in this work, ion milling was used with the first and second mask to define the junction mesa and bottom electrode pads. Together with the lithography, the milling process is schematically shown in Fig. 3.10, which includes phtoresist spin-coating (a), lithographic patterning (b), ion milling (c), and photo-resist removal (d): In Fig. 3.10 (a), a layer of S1805 was spun all over the wafer. Fig. 3.10(b) shows the pattern of the photoresist shape after development. Fig.3.10(c) shows the uncoverd part of the film was milled away by in milling and Fig.3.10(d) is the resultant film after the photoresist removal.

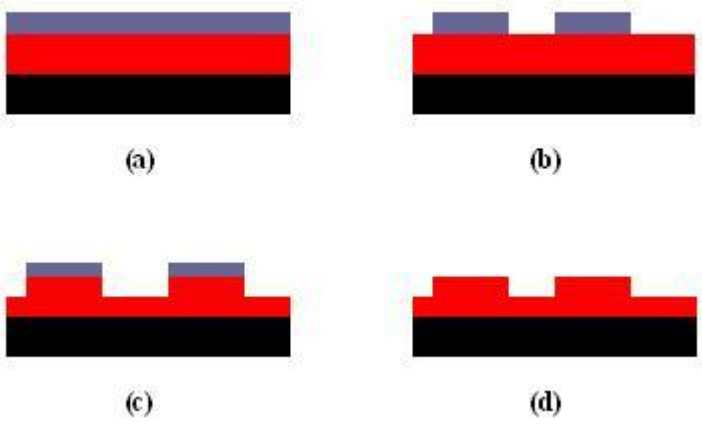

Fig. 3.10. Schematic illustrations of photoresist coating, lithography and ion milling: (a) sample after photoresist spinning, prebaking (b) after lithography, postbaking (c) after ion milling and (d) after photoresist removal.

The ion miller shown in Fig. 3.9 consists of a main chamber pumped by a diffusion pump and a power supply. The chamber is pumped down to low pressure to 2×10e-6 Torr and then filled with Ar. The ionized Ar is accelerated by a DC electric field towards the sample. The kinetically energized ions strike on the film and remove the unwanted portion not covered by photoresist as shown in Fig. 3.10 (b) and (c).

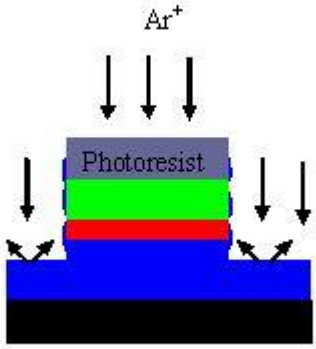

Fig. 3.11. Schematic illustration of re-deposition during ion milling.

There is a by-product of ion milling if the incidence of the ions is normal to the sample surface as shown in Fig. 3.11 in which the etched material is re-deposited onto the side

wall of the pattern. This is called re-deposition. Re-deposition can result in lower measured TMR or a short-circuit of the MTJ devices. To minimize the effect of re-deposition, the milling angle needs to be optimized or a second sidewall milling at the end of milling should be used. In our milling process, the milling stage was angled at 30 degree to the normally incident beam and rotated during the process. To avoid lower TMR resulting from re-deposition, the milling depth should be well controlled. The milling for the junction mesa for MTJ should be stopped right underneath the barrier as over-milling may cause a short-circuit. The milling depth was controlled by calibrated milling rate and double checked by AFM.

The striking of the sample by ions introduces a large amount of heating in the substrate. The photoresist may become toughened due to the heating in combination with the ion radiation resulting in difficulties in the removal of photo-resist after milling. To reduce the effect, the substrate is water cooled and the duration for each milling is controlled. We stopped for 5 minutes after each 2 minutes milling to cool the substrate.

The photoresist is hard to remove after ion milling. AFM was used to examine the conditions of photoresist removal for milled patterns. Fig.3.12 (a) shows a pattern with a fencing effect after the sample was milled and soaked in 1165 stripper, which represents the worst results at an early stage of the experiments. This was improved as shown in Fig.3.12 (b) by optimizing the milling parameters and photoresist removal conditions, such as milling time, milling angle, ultrasonic bath temperature and time, etc. But one can see from Fig.3.12 (b) that there is still some photoresist residue on the pattern. This was improved further by gentle cleaning with clean room tissue soaked in acetone as shown in Fig.3.12 (c).

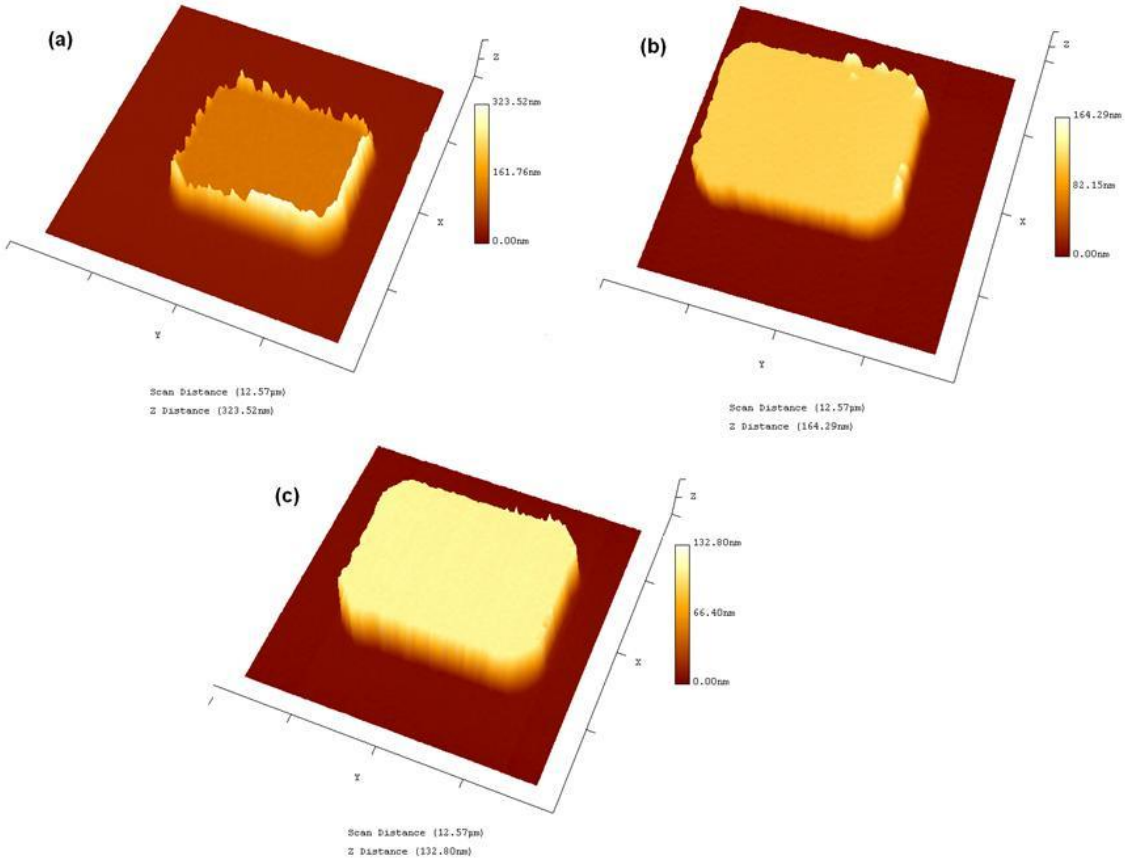

Fig. 3.12. AFM image of milled pattern (a) before parameters optimization; (b) after parameters optimization; and (c) after further cleaning by clean room tissue soaked in acetone.

3.4.3 Lift off

Apart from ion milling, lift-off is another technique in microfabrication of devices. Different from ion milling, lift-off is a process in which the film is deposited over a substrate partially covered with patterned photoresist. The removal the patterned resist after deposition leaves the desired portion of film on the substrate. Lift-off was also used for the calibration of the deposition rate of films. In the MTJ fabrication process, it is used for the deposition and patterning of the SiO_2 insulating layer between the top and bottom electrodes and the Cu contacting pads.

3.5 Characterization techniques

A number of characterization techniques have been used to test the thin films and devices. These techniques and their working principles are introduced as follows.

3.5.1 Vibrating sample magnetometer (VSM)

The magnetic properties of as deposited and annealed films were investigated using a VSM (constructed by Khew Joong Harnn) as shown in Fig. 3.13. A VSM consists of an electromagnet, a vibration unit with a sample holder, a pair of pick up coils, and a field sensor. It is based on the principle that a magnetic sample placed in a uniform field can be treated as a magnetic dipole and the magnetic flux from the sample which vibrates in the direction perpendicular to the applied field, can induce a voltage in the pick up coils nearby. As stated by Faraday's law of electromagnetic induction,

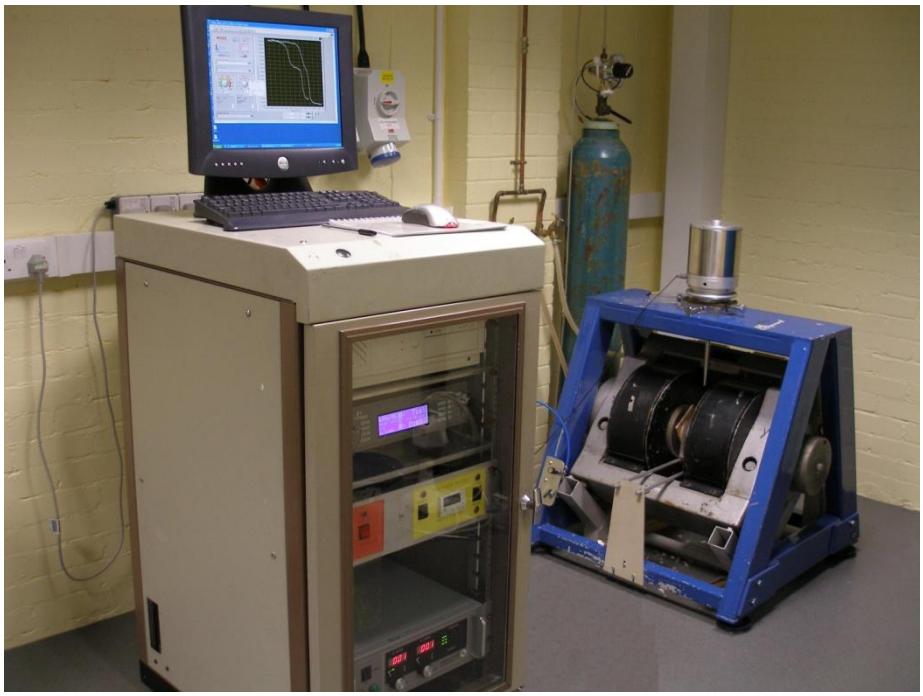

Fig. 3.13. Picture of the VSM in the lab built by Khew Joong Harnn.

$$V = N\frac{d\emptyset}{dt} = NA\frac{dB}{dt} \tag{19}$$

where, N is the number of turns of the coil, A is the cross sectional area of the coil and $\emptyset$ is the changing flux in the pick up coils. The voltage V in the pick up coils will vary depending on the magnetization of the sample, frequency of the motor, the amplitude of the sample movement and the coils design. The magnitude of the signal is proportional to the magnetic moment of the sample,

$$e = \frac{3}{4\pi}\mu_0 M \omega g_1 \tag{20}$$

where M is the magnetic moment of the sample; ω is the angular velocity of the vibration and g_1 is the instrument factor.

The typical VSM setup used in this work is schematically shown in Fig. 3.14. The magnetic sample is placed in a sample holder that is situated in the centre of a pair of pick up coils between the poles of an electromagnet. The sample holder is mounted to a rod, which is connected to a vibrating motor with an adjustable oscillation frequency. The vibrating motor is driven by a power amplifier which itself is driven by an oscillator. The magnetic sample is constrained to vibrate only along the vertical axis, inducing a signal in the sample pick up coils.

The output of the pick-up coil is fed to the lock-in amplifier, the output of which goes to the data acquisition computer. The magnitude of the magnetic field measured by the Hall Sensor is also fed to the lock-in and the PC. The field sensitivity of the VSM system has been improved recently, which can provide a precise magnetic measurement for very soft magnetic film.

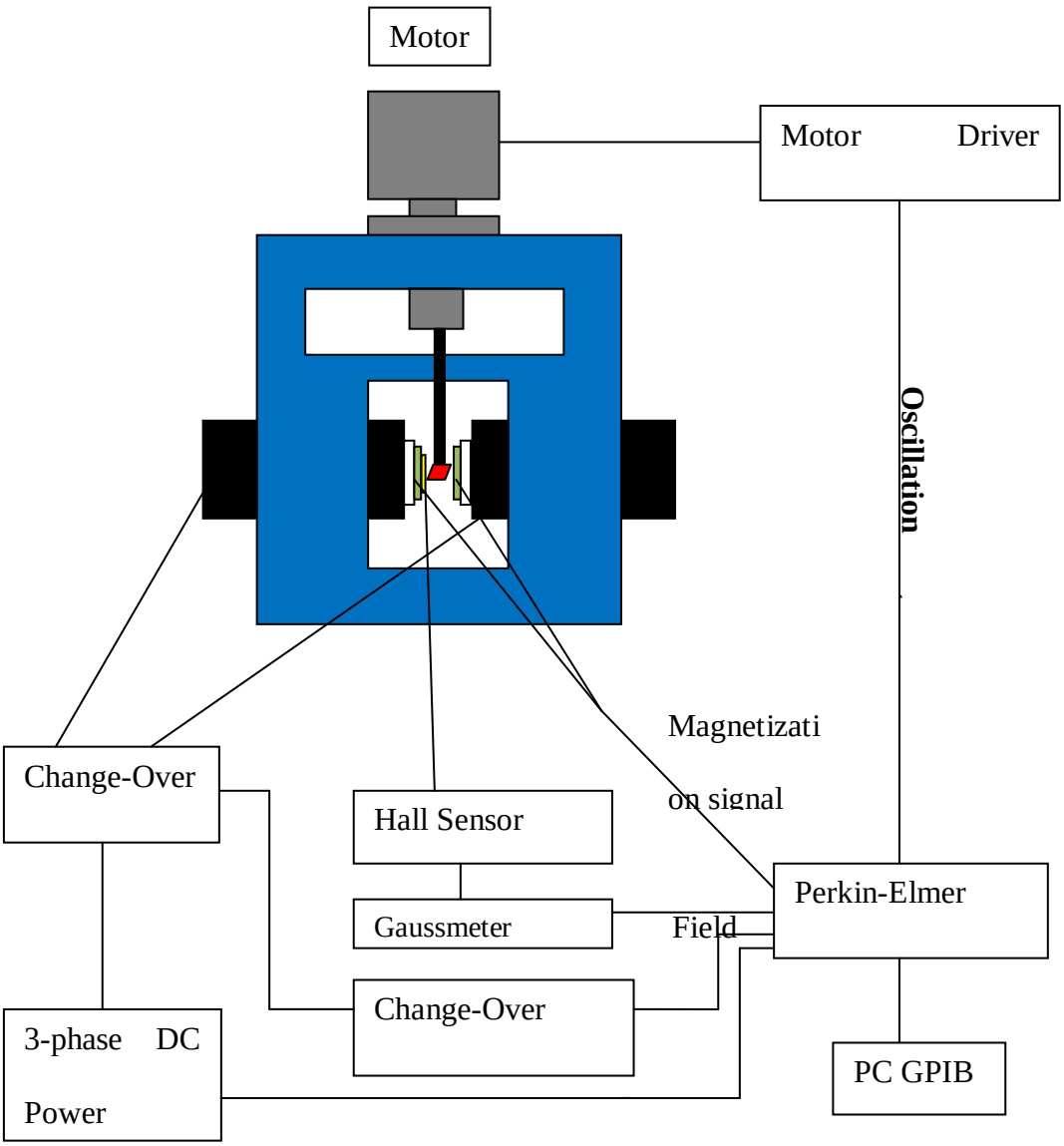

Fig. 3.14. Block diagram of VSM.

3.5.2 Atomic force microscope (AFM)

The AFM is a very powerful analysis tool as it creates a highly magnified, three dimensional image of a feature. It is an indispensable tool in the fabrication of MTJs. Using the AFM, the milling depth and calibration of deposition rate can be carried out quickly. The roughness of the films, which is also a main factor affecting TMR in MTJ devices, can also be examined by the AFM.

AFM, developed in mid-1980's, uses a sharp probe to magnify surface features. The theory and operation of an AFM is similar to that of a stylus profiler. Fig 3.15 illustrates an example of an early profiler, invented by Schmalz[84] in 1929, utilizing an optical lever arm to monitor the motion of a sharp probe mounted at the end of a cantilever. A magnified profile of the surface was generated by recording the motion of the stylus on photographic paper.

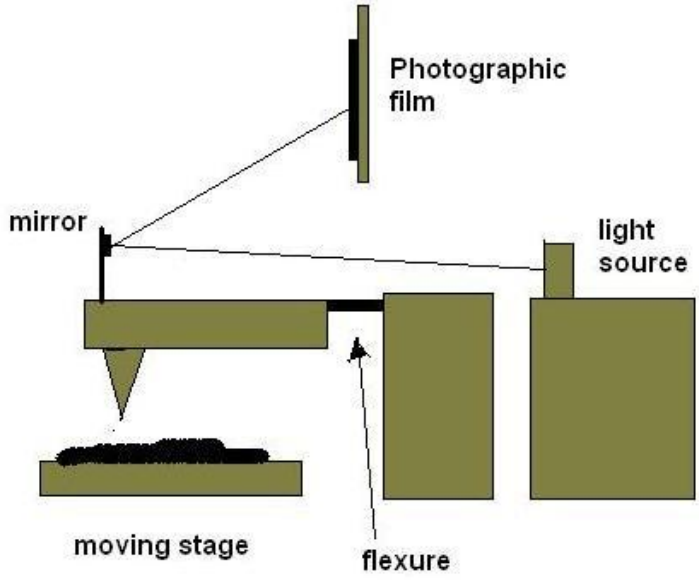

Fig. 3.15. Example of a surface profiler made in 1929.

In an AFM, the force between the probe and sample surface is maintained constant while the probe is raster-scanned across the surface. By measuring the force on the cantilever with the light lever sensor and by using a feedback control electronic circuit to control the position of the Z piezoelectric ceramic, the constant force is maintained. By monitoring the Z motion of the probe as it is scanned, a three dimensional image of the surface is constructed. The motion of the probe over the surface is generated by piezoelectric ceramics that move the probe across the surface in the X and Y directions as shown in Fig. 3.16.

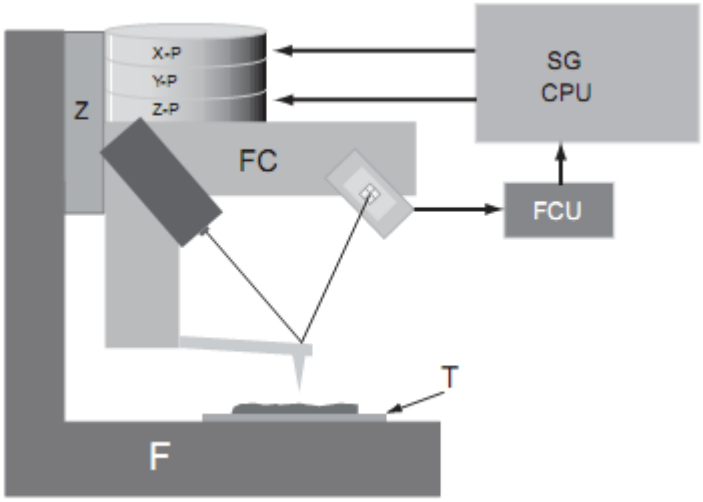

Fig. 3.16. Block diagram of an AFM [Nano-R^{TM}].

In the Nano-R^{TM} AFM (Fig. 3.17) used for this work, there are two modes of operation in measuring the force between the sample and probe, the contact mode and the close-contact (or non-contact) mode. In the contact mode, the deflection of the cantilever is measured directly. In close-contact mode, the cantilever is vibrated and changes in the vibration properties are measured.

In the contact mode, the sample is scanned with a fixed cantilever deflection using the feedback control. A constant force is applied during scanning the sample as the deflection is proportional to the force on the surface. The constant force applied between the probe and the surface is usually less than a nano-Newton and the probe is minimally touching the surface. In the close-contact mode, in which the tip does not "tap" the sample surface, the cantilever can be vibrated using a piezoelectric ceramic. The amplitude and phase of the vibrating cantilever may change when the vibrating cantilever comes close to the sample due to the change of atomic force. With either the vibration aptitude/phase kept constant by the feedback unit, changes in the vibration amplitude/phase are measured and correlated to the force on the surface.

Close-contact mode was used during our work to avoid damaging the devices or tripping the tip.

Fig. 3.17. Picture of Nano-R^{TM} AFM

3.5.3 X-ray magnetic circular dichroism (XMCD)

The understanding of interface effects in magnetic multilayers, for example the exchange bias phenomenon in AF/FM bi-layers, is of great significance. X-ray magnetic circular dichroism (XMCD) is one effective technique to study surfaces and interfaces using electron yield detection. XMCD is a difference spectrum of two x-ray absorption spectra (XAS) taken in a magnetic field, one taken with left circularly polarized light, and one with right circularly polarized light. By analyzing the difference in the XMCD spectrum, information can be obtained on the magnetic properties of the atom, such as its spin and orbital magnetic moment. One of the powerful features of XMCD measurement is that the magnetic moment detected is element specific.

The basic principles of XAS - When a sample is hit by x-rays, the electrons in the atoms will interact with the oscillating electric field of the electromagnetic radiation of

the x-rays. The radiation will be either scattered by these electrons or absorbed and excite the electrons. Fig. 3.18 shows such a process. When a mono-chromatic x-ray with intensity of I_0 passes through a sample with thickness x, some of the x-rays are scattered as "scattered x-rays"; and some are absorbed by the core electrons which are excited to partially filled orbits or out of the sample as "photoelectrons". When a core electron is excited it will leave a hole behind and this state of the system is not stable. There are two main ways this excited state can relax (fundamental of electrochemistry), either by emission of fluorescence x-rays (leading to fluorescence yield, FY) or by emission of an Auger electron (leading to electron yield, EY). Both of the fluorescence x-rays and the Auger electron signals can be processed to yield XAS spectrum as both signals are proportion to the x-ray absorption. The electrons on a higher energy level fall into the holes resulting in the release of energy. This energy can give off as fluorescent photons or may also excite other electrons, which will be ejected from the sample and are called Auger electrons. The intensity of the incident x-rays I_0 drops exponentially with distance x if the material is homogenous and the intensity of the transmitted x-rays I is:

$$I = I_o e^{-\gamma\mu x} \tag{21}$$

Where μ is the absorption coefficient and γ is the mass density.

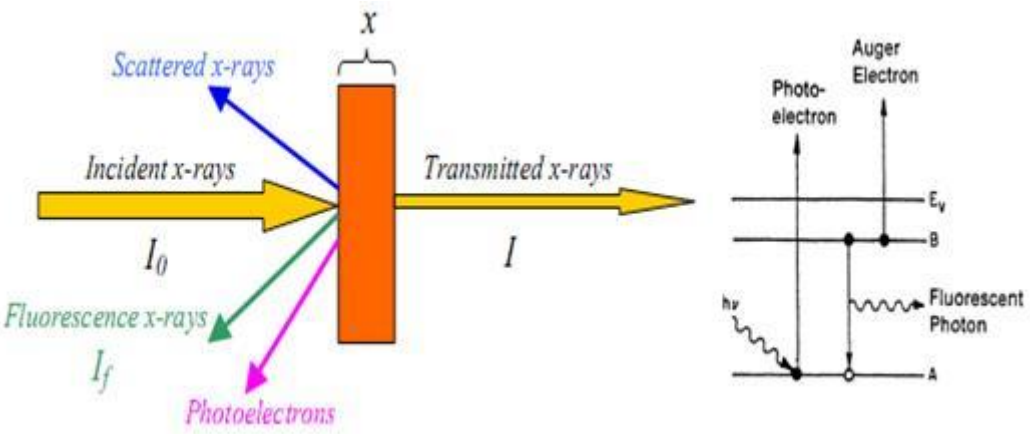

Fig. 3.18. X-ray absorption process[85]

XAS utilizes the energy dependent absorption of x-rays to obtain information about the elemental composition of the samples as well as the chemical environment of the atoms and their magnetic state. In the absorption process, core electrons are excited into empty states or into continuum above the Fermi energy at the absorption edges and the technique thereby probes the electronic and magnetic properties of the empty valence levels. The word "edge" represents the energy level from which the core electrons are excited: the principle quantum number $n = 1, 2,$ and 3 corresponds to K, L, M edges and so on (Fig. 3.19). The XAS spectra follow the dipole approximation selection rules, electrons can only make transitions that do not change their spin $\Delta s = 0$, and change their orbital number $\Delta l = \pm 1$, where $l = 0, 1, \ldots, n - 1$ is the orbital angular momentum corresponding to sub-orbits s, p, d, f … respectively. For the magnetic 3d transition metal elements Fe ($4s^2 3d^6$), Co ($4s^2 3d^7$) and Ni ($4s^2 3d^8$), the magnetic properties are largely determined by the 3d valence electrons, i.e. L-edge absorption (2p to 3d) is important. To excite one electron from a given core level, the photon or x-ray must have an equal or higher energy than the binding energy of this core level. Therefore the energy of the absorption edges are corresponding to the core level energy and it is element specific. Fig. 3.20 shows the L-edge x-ray absorption spectra of Fe which are dominated by the two main peaks of the L3 edge at lower energy and the L2 edge at higher energy.

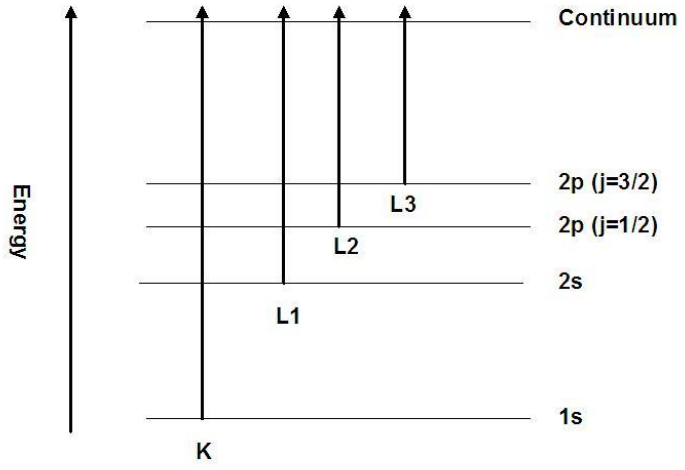

Fig. 3.19. XAS edges.

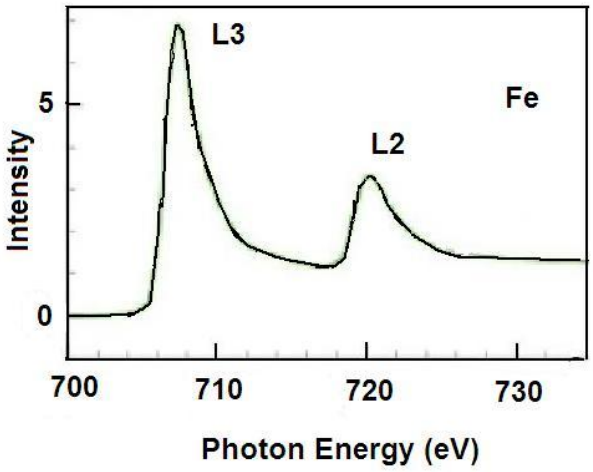

Fig. 3.20. L-edge x-ray absorption spectra of Fe[86].

The XAS spectra can be recorded by three ways: the transmission mode, the FY mode and the EY mode. The transmission mode is the simplest way which involves only measurement of the incident and the transmitted x-rays. The FY mode is to measure the incident and the fluorescent x-rays. In most cases, except for the fluorescent x-rays, the sample will also emit other x-rays, namely the scattered x-rays. To exclude the scattered x-rays, an energy-resolving solid-state fluorescence detector is used, such as a Lytle detector or a Ge detector. Another mode is EY mode. EY measurements can be performed by counting the energy of either all the total electrons (TEY), including

Auger, secondary and photoelectron, or of the partial electrons (PEY). TEY mode was used in the XMCD measurement in our work. The signal of TEY is depth dependent and decays exponentially with depth from surface[87]. A very thin cap layer in our XMCD samples to obtain enough signal.

The basic principles of XMCD - The magnetic properties of FM materials are usually studied by XMCD, which measures the difference in the XAS taken in a magnetic field using left and right circularly polarized (LCP and RCP) x-rays.

The circularly polarized x-rays are in a definite eigestate of the angular momentum operator in the direction of the propagation with LCP and RCP in an opposite direction. During the absorption process, the x-ray photon is annihilated and its momentum must be transferred to the sample, so apart from the dipole approximation selection rules, $\Delta s = 0$ and $\Delta l = \pm 1$, the excited electrons also obey $\Delta m_l = +1$ for RCP x-rays and $\Delta m_l = -1$ for LCP x-rays, where m_l is the magnetic quantum number with $m_l = 0, \pm 1, \pm 2 \ldots \pm l$. Polarized photoelectrons will be exited. Consider a 3d metal, core electrons will be excited into the 3d empty states with L2 ($2p_{1/2}$ to 3d) and L3 ($2p_{3/2}$ to 3d). 2P is split into $2p_{1/2}$ and $2p_{3/2}$ through the spin-orbit coupling ($l + s$ and $l - s$, respectively). For a certain RCP x-ray or LCP x-ray, due to the transition selection rules, spin polarized photoelectrons will be excited with opposite sign for $2p_{1/2}$ and $2p_{3/2}$ as they have opposite spin-orbit coupling. RCP x-ray has its orbital angular momentum in the direction of propagation and will preferentially excite the $2p_{3/2}$ states over the $2p_{1/2}$ states and it is the opposite case for LCP x-rays, whereby the $2p_{1/2}$ is preferred[88]. As there is difference between RCP and LCP XAS at L2 and L3 edges, a non-zero difference will show up. As the transition probability depends on the density of empty states in the d band, the d band spin down and the empty states act as a detector for the

photoelectron. If the number of empty states are the same for spin up and spin down, there will be no change of the absorption intensity between the RCP and LCP x-ray. Once there is an unbalance number between the spin up and spin down empty states, the absorption of the two polarization is different and the difference is opposite for L2 and L3 edges.

Fig. 3.21 shows the XMCD effect of Fe. The red and light blue line represents the absorption spectra using the right and left circularly polarized x-ray photons. The difference of the two lines gives the magnetic properties of Fe. By the application the sum rules[89] to the XMCD signal, the average of the spin and orbit magnetic moments can be estimated[48]. If there is no net spins in the material, there will be zero XMCD signal[52]. The most powerful feature of XMCD magnetometry is that the measurement is element specific.

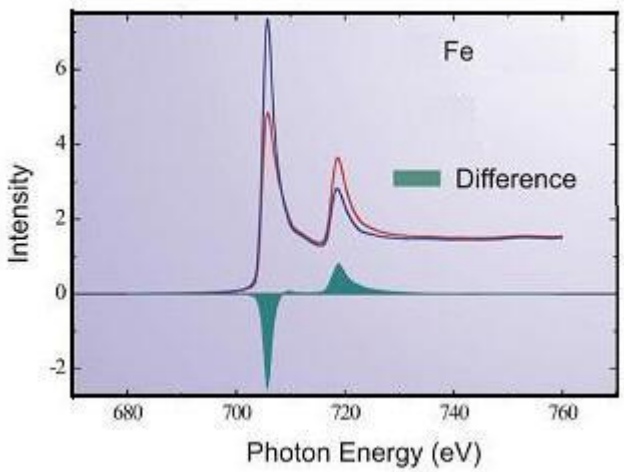

Fig. 3.21. XMCD effect of Fe[90].

3.5.4 Four point probe

The four point probe magnetic measurement is a widely used technique for measuring sheet film resistance or MR properties. Fig. 3.22 is a schematic set up of a four point probe method. A set of four linear microprobes is placed on a flat surface of a material

with separation distances of S_1, S_2 and S_3. A constant current is passed through the two outer electrodes, and the response voltage is measured across the inner pair.

For a regular bulk conductor, the resistance is $= \rho \frac{L}{A}$, where ρ is the resistivity, L is the length and $A = Wt$ is the cross sectional area. Thus$R = \rho \frac{L}{A} = \frac{\rho}{t}\frac{L}{W} = R_s \frac{L}{W}$, and $R_s = \frac{\rho}{t}$ is the sheet resistance.

For a material of semi-infinite volume, the resistivity is given by[91]:

$$\rho = \frac{V}{I}\frac{2\pi}{\frac{1}{S_1} + \frac{1}{S_3} - 1/(S_1 + S_2) - 1/(S_2 + S_3)} \tag{22}$$

When $S = S_1 = S_2 = S_3$, it reduces to

$$\rho = \frac{V}{I} 2\pi S \tag{23}$$

It can be shown[91] that when $t \ll S$,

$$\rho = \frac{V}{I}\frac{\pi}{ln2} \tag{24}$$

or the sheet resistance R_s is:

$$R_s = \frac{\rho}{t} = \frac{V}{I}\frac{\pi}{ln2} \tag{25}$$

From Equation (24), it can be seen that the value of the measured sheet resistance is independent of the probe distance.

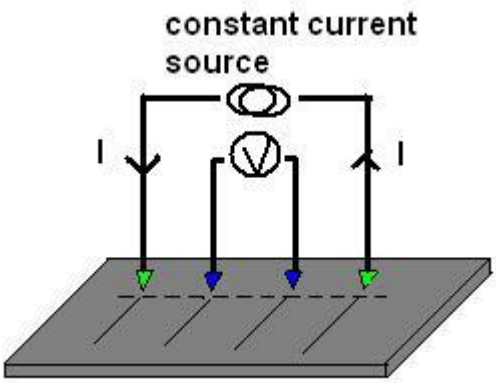

Fig. 3.22. Schematic set up of four point probe measurement.

Fig.3.23 shows the four point probe measurement system in our lab and its block diagram is shown in Fig. 3.24. Using a LabView programme developed by Mr. Kuan-yi Yang with a GPIB interface card controlled TTI PL 330TP Power Supply, Keithley 2182 nanovoltmeter and Keithley 6221 source meter, this system provides precise MR measurements for thin film devices. The device was placed in the middle of the magnetic field driven by TTI PL 330TP power supply. A constant current is applied between the two outer probes by the Keithley 6221 source meter. The voltage between the two inner probes is measured from the Keithley 2128 Nanovoltmeter. The magnetic field was measured by a Hall probe mounted in the middle of the magnetic fieled. Up to 1800 Oe of magnetic field could be applied in this system.

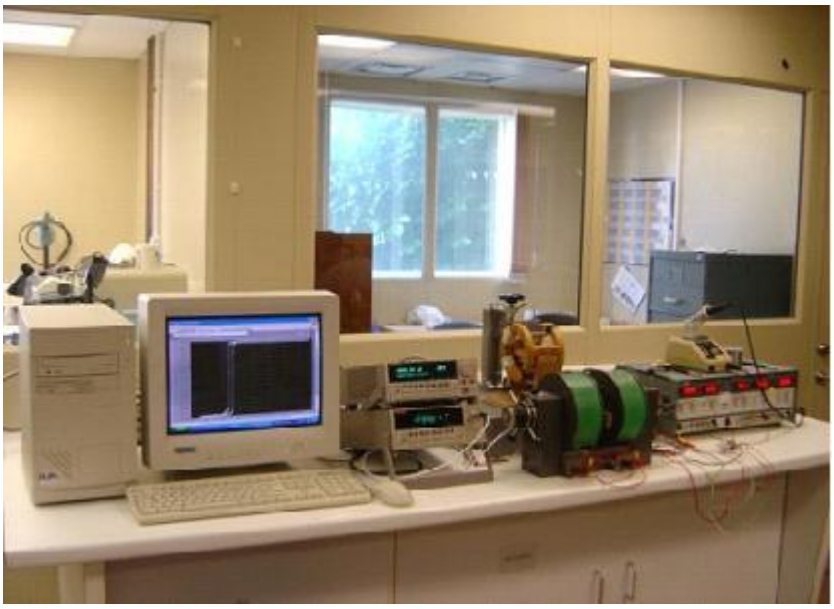

Fig. 3.23. Picture of the four point probe system in Plymouth.

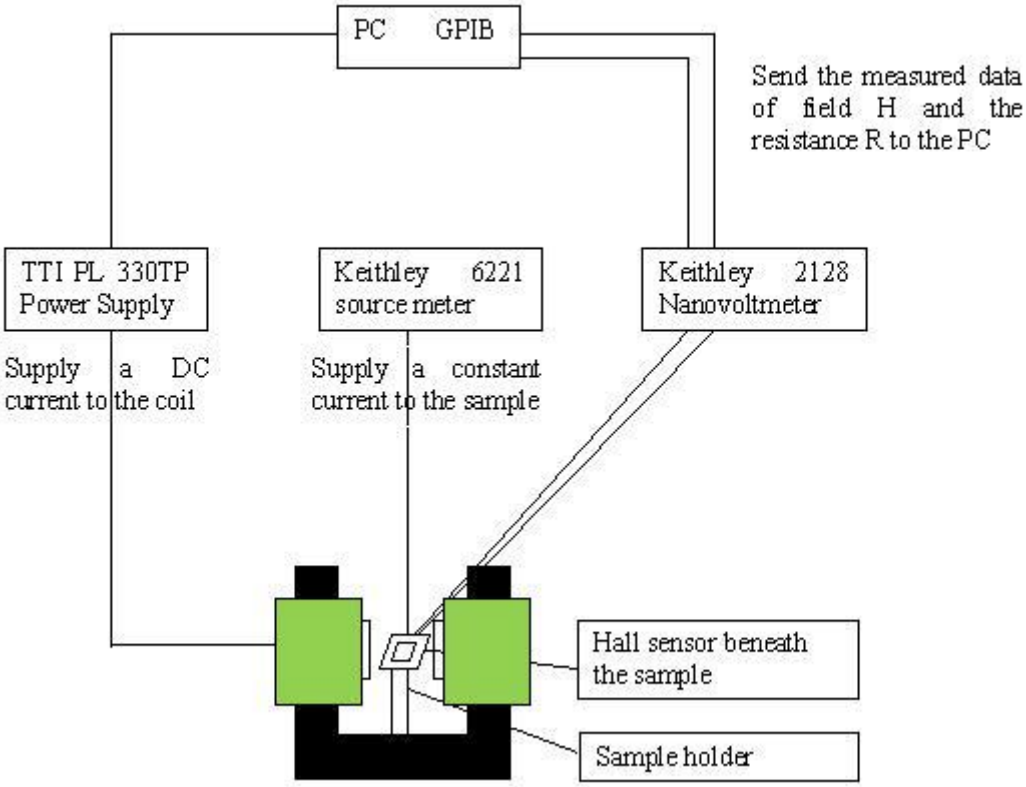

Fig. 3.24. Block diagram of a four point probe system.

4 The DTI MNT project

For most of the first two years of the PhD programme, the author participated as a Research Assistant in the DTI MNT funded project "300-mm ready ion beam deposition system for spintronics and MRAM", led by Aviza Technology Inc. The aim of this project was to build the 300 mm IBD tool for the manufacturing of the next generation MTJ based devices for applications in MRAM, hard disk drives, read heads, RF components and other spintronic devices. In November 2008 after the successful completion of the project, Aviza Technology announced the world's first 300-mm ready IBD system for MRAM and spintronics[92], the StratIon™ *fx*P, a picture of which is shown in Fig. 4.1. The first machine was shipped to CEA-LETI_MINTEC in Grenoble, France, one of Europe's foremost applied research centers in electronics and spintronics.

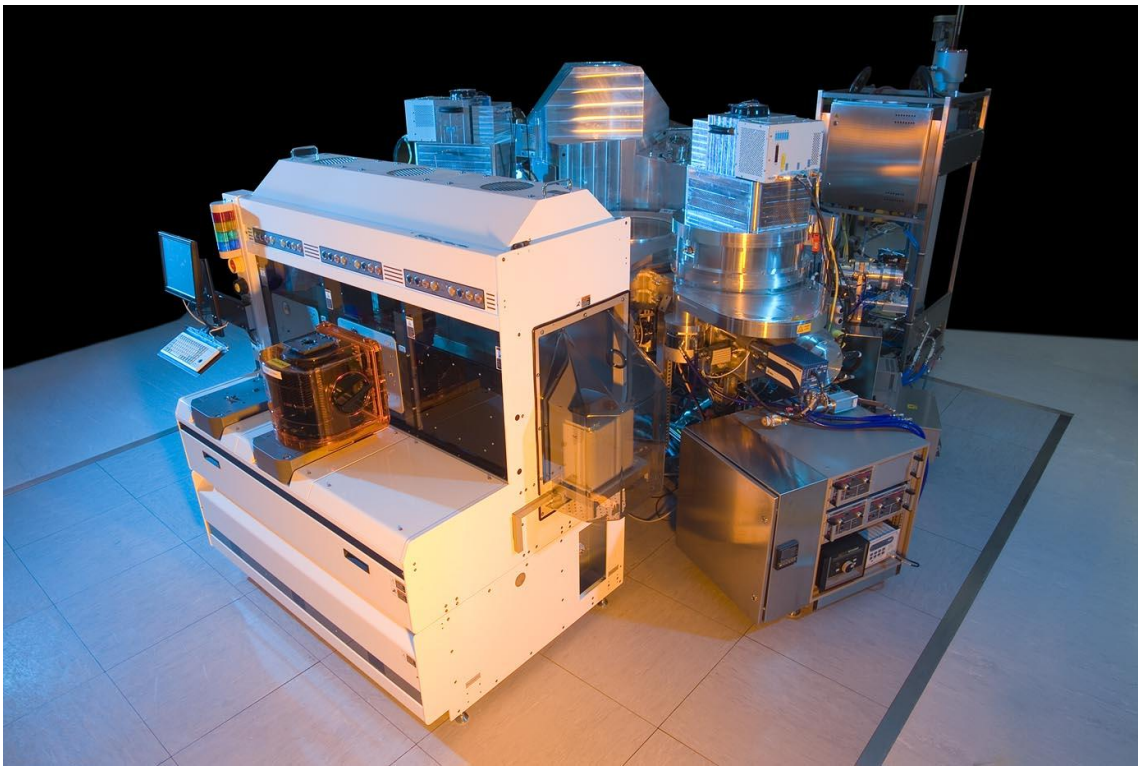

Fig. 4.1. The world's first 300-mm ready IBD system for MRAM and spintronics, StratIon™ *fx*P

The Plymouth group was a sole academic partner in this £3M project, responsible for the technical advice for some aspects of the design and operation of the tool, and the nanoscale characterisation of films, magnetic properties measurements, magnetic field annealing, microfabrication and MR measurements of MTJs. Results presented here are obtained by the author from the StratIon^{TM} *fx*P tool in partnership with the project consortium.

4.1 Exchange bias of PtMn/CoFe

PtMn is one of the AFM materials which could be used as pinning material in exchange bias systems for practical applications due to its high pinning field, high blocking temperature and good corrosion resistance [93; 94; 95]. However, as the as-deposited PtMn is paramagnetic, rather than antiferromagnetic, the as-deposited PtMn/FM exhibits no exchange bias [96]. The desired AFM fct phase can be obtained by magnetic field annealing [97]. One of the major advantages of IBD is its collimated incident ion beam and its ability to vary the target-substrate angle for optimized film properties.

Four samples with layer structure Ta (10 nm)/ PtMn (20 nm)/ CoFe (3 nm)/Ta (10 nm) deposited on 300 mm silicon were provided by Aviza. The PtMn film in each sample was deposited at an angle of the substrate relative to the target (ST angle) at 0°, 10º, 20º, and 30°, respectively. As the sample holder for annealing is limited to 2inch×2inch sample, in order to have a good comparison between these samples, the samples for annealing were cut to 1inch×1inch. Each annealing will contain four samples, either from the same 300 mm size sample with the same deposition angle or one each from the big sample with different deposition angle. A sweep of annealing temperature (T_A) of 275 ℃, 300 ℃, 325 ℃ and 350 ℃ for 2 hours with an external field of 5 kOe was carried out on each sample from different deposition angle. The samples were measured

by VSM for the MH loops. The exchange bias H_{ex} was calculated by the shift of the MH loop along the x axis.

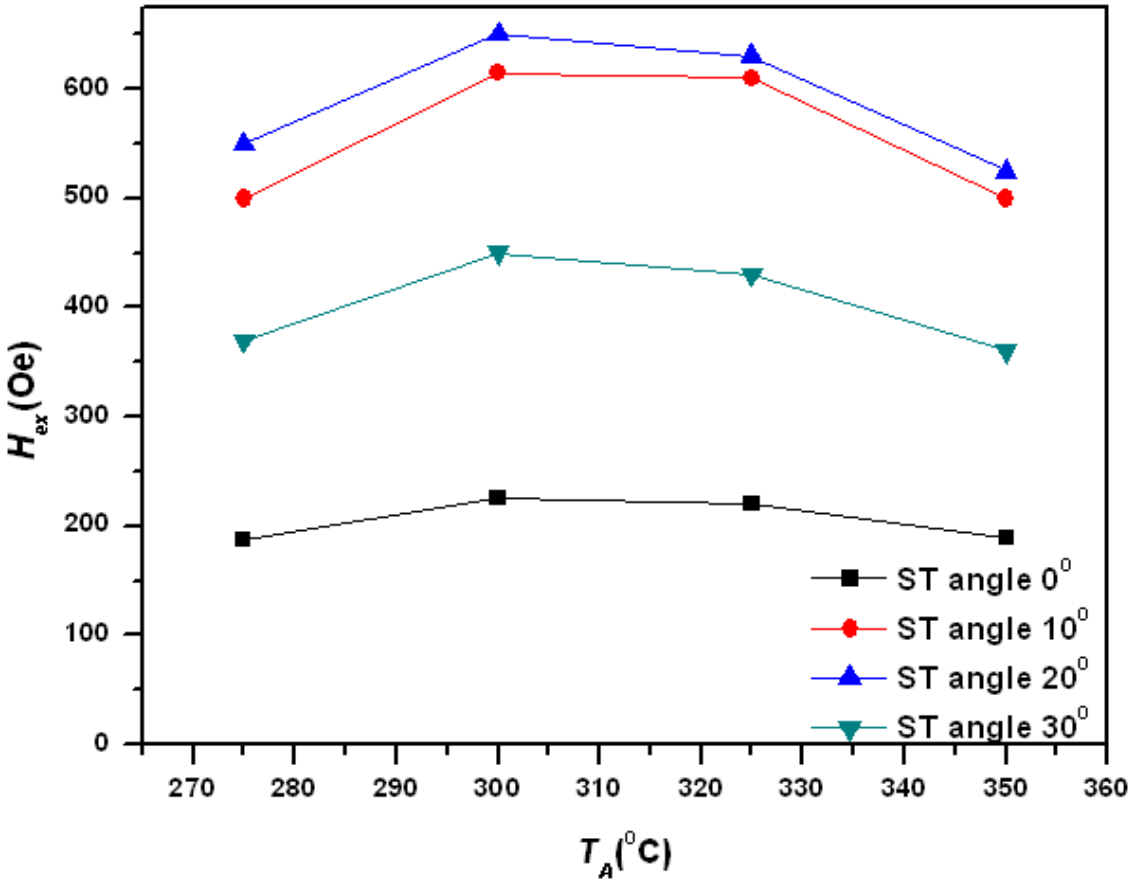

Fig. 4.2. Exchange bias measured by VSM on samples deposited on ST angle (0°, 10°, 20° and 30°) annealed at different annealing temperature (275℃, 300℃, 325℃ and 350℃).

Fig. 4.2 shows the exchange bias of samples deposited at different ST angle annealed at different temperatures. It is found out that sample deposited at ST angle 20° annealed at 300℃ gives the maximum H_{ex} about 650 Oe. For a specific annealing temperature, sample deposited at ST angle 20° (blue dot) showed the higher H_{ex} than other sample deposited at different ST angle. For the different annealing temperatures, each sample with different ST angle shows a similar trend with the highest H_{ex} around 300℃.

Fig. 4.3 shows MH loops measured by VSM with H_{ex} of 225 Oe, 615 Oe, 650 Oe and 450 Oe for the samples deposited at ST angle 0º, 10º, 20º and 30º, respectively. By changing the ST angle from 0º to 30º, H_{ex} increased from 215 Oe at 0º, reached maximum 650 Oe at 20º and then decreased to 450 Oe at 30º.

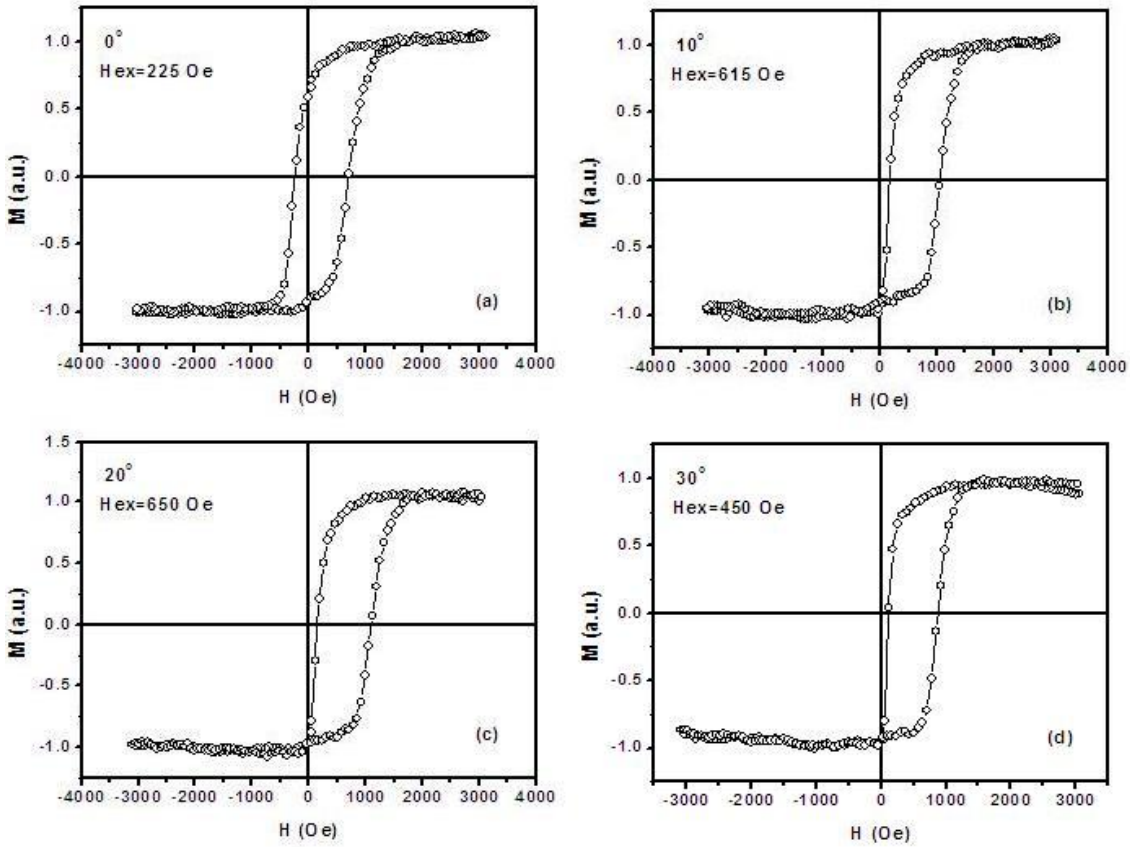

Fig. 4.3. MH loops of annealed Ta (10 nm)/ PtMn (20 nm)/ CoFe (3 nm)/Ta (10 nm) with PtMn IBD deposited at ST angle of 0º, 10º, 20º and 30º, corresponding to (a)-(d).

The dependence of H_{ex} on substrate-target angle can be attributed to the change of film composition due to the change of incident beam angle to the target. It was reported H_{ex} thatis dependent of the elemental ratio of the Mn and Pt and the highest H_{ex} is obtainable when the ratio is 1:1[98]. By the variation of the substrate-target angle in the IBD, the composition of the PtMn film can be controlled due to the difference in sputtering yield of the Pt and Mn atoms under different incident beam angles [99]. M. Rickart [99] *et al* reported similar trend of substrate-target angle dependence where at

31º they obtained an optimum H_{ex} of ~ 450 Oe for their Nordiko IBD deposited sample of Ta (30 nm) /PtMn (20 nm)/CoFe (5 nm)/Ta (10 nm) annealed for 2 hours at 330 ºC. Considering the FM thickness used in the exchange bias layer structure, the H_{ex} value obtained in our work 650 Oe for 3nm CoFe is comparable to 450 Oe for 2nm CoFe 5nm in the Nordiko IBD deposited sample. They found that the composition ratio of PtMn is approximately 1:1 at substrate-target angle of 31º. In our work, the optimum H_{ex} is obtained at a ST angle of around 20º. The optimal angle in each case could be different due to the initial composition of the PtMn target or due to different tool design.

The annealing temperature has an effect on the H_{ex} . The blue line in Fig. 4.2 for example, the H_{ex} increases with the increase of T_A before 300 ºC where it reaches a maximum value of 650 Oe and then decreases with the further increase of T_A. This relationship can be explained by the film structure change during the annealing. If the annealing temperature is too low, the PtMn structure transition from fcc to fct is not enough which will affect the exchange bias. If the annealing temperature is too high, there will be an inter-diffusion at the interfaces which results in the reduction of the exchange coupling at the interface[100].

We also studied the repeatability of the performance. More samples including sample deposited at TS angle 25°, together with 0°, 10°, 20° and 30° were requested. These samples were repeat twice at these annealing temperatures, 250℃, 275℃, 300℃, 325℃ , 350℃ and 375℃. Together the previous results shown in Fig.4.2, they are plotted in Fig.4.4. The trend is still valid the relationship of the exchange bias and annealing temperature and the TS angle. Sample deposited at TS angle 20°, annealed at 300 ℃ is still the optimum point. Overall the points are matched although there are about 10~20 Oe difference on the measurement value, it is reasonable. One reason is that the

exchange calculated by selecting the switching points from the MH loop is very subjective and this may introduce some difference. Other factors include different batch of wafers from deposition and also different annealing, may also introduce some change in exchange bias. Comparing the exchange bias in the order of several hundred, 10~20 Oe difference is acceptable.

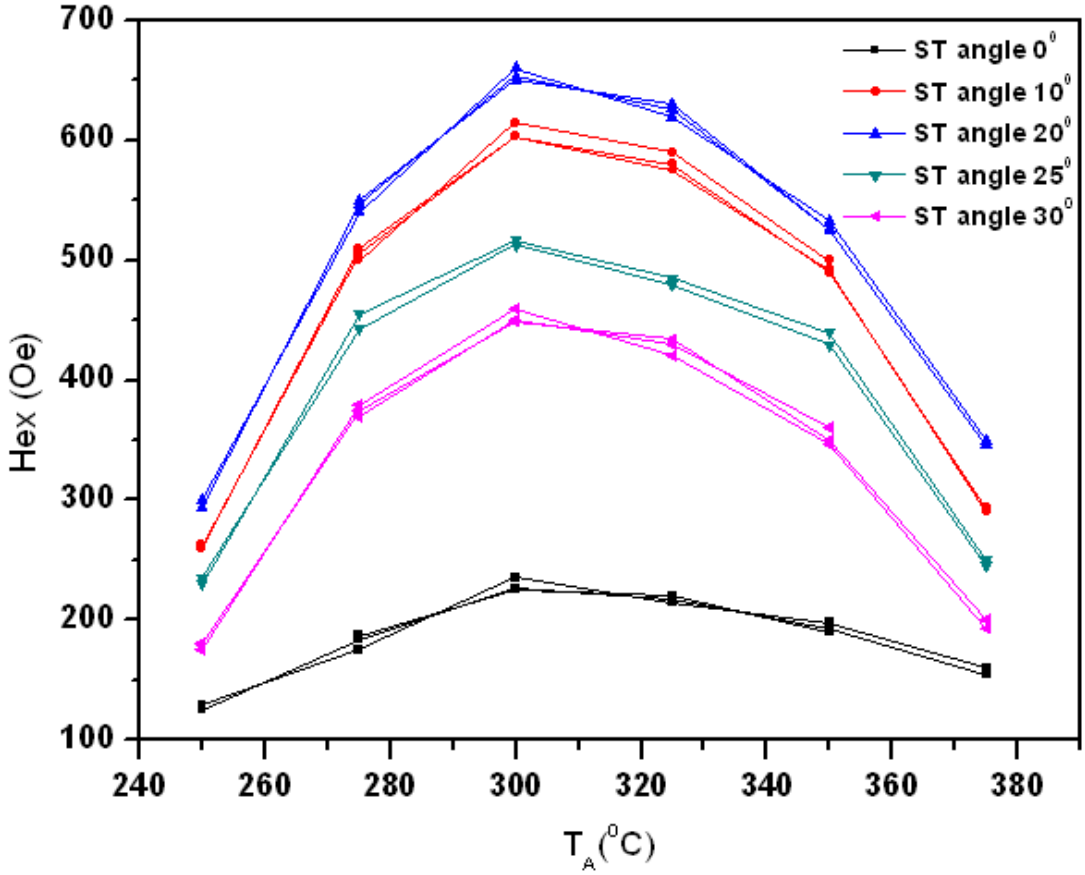

Fig. 4.4. Repeatability study of the effect of annealing for samples deposited at ST angle 0°, 10°, 20°, 25° and 30°. 10~20 Oe difference in exchange bias was observed for each measurements.

These results demonstrated that the new Aviza StratIon *fx*P IBD system is capable of producing exchange biased layers as good as the Nordiko IBD machine could produce.

4.2 MTJs with Al-O barrier deposited by IBD system

An Al-O MTJ stack with layer structure of Ta (5 nm)/Al (30 nm)/Ta (5 nm)/PtMn (20 nm)/CoFe (2.5 nm)/Al (0.8 nm + oxidization time)/CoFe (1.5 nm)/Ta (5 nm)/Al (30 nm)/Ta (5 nm) deposited by the new Aviza IBD tool after the optimization of the exchange bias in PtMn/CoFe was processed for microfabrication and TMR measurements in Plymouth.

4.2.1 Microfabrication process of MTJ devices

The microfabrication procedure of MTJs using lithography techniques has been described in Chapter 3. For convenience, the processing route is summarized below. Magnetic field annealing was first carried out for the MTJ stack after it was deposited. Then the normal four-mask layer processing is used to complete the microfabrication of the MTJ devices.

- Layer 1: Junction mesa areas are defined by Mask #1, and then patterned by ion milling to over the barrier, as shown in Fig. 4.5(a).
- Layer 2: Bottom electrodes are defined by Mask #2, followed by ion milling as shown in Fig.4.5 (b). All area except for the bottom area are etched into the substrate.
- Layer 3: Areas for SiO_2 insulating layer deposition are defined by mask #3, followed by deposition and lift-off of the SiO_2 insulation layer, as shown in Fig.4.5 (c). The SiO_2 is deposited everywhere in the wafer except leaving one window on the mesa and two windows on the bottom electrode. Two probes of the four probes for the TMR measurement can be put on the two windows of the bottom electrode after the contacting Cu pads are deposited.
- Layer 4: Top electrodes are defined by Mask #4, followed by deposition and lift-off of Cu electrodes, as shown in Fig. 4.5(d).

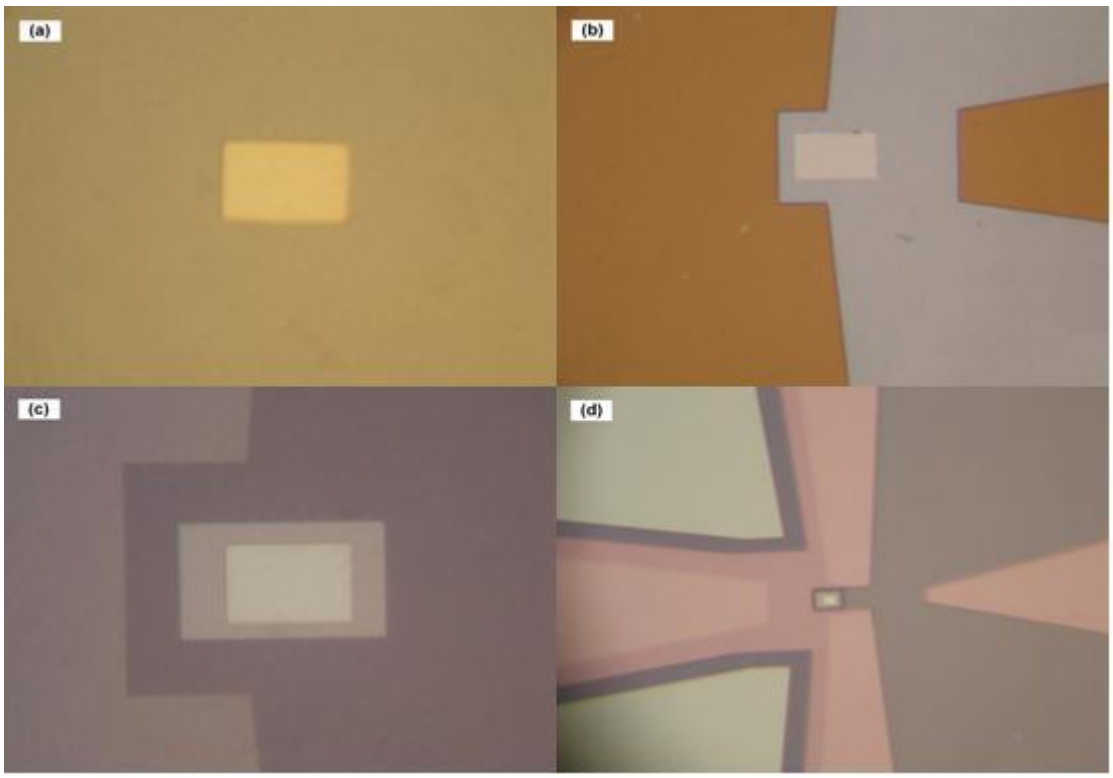

Fig. 4.5. Pictures showing the four-mask layer processing of MTJ devices: (a) junction mesa defined by ion milling, (b) bottom electrode defined by ion milling, (c) SiO_2 insulating layer deposited by lift-off, and (d) top electrodes defined by lift-off of Cu. [The mesa is $20\mu m \times 30\mu m$].

Upon the completion of the four-mask layer microfabrication process, the devices are ready for the four-point-probe TMR measurements. However, great care needs to be taken in each step to ensure the success of the subsequent steps and the final devices. The most challenging part is the ion milling of the junction mesa, for which much time was spent. The milling depth and uniformity of the junction mesa is quite important for the TMR ratio. The ideal milling depth is to reach the top surface of the pinned layer, in other words, just etch through the barrier layer. Under-etching means that there is no sensing current across the tunnel barrier during TMR measurement resulting in very low resistance and no TMR. Over-etching may result in a very thin, or even broken bottom electrode causing an open circuit during TMR measurement. A less severe over-etch is still unacceptable as the re-deposition of the etched materials on the side walls of the junction mesa may cause a shunting effect on the sensing current between the top and

bottom FM layers, resulting in reduced or no MR. As there was no milling end point detection system available in the ion miller we have, the milling depth could only be controlled by calibrated milling rate and milling time. To achieve an accurate control of the milling depth, it requires accurate determination of the layer deposition rate, layer thickness, the milling rate for each layer and the uniformity of milling rate across the wafer. All the deposition and milling rates, layer thicknesses and milling depths were carefully calibrated by AFM.

Due to the limitations of the gun diameter and its milling profile, it is not possible to obtain a uniform milling depth across a 2 inch wafer. By adjusting the position of the substrate holder, beam angle and milling parameters, it is possible to obtain a uniform milling area of 1 inch diameter in the middle of the substrate. Other issues including the photo-resist removal were discussed in Chapter 3.

4.2.2 TMR measurements

Due to the number of layer processing steps involved, it takes at least a week for completing the microfabrication of an MTJ wafer before the TMR measurements. In order to make sure that we do not waste our time on bad samples, a single step patterning process in combination with a 2-point probe measurement technique was developed for pre-examination of MTJ stacks just to see whether they have TMR so that we could decide whether it is worth continuing the microfabrication for that batch.

The TMR properties of MTJ devices are normally measured by a four-point-probe technique as shown in Fig. 3.23 in Chapter 3, in which a constant current is applied to the two outer probes and the resistance of the MTJs is measured by the two inner probes. The advantage of this technique is that the contact resistance at the source terminals is eliminated and the measured resistance is the device’s resistance. However, two- or

three –point-probe measurements could be used just for a rough estimation of the TMR although the magnitude of the measured TMR is not accurate as the contact resistance is included in the measurements. The mesa itself cannot be measured as it is too small and in the micron range. However, the patterns for the bottom electrode are large enough for the probes to be placed on and thus could be used for the TMR estimation. So for each wafer, if we start with the patterning using mask #2, it is possible to pre-check the TMR after ion milling. We call this one-step patterning method.

There will be some change about the microfabrication route to use the one-step pattering method, mainly on mask #1 and #2. In a standard microfabricaiton MTJ route, the mesa is etched first using mask #1. The depth of the etching will be stopped just over the barrier, about 43 nm. Then mask #2 is used and the bottom electrode is defined with etching depth down to the substrate, about 58 nm. After the second etching, a total of the MTJ thickness of 101 nm is etched away in the non-bottom area (The bottom electrode is the mesa's bottom electrode and so the mesa is within the bottom electrode). The reason we etched the entire MTJ stack in the non-bottom electrode area is because we want there is no overlap area between the top electrode and the bottom electrode except the mesa area. Thus the shorting possibility between the top and the bottom electrode is reduced. Mask #3 the SiO_2 is to insulate the bottom and top electrode except the mesa area. If for mask #2 the non-bottom electrode area is not etched down to the substrate and still has some metal left (part of the bottom electrode) and if there is a very small trace of contamination on mask #3 in the top bottom area, then the quality of the SiO_2 is poor and there will be shorting for the sample as the top and bottom area are connected. So it is better to etch down to the substrate after the second etching. Mask #3 and mask #4 are followed to complete the microfabrication.

For the one-step patterning method, in order to have a larger ‘mesa’ area for the probe to put on, we used the bottom electrode mask #2 as the junction ‘mesa’ to measure the TMR using two- or three- probe method. Thus, this bottom electrode shape ‘mesa’ needs to be etched until passing the barrier, 43 nm. At this time, one can see whether this sample shows TMR or not. If it shows TMR, the real junction mesa needs to be created using mask #1 and etch away about 43 nm. Together with the first etch of 43 nm, it is about 86 nm etched away, leave about 101-83=18 nm in the non-bottom electrode area. To solve this problem, a re-etch for the bottom electrode of 18 nm is done after the wafer shows TMR. And thus the mesa using mask #1 etching 43 nm as normal can be used. The following process of Mask #3 and Mask #4 can be used as usual for the completion of the microfabrication.

In brief, instead of milling the junction mesa in the first step as shown in Fig.4.5 (a), the mask for the bottom electrode is milled first to the depth of the mesa for the TMR estimation by two or three point-probe-measurements. We found a TMR of 1.3% after one-step milling for the sample above and 13.9% after the completion of the whole microfabrication as shown in Fig.4.6 (a) and Fig.4.6 (b) measured in low magnetic field. A high field measurement by the four-point probe is shown in the inset in Fig.4.6 (b).

It was a good result of getting TMR of 13.9% for the newly built IBD tool before the optimization of the material and parameters. It should be noted that Al was used as a bottom electrode which is not ideal as it is rough and may affect the quality of the interfaces of the devices and result in low TMR. But Al was the only material available at that time for that machine. If targets such as Ru, MgO, CoFeB, etc. were used, the TMR would be much higher.

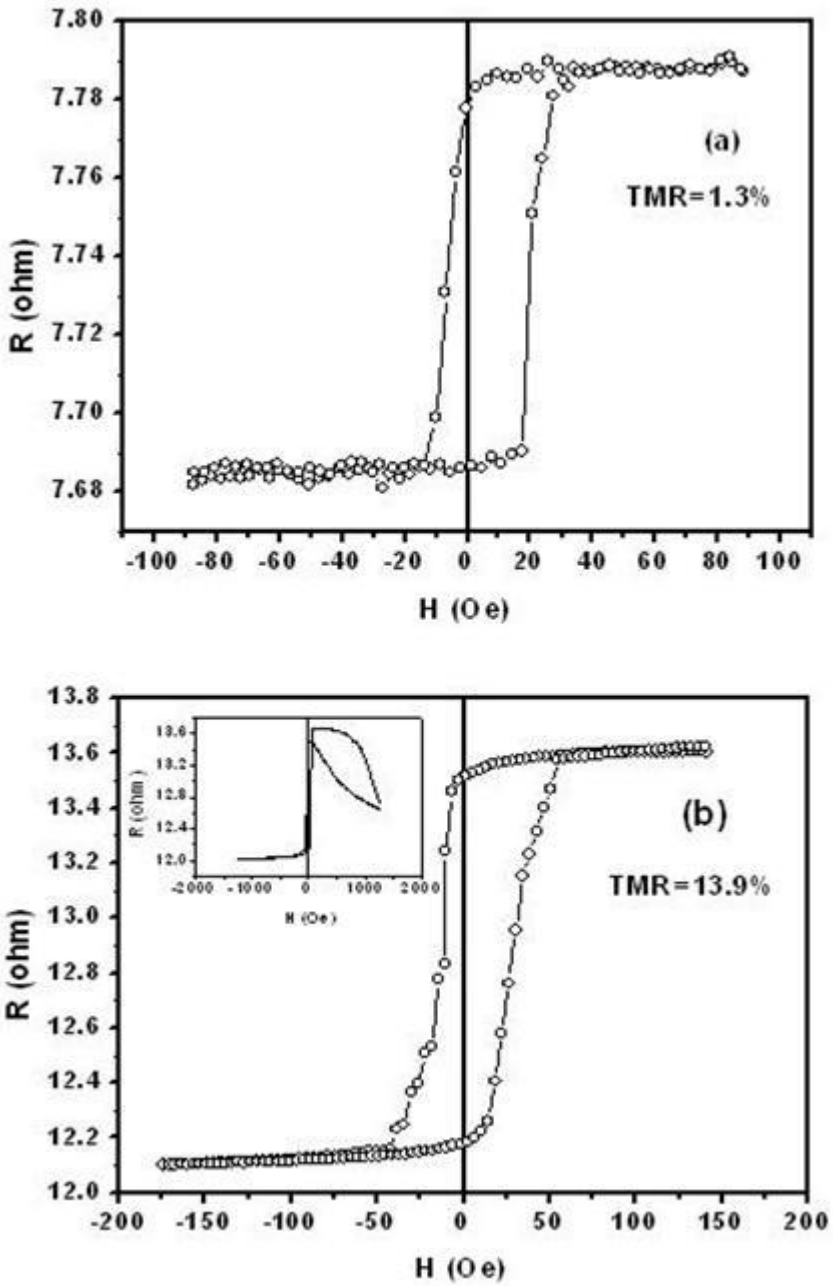

Fig. 4.6. TMR curves measured by 3-point probe after one step milling (a), and 4-point probe after the whole microfabrication (b), for sample Ta (5 nm)/Al (30 nm)/PtMn (20 nm)/CoFe (2.5 nm)/Al (1 nm + oxidized 16 seconds)/CoFe (1.5 nm)/Ta (5 nm)/Al (30 nm)/Ta (5 nm) provided by Aviza Technology. Inset in (b) is the high field MR measurement of this sample.

4.3 Summary

By participating in the DTI MNT project, the author has contributed to the development of the process conditions for the deposition of the MTJs and their associated magnetic

layers. The PtMn/CoFe exchange bias systems were systematically studied with magnetic field annealing and VSM MH loop characterization. An Exchange bias field of up to 650 Oe was obtained for the Ta (10 nm)/ PtMn (20 nm)/ CoFe (3 nm)/Ta (10 nm) stack after magnetic field annealing at 300 ^{o}C for 2 hours. The photolithographic and ion milling processes for the microfabrication of the MTJs with an Al-O barrier layer was developed and TMR of these devices were successfully measured using the four-point probe system.

5 Enhanced exchange bias in IrMn/CoFeB systems

When the Nordiko 9550 deposition tool was installed in Plymouth, we started to study the exchange bias in IrMn/CoFeB. As discussed previously in Chapter 2, CoFeB film has been widely used as a ferromagnetic (FM) electrode material for MTJs with an MgO barrier [33]. Due to its highly spin polarised Δ_1 Bloch states of the majority spin and the lack of Δ_1 states of the minority spin at Fermi level, plus its extremely smooth interface, MTJs made with CoFeB as both top and bottom FM electrodes exhibit the highest tunnelling magneto-resistance (TMR) [29]. The ability to obtain large exchange bias field from a system with CoFeB layers is therefore of great technological importance [101; 102; 103], which was one of the objectives of this part of the work. Our initial experimental findings of the difference in exchange bias field between material systems of IrMn/CoFeB and IrMn/CoFe provide us with a unique opportunity to investigate into the physics origin for the differences and hence to understand the origin of exchange bias from the study of these two especial material systems.

Although the phenomenon of exchange bias was discovered over 50 years ago[40] and has been widely used in practical device applications, the understanding the physics behind this phenomenon is still elusive. However, there have been some marked progresses on the topic in the past decade with experimental findings in association of exchange bias with interfacial uncompensated spins. For example, the correlation between exchange bias and the pinned uncompensated spins has been reported by Ohldag *et al* [51], characterized as a vertical off-set of the AFM Mn MH loops obtained by element specific x-ray magnetic circular dichroism (XMCD). There have been very recent reports to give more intuitive pictures of the pinned interfacial spins and their

corelations with H_{ex} based on the XMCD measurements of $Mn_{52}Pd_{48}$/Fe[53] and permalloy/CoO bi-players[58]. However, such an understanding is still far from conclusive. Tsunoda et al[48] reported that neither pinned uncompensated AFM spins nor correlation between the XMCD signals and the strength of exchange anisotropy could be observed from the ordered and disordered IrMn/CoFe bilayer system with significantly different H_{ex} values. These intriguing developments continue to motivate ongoing investigations into these topics.

We aimed to obtain higher exchange bias field in IrMn/CoFeB structure in preparation for the fabrication of MgO MTJs with CoFeB as both the top and bottom (pinned and free) electrodes. As it is quite difficult in obtaining exchange bias in top pinned CoFeB/IrMn structure [102; 104; 105] due to the difficulties in formation of (111) texture in the AFM layer, the bottom pinned structure of IrMn/CoFe/Ru/CoFeB is normally choosed, where CoFe/Ru/CoFeB is a synthetic antiferromagnetically coupled. As Ru target is not available in our PVD tool, we would like to see if simple bottom pinned structure IrMn/CoFeB could achieve a relatively high exchange bias. Exchange bias in IrMn/CoFe structure has been studied in comparison with the IrMn/CoFeB structure.

5.1 Sample preparation and characterization

Six targets are installed in Nordiko 9550 PVD depositon tool: Ta, Cu, MgO, $Ir_{20}Mn_{80}$, $Co_{70}Fe_{30}$, and $Co_{40}Fe_{40}B_{20}$. Ta buffer layer and seed layer such as NiFe, Cu, Ru etc are always used to promote the (111) texture formation in IrMn layer [106; 107]. Considering the targets available, CoFe and Cu were used for the seed layer.

Samples with structure of Ta (5 nm)/Seed layer (t_s nm)/IrMn (5 nm)/FM (t_f nm)/Ta (5 nm) were deposited on 4 inch silicon oxide substrate at room temperature by Nordiko 9550 PVD deposition tool using Ar gas, where FM = CoFe or CoFeB. The base pressure of the system is 2×10^{-8} Torr. A magnetic field of about 60 Oe was applied on one direction of the FM layer and AFM layer to introduce an easy axis in the FM layer. The seed layer is either CoFe or Cu. Magnetic field annealing was carried out at T_A from 250 ºC to 400 ºC for 1 hour in an external applied magnetic field of 5 kOe along the FM easy axis. All the samples were cut to 1cm × 1.5 cm and put into a stainless steel box for annealing, with field applied along the easy axis direction in the FM layer. H_{ex} was obtained from the MH loops measured by VSM and J_k was calculated by equation $J_k = M_s t_f H_{ex}$, where M_s is the saturation magnetization and t_f is the thickness of the FM layer. The film deposition rate was measured by AFM through lift-off and the composition of the FM layers was verified by Energy-dispersive x-ray spectroscopy (EDS). The deposition rate of each layer is caliberated once a week to ensure the stability and repeatability of the deposition process. The microstructure of the layers was also examined at Oxford Materials using high a high angle annular dark field (HAADF) image and cross-sectional high resolution TEM (HRTEM). The film composition and its distributions were also analysed with Secondary Ion Mass Spectrometer (SIMS) at Oxford Materials. The interfacial spins were analysed at Stanford Synchrotron Facility using a highly sensitive XMCD spectroscopy in TEY detection mode. Spectra were taken at the Mn and Co L_2 and L_3 edges, respectively. Samples for XMCD measurements were specially made to have a Ta cap layer thickness of 2 nm to ensure the soft x-ray can reach the top IrMn/CoFeB interface.

5.2 Exchange bias in IrMn/CoFe and IrMn/CoFeB

The exchange bias field H_{ex} and exchange energy constant J_k were measured and calculated for samples with different layer structures and annealed at different temperatures. Much enhanced exchange bias field was obtained from IrMn/CoFeB bottom pinned exchange biasing layers with seed layer of either CoFe or Cu. Initially we did not expect much difference in exchange bias between IrMn/CoFeB and IrMn/CoFe. But after it is found that much enhancement in IrMn/CoFeB and we decided it is a good opportunity to investigate the origin of exchange bias and the difference between IrMn/CoFe and IrMn/CoFeB system. Due to the large grain size of seed layer Cu, especially after annealing, most of the samples for comparision of IrMn/CoFe and IrMn/CoFeB are deposited on CoFe seed layer.

Fig. 5.1 shows the typical MH loops of 4 selected samples. Samples 1, 2, and 3 were deposited on a 3.4 nm CoFe seed layer and sample 4 was deposited on a 3.4 nm Cu. Sample 1 and 2 had the same layer structure CoFe/IrMn/CoFeB, sample 3 CoFe/IrMn/CoFe and sample 4 Cu/IrMn/CoFeB. Sample 1, 3 and 4 were annealed at the same temperature of 350 ℃ for 1 hour in a 5 kOe field and sample 2 were annealed at 250 ℃ for an initial annealing temperature study for structure CoFe/IrMn/CoFeB. The bottom half of the MH loops for the first three samples is the contribution from the CoFe (3.4 nm)/IrMn (5 nm) interface with H_{ex} of around 250 Oe. Enhanced H_{ex} was observed from the top IrMn 5nm/FM 3nm interface annealed at 350 ºC for 1 hour, with maximum H_{ex} of around 988 Oe for IrMn 5nm/CoFeB 3nm (sample 1), while H_{ex} of 500 Oe for IrMn 5nm/CoFe 3nm (sample 3). H_{ex} with similar magnitude about 1000 Oe as sample 1 was also observed for IrMn 5nm/CoFeB 3nm with Cu seed layer with the same annealing conditions (sample 4); see the MH loop in the inset of Fig. 5.1. This excludes the factor that the enhancement of the H_{ex} may be caused by the spin

propagation from the bottom magnetic seed layer as in [108] as Cu is non-magnetic. In both cases, the larger H_{ex} is accompanied by an increased coercivity of the CoFeB films. The H_{ex} for sample 2 (the same layer structure as sample 1, but was annealed at a lower temperature 250 ºC for 1 hour) is 756 Oe.

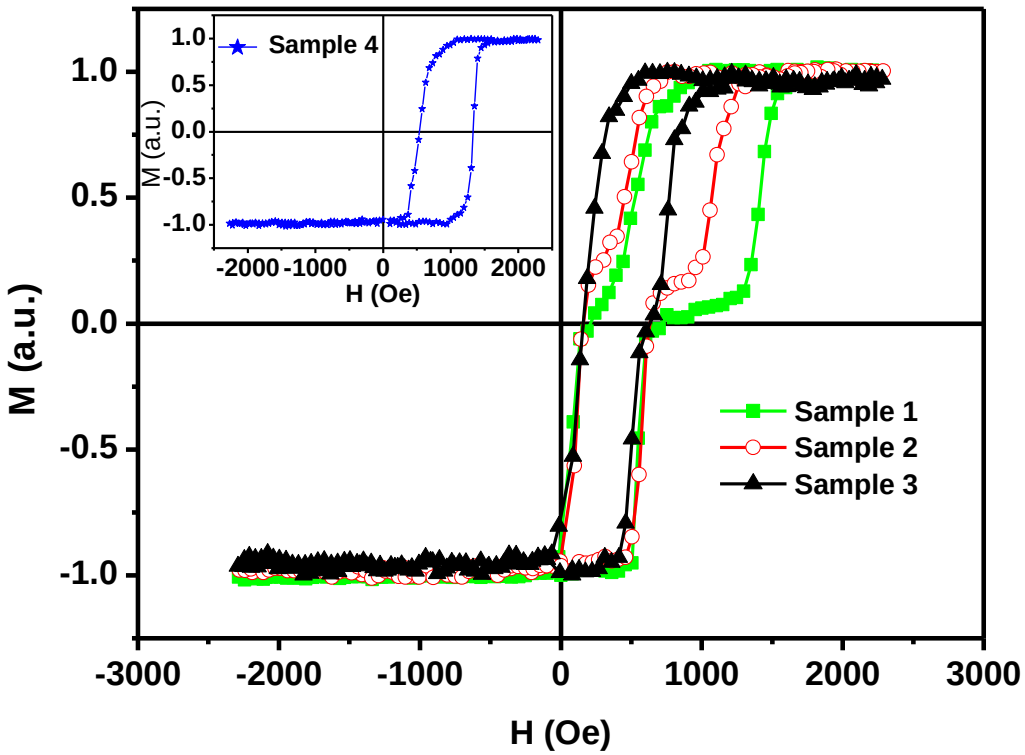

Fig. 5.1. MH loops of four selected samples. Sample 1 has a layer structure SiO_2/Ta (5 nm)/CoFe (3.4 nm)/IrMn (5 nm)/CoFeB (3 nm)/Ta (5 nm) annealed at 350 °C for 1 hour. Sample 2 has an identical layer structure as sample 1, but annealed at 250 °C for 1hour. Sample 3 has a layer structure Si//Ta (5 nm)/CoFe (3.4 nm)/IrMn (5 nm)/CoFe (3 nm)/Ta (5 nm) annealed at 350 °C for 1 hour. Sample 4 has a layer structure Si//Ta (5 nm)/Cu (3.4 nm)/IrMn (5 nm)/CoFeB (3 nm)/Ta (5 nm) with T_A of 350 °C for 1hour. The lower half of the MH loops for samples 1, 2& 3 is the contribution from the CoFe seed layer.

It can be seen that for the same annealing conditions, top pinned CoFeB showed much higher exchange bias than that of the top pinned CoFe (998Oe vs 500Oe). In the following, we focused on the two layer structures substrate SiO_2/Ta/CoFe/IrMn/CoFeB/Ta and substrate SiO_2/Ta/CoFe/IrMn/CoFe/Ta to find out

why there is so much difference on exchange bias for CoFeB and CoFe. A systematic annealing temperatures and layer thickness dependence were studied.

5.3 Effect of annealing temperature on exchange bias

The dependence of H_{ex} and J_k on T_A from 250 ºC up to 400 ºC for sample 1 (IrMn 5nm/CoFeB 3nm) and sample 3 (IrMn 5nm/CoFe 3nm) are plotted together in Fig. 5.2. As can be seen from the figure, the H_{ex} (curves with solid symbols) and J_k (curves with hollow symbols) of IrMn (5 nm)/CoFeB 3nm is in general larger than that of IrMn 5nm/CoFe 3nm for all annealing temperatures. The H_{ex} initially increases almost linearly with T_A up to 350 ºC, where there is a peak for both cases before falling off for T_A >350 ºC. The J_k follows a similar trend with a maximum value of 0.37 erg/cm^2 for IrMn/CoFeB against 0.26 erg/cm^2 for IrMn/CoFe annealed at 350 ºC. The possible oxidation or intermixing in the films caused by annealing which may contribute to the increase in H_{ex} at 350 ºC as reported in [109] can be ruled out in this case from the unchanged saturation magnetization of the samples measured by VSM before and after annealing. This was further confirmed by the same enhanced H_{ex} and J_k values obtained from samples with Ta capping layers of up to 20 nm.

The enhancement of H_{ex} and J_k in these samples is accompanied by a moderate increase of coercivity H_c, as also shown in Fig. 5.1. The H_{ex} and J_k for the samples annealed above 350 ºC are reduced, which is perhaps associated with the interfacial diffusion caused by the high annealing temperature [110] as it was evident by the sharp increase of H_c values of these samples when T_A >350 ºC. Such an annealing temperature dependence profile of H_{ex} and J_k is in agreement with other similar works [111]. Typical MH loops of the sample annealed at 350 ℃ and 400 ℃ is also shown in Fig. 5.3, in

which it clearly showed that the H_c of both FM layers CoFe and CoFeB has increased considerably due to interlayer diffusion at higher annealing temperature of 400 ℃.

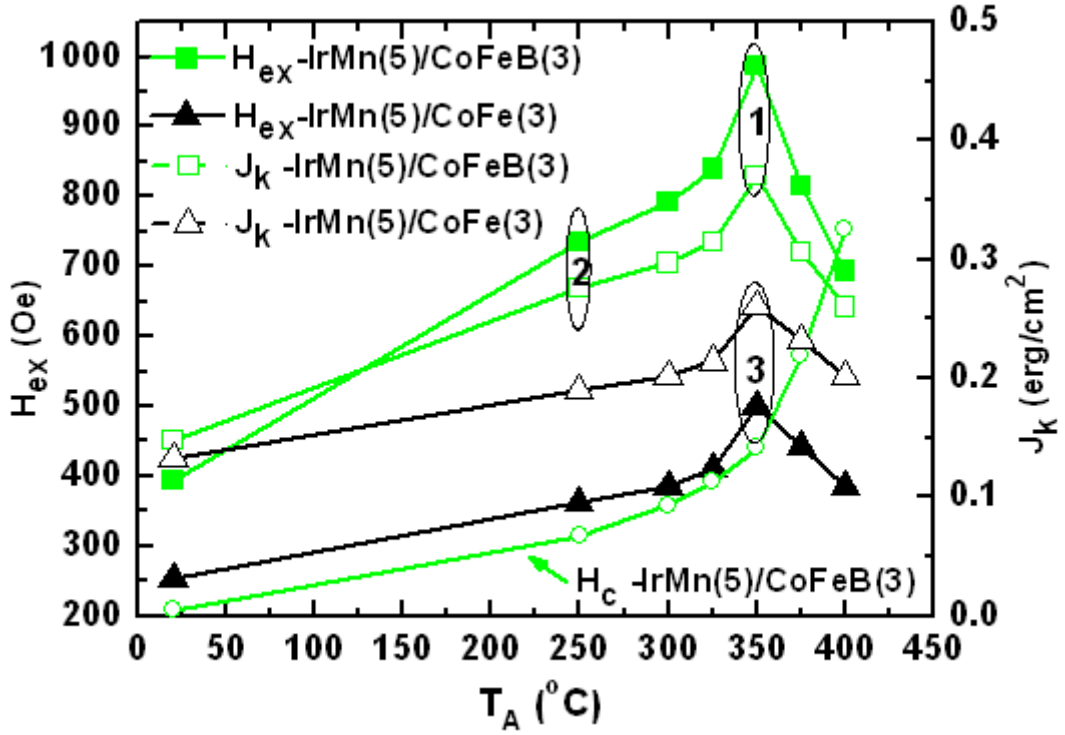

Fig. 5.2. Dependence of H_{ex} (Solid line and mark) and J_K (dashed line and hollow mark) on annealing temperature for samples with layer structures of CoFe (3.4 nm)/IrMn (5 nm)/CoFeB (3 nm) (square mark) and CoFe(3.4 nm)/IrMn (5 nm)/CoFe (3 nm) (triangle mark), respectively. Also shown, the dependence of H_c on annealing temperature for the sample with layer structure of CoFe (3.4 nm)/IrMn (5 nm)/CoFeB (3 nm). Number 1, 2 and 3 represents the three samples in Fig. 5.1.

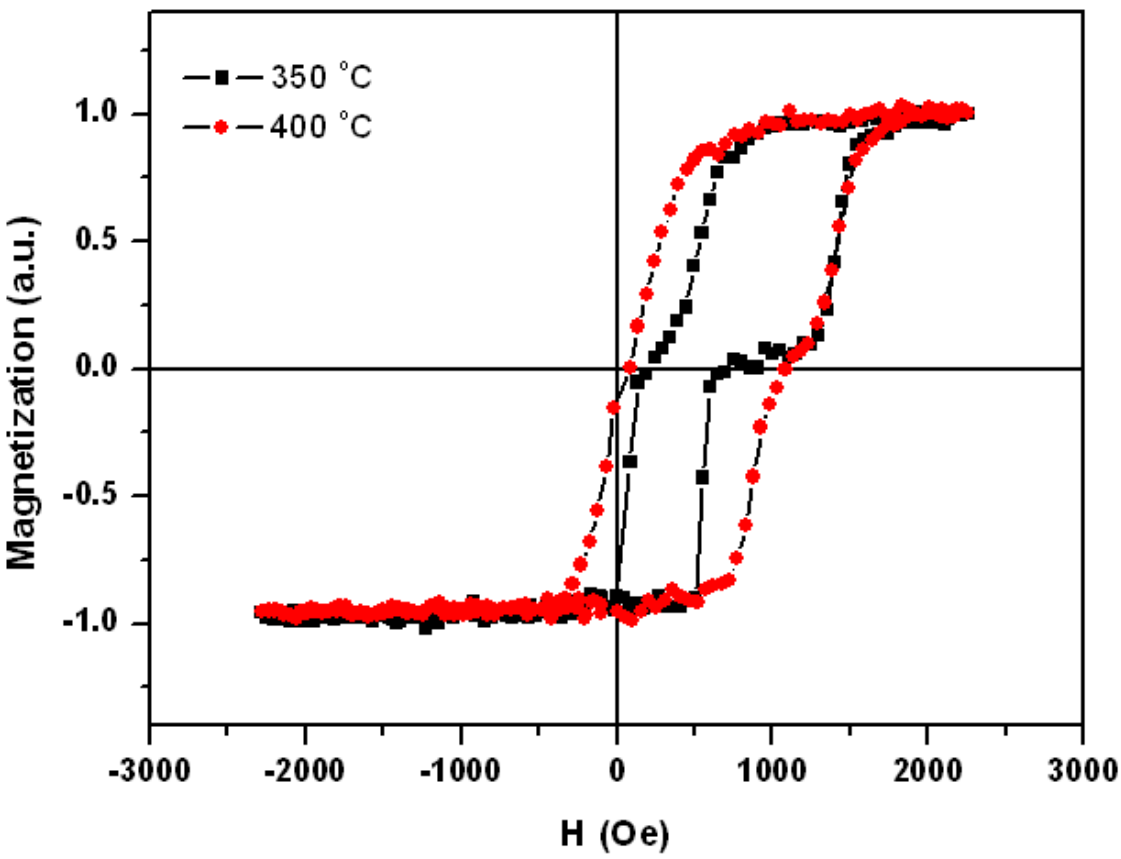

Fig. 5.3. MH loops of CoFe(3.4nm)/IrMn(5nm)/CoFeB(3nm) annealed at 350 ℃ and 400 ℃ for 1 hour.

5.4 Dependence of exchange bias on seed layer thickness

As the seed layer is to promote the formation of (111) texture in IrMn layer, the quality of which will affect the magitutde of exchange bias[106], we investigated the effect of the thickness of seed layer CoFe on the exchange bias on IrMn/CoFeB with CoFeB thickness of 3 nm and 2 nm. In the same time, the thickness effect of CoFeB on its exchange bias is also studied.

The dependence of H_{ex} (solid line) and J_k (dashed line) on the CoFe seed layer thickness is shown in Fig. 5.4 for samples with 3 nm and 2 nm CoFeB upper FM layers annealed at 350 ºC. In both cases, the H_{ex} and J_k initially increases with the CoFe seed

layer thickness, reaching a maximum before falling slightly. The optimum CoFe seed layer thickness for maximum J_k is in the range of 3.4 ~ 4 nm, which is perhaps determined by the combined effect of the two competing factors – the required minimum seed layer thickness for the establishment of the (111) orientation of the IrMn AFM layer and the inverse dependence of H_{ex} on grain sizes of the IrMn AFM films[72]. The slight reduction of H_{ex} with increased seed layer thickness for t_s may be attributed to the inverse dependence of H_{ex} on grain sizes. Grian size often varies with film thickness. According to a microstructural evolution study, the mean grain size increases with film thickness. The exchange anisotropy J_k appears to be very sensitive to the subtle changes (in the submicron regime) of grain sizes and crystallographic orientations of the seed layers, which in turn affect the grain sizes and interfacial structures of the following IrMn and CoFeB layers.

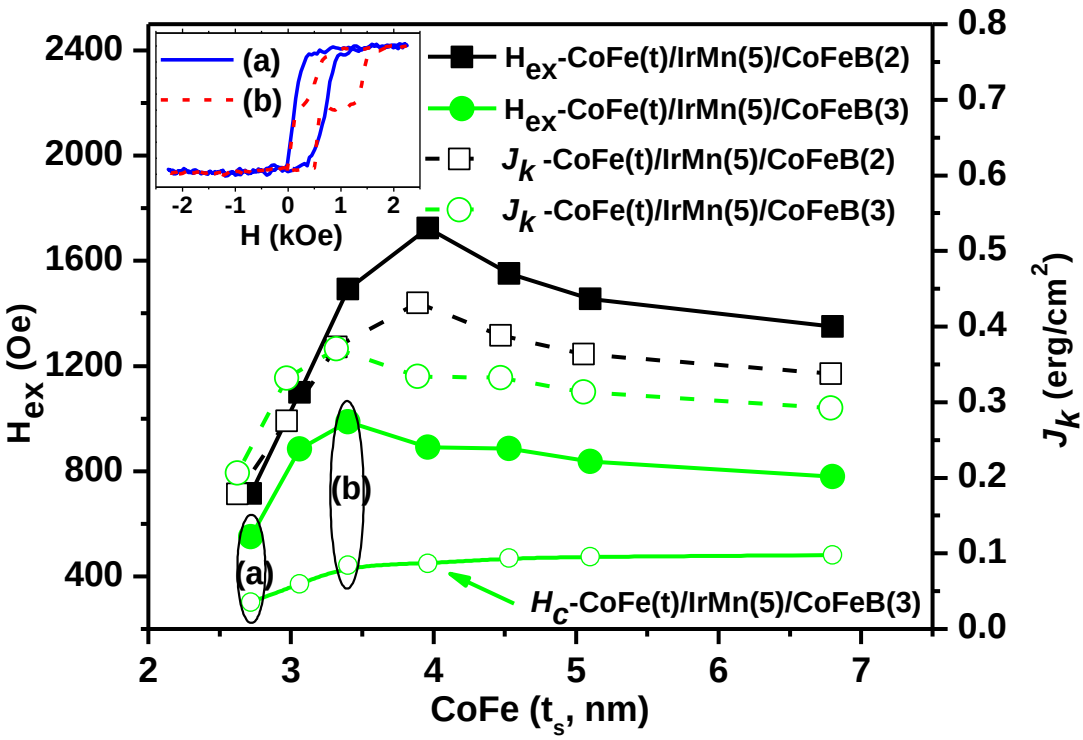

Fig. 5.4. Dependence of H_{ex} (solid line and mark) and J_k (dashed line and mark) on the CoFe seed layer thickness for samples with 3 nm (circular mark) and 2 nm (square mark) upper CoFeB layers annealed at 350 °C. Also shown, the dependence of H_c on the CoFe seed layer thickness for samples of /IrMn (5

nm)/CoFeB (3 nm). The inset shows the MH loops of two /IrMn (5 nm)/CoFeB (3 nm) samples corresponding to data points (a) and (b).

Samples with 2 nm thick CoFeB upper layers exhibit larger exchange bias with maximum H_{ex} and J_k of 1720 Oe and 0.43 erg/cm^2, respectively in comparison with 988 Oe and 0.37 erg/cm^2 for samples with 3 nm CoFeB. This indicates that the exchange anisotropy is an interfacial effect and the strength of which is inversely proportional to the distance between the FM and AFM spins.

Also shown in Fig. 5.4 is the dependence of H_c on seed layer thickness for the IrMn 5nm/CoFeB 3nm samples annealed at the same conditions. The increase of H_c with seed layer thickness is in line with the increase of H_{ex} and is particularly apparent when seed layer is less than 4nm. The increase of H_c could be introduced by element interfacial diffusion due to extremely high temperature annealing as shown in Fig.5.3, but it is not the case here. Two samples with the same top pinned structure IrMn (5nm)/CoFeB (3nm) on different CoFe seed layer thickness (2.8 nm and 3.4 nm) are annealed at the same condition. If there is diffusion then the diffusion would have the same effect on H_c on each sample. That means whatever the exchange bias of each sample; the two samples would have about the same H_c which is not true here. This is more clearly shown in the inset of Fig. 5.4 in which the MH loops of two samples are corresponding to data points (a) and (b), where the H_c is 300 Oe for the sample on a 2.7 nm seed layer with H_{ex} of 450 Oe, in comparison with 440 Oe for that on a 3.4 nm seed layer with H_{ex} of 900 Oe. These results suggest that the increase of H_c in these samples is largely dependent on the increase of H_{ex}. Thus the thickness of the seed layer will affect the exchange and also covercivity, which should be considered in the application of the exchange bias in spintronic devices.

5.5 TEM analysis

It is clear from the MH loop measured by VSM that IrMn/CoFeB showed better exchange bias and anisotropy than that of IrMn/CoFe. It is necessary to investigate the micro-origin of the reason by assisting of some structure and depth analysis tool. We contacted with Oxford Materials and Standford Synchrotron Radiation Laboratory for collaboration.

Two samples were submitted to Oxford Materials for TEM analysis. The two samples are sample 1 and sample 3 in Fig.5.1, one with structure SiO_2/Ta/CoFe/IrMn/CoFeB/Ta (sample 1) and the other one with structure SiO_2/Ta/CoFe/IrMn/CoFe/Ta (sample 3), both annealed at the 350 ℃ for 1 hour.

Fig.5.5 shows the High Angle Annular Dark Field (HAADF) image on the left and also the intensity line scans of the selected areas on the right for the two samples. It can be seen that there are distinct layers shown for both samples and there is no significant intermixing between the FM and AFM layers. There is an approximate agreement between nominal layer thicknesses. The estimated thickness from the analysis for Sample 1 is Ta 5.8 nm, CoFe 3.75 nm, IrMn 5.7 nm, CoFeB 2.9 nm and Ta 2.3 nm plus 9 nm oxidized Ta. The estimated thickness from the analysis for Sample 3 is Ta 6 nm, CoFe 3.6 nm, IrMn 5.4 nm, CoFeB 2.6 nm and Ta 2.3 nm plus 10 nm oxidized Ta. The error is about 0.5 nm. One can see the Ta layer was partially oxidized with some of the Ta leaving. The magnetic properties of the sample are not affected by the oxidization.

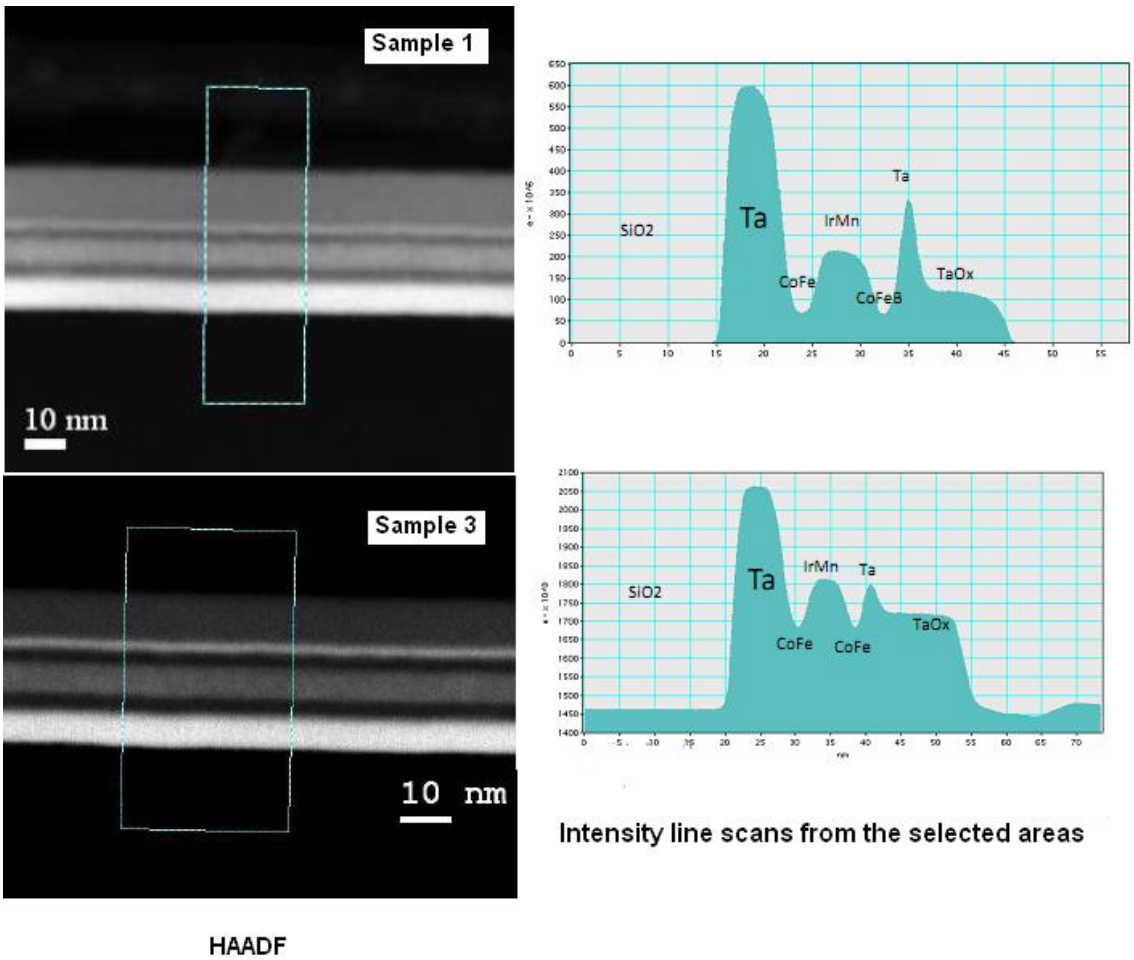

Fig. 5.5 HAADF and intensity line scans from the selected areas of sample 1 and sample 3

Except for the HAADF and line scan analysis, our original intention was to use the SIMS depth profiling to examine the interlayer diffusion. As each layer in the sample is in the order of only several nm and in order to achieve the element diffusion after thermal annealing, the SIMS analysis needs to be carried out with atomic depth profiling resolution. However, this was not achieved due to the fact the resolution used in the SIMS experiment was too rough. No further work was possible because of the lack of new samples due to the change of the Nordiko 9550 machine configuration.

Fig.5.6 shows cross-sectional HRTEM images and the SAED patterns of sample 1 and sample 3, respectively. It was observed that the FM/AFM/FM layers of both samples

are in good epitaxy. Local epitaxial growth between the upper AFM/FM layers can be clearly seen from these images. The majority of the bottom CoFe grains in both samples have (110) orientation, which gives a (111) orientation to the IrMn layer and again a (110) orientation to the upper CoFe or CoFeB layer. Such an orientation relationship was also confirmed by similarity of the interfaces. No significant difference in crystal structure and orientations between the two samples was observed. The upper CoFeB layer which was amorphous when as grown has apparently become polycrystalline with (110) orientation as a result of solid phase epitaxy during annealing. The grain sizes of the upper FM layers in both cases are in the range of 5 +/- 2 nm as determined from the HRTEM images though the numbers of grains measured are limited due to the cross-sectional orientation of the TEM sample. Consequently, the structural origin of the enhanced exchange anisotropy in IrMn/CoFeB compared with IrMn/CoFe structure is not clear from the HRTEM analysis. Since exchange anisotropy is sensitive to the grain and interfacial structures, as indicated by the results in Fig. 5.4, small differences that were not detected by this analysis may explain the large change in magnetic properties.

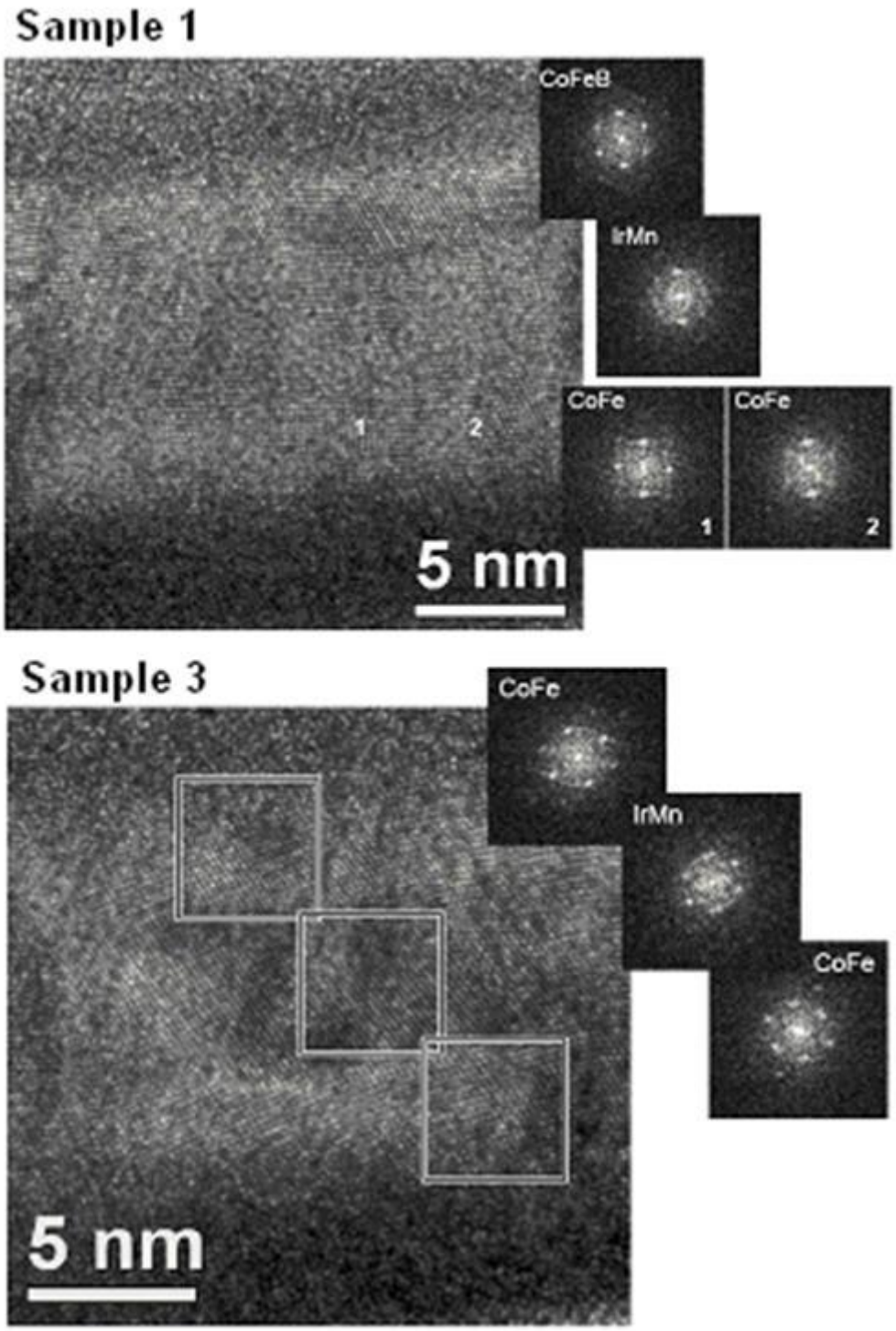

Fig. 5.6 Cross sectional HRTEM images and SAED patterns of sample 1 and sample 3.

5.6 XMCD analysis

Element specific XMCD measurements were carried out for three three samples (samples 1, 2, and 3 as shown in Fig.5.1) at the Mn and Co $L_{2,3}$ edges.

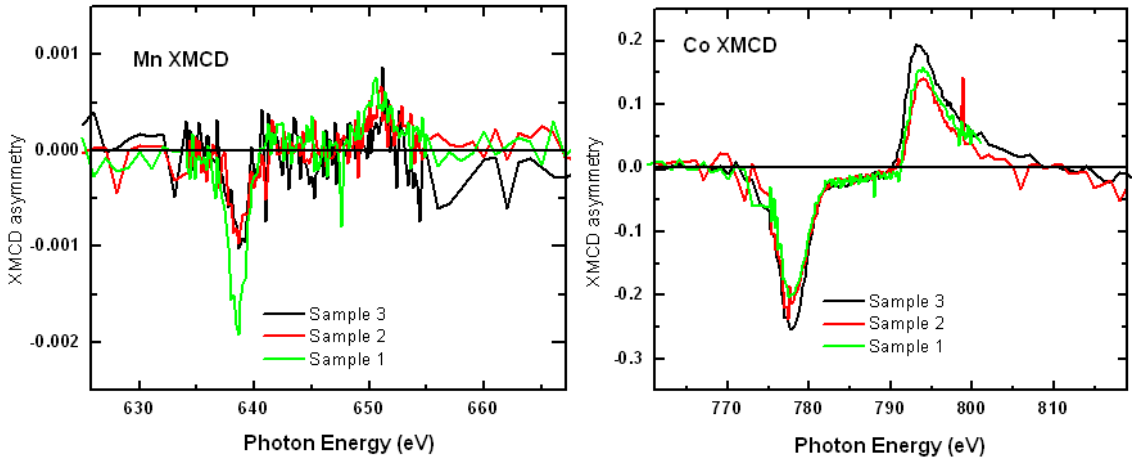

Fig. 5.7 Element specific XMCD asymmetry spectroscopy taken at the Mn (left) and Co (right) L_2 and L_3 edges for samples 1, 2 and 3 corresponding to data points marked in Fig. 5.1.

Fig. 5.7 shows the XMCD spectra for the Mn L2, L3 and Co L2 L3 edges, respectively. The origin of XMCD at the Mn L2 and L3 edges has been investigated previously [48; 51] and it is attributed to the magnetic coupling at the interface between the CoFe layer or CoFeB layer in this work and the IrMn layer. As it can be seen from Fig. 5.7 the Mn XMCD asymmetry exists on all the three samples and the magnitude observed from sample 1 (IrMn/CoFeB annealed at 350 ºC), which is the sample with the strongest exchange anisotropy, is nearly twice as high as that observed from sample 2 (IrMn/CoFeB annealed at 250 ºC) and sample 3 (IrMn/CoFe annealed at 350 ºC). It is also interesting to note that the XMCD signal strength is almost equal for sample 2 and 3 which exhibit markedly different H_{ex} but with similar value of J_k (0.27 erg/cm^2 for sample 2, and 0.26 erg/cm^2 for sample 3, see Fig.5.2). As the bulk IrMn itself exhibits zero XMCD signal due to its noncolinear spin-density wave structure [52; 112], the strength of the XMCD signal represents the amount of the uncompensated AFM spins at

the IrMn/FM interface. Tsunoda *et al* [52] showed the Mn XMCD signal does not increase as the thickness of IrMn increases. They changed AFM layer IrMn thickness in IrMn (t)/CoFe (2.5nm) from 0.5nm to 20nm and the Mn XMCD magnitude does not change too much which means the uncompensated Mn component is localized at the very interface less than a few monolayer (0.5nm about 2.3 monolayer). The results that sample 2 and sample 3 showed similar J_k and same magnitude of uncompensated interfacial Mn spins, both smaller than those of sample1 apparently suggest that the enhanced exchange bias of the IrMn/CoFeB system is associated with increased uncompensated interfacial spins and there exists a quantitative correlation between the XMCD signal strength and the exchange bias anisotropy constant J_k.

Tsunoda *et al* [52] also showed quite large different of Mn XMCD signal when different FM materials were used. For both conditions of Mn XMCD signal not changing too much with different thickness of IrMn and Mn XMCD signal significantly changing with different FM materials, they simulated using a classical Heisenberg model and it is found that the uncompensated Mn spins are localized at the very interface of FM FM and AMF layers and are introduced through the exchange interaction between the two layers, in which, if the interface is atomically flat, the uncompensated spins are purely an interfacial effect and not an alloying effect; if the interface are changed and the exchange interaction will change and the uncompensated spins will change as well.

CoFe and CoFeB are two different FM materials, and the exchange interaction between the FM and AFM interface are different for these two materials. This will introduce different uncompensated Mn spins, although HRTEM did not obtain obvious difference between IrMn/CoFeB and IrMn/CoFe interfaces. The interface is only several ML thick

and it is hard to tell using TMR. Regarding to sample 1 and 2 using the same FM CoFeB layer but annealed at different temperature, the temperature also has an effect on the interface and thus again introduce different number of uncompensated spins.

It is reported by Takahashi *et al* [113] that the magnitude of the uncompensated Mn spins strongly depended on the composition of the FM layer due to the exchange coupling between at the different species of atoms. They showed from Fig. 4 in their work Co70Fe30 showed higher Mn L3 XMCD signal than $Co_{50}Fe_{50}$ with AFM Mn_3Ir. The composition of IrMn CoFe and CoFeB used our work are $Ir_{20}Mn_{80}$, $Co_{70}Fe_{30}$ and $Co_{40}Fe_{40}B_{20}$. Mn XMCD shows higher magnitude for CoFeB/IrMn than CoFe. The different results may be due to the quite different B content and IrMn, which can change the interface as well.

5.7 Summary

In summary, we have studied the bottom pinned exchange bias systems of IrMn/CoFe and IrMn/CoFeB with CoFe seed layer. Enhanced exchange anisotropy has been obtained from samples with IrMn/CoFeB annealed at 350 °C. The enhancement of H_{ex} is accompanied by a moderate increase in H_c. Cross-sectional TEM shows that FM and AFM layers are polycrystalline and textured [110] for CoFe and CoFeB, and [111] for IrMn, respectively. Element specific XMCD spectrum shows a much enhanced uncompensated interfacial spins for IrMn/CoFeB sample with the largest exchange bias field, which may in some way explain the interfacial magnetic origin of the enhanced anisotropy. A quantitative correlation between the XMCD signal strength and the exchange anisotropy constant J_k was observed.

6 MgO MTJs

6.1 Design of MgO MTJ stack layer structures

As introduced in Chapter 2, the essential conditions for obtaining high TMR in MgO MTJ are atomically flat and ultra clean interfaces between FM/MgO/FM, and a highly orientated FM/MgO/FM stack. Six targets have been installed in our Nordiko 9550 PVD sputtering machine: $Co_{40}Fe_{40}B_{20}$, Cu, $Ir_{20}Mn_{80}$, MgO, $Co_{70}Fe_{30}$, and Ta, so the layer structure of MTJ stack should be designed based on these materials according to these requirements. For a top-pinned MTJ layer structure, it is in the sequence of Si/SiO_2/Ta/electrode/FM/MgO/FM/AFM/Ta, for a bottom-pinned structure, Si/SiO_2/Ta/electrode/AFM/FM/MgO/FM/Ta.

As discussed in Chapter 2, it is favorable to use CoFeB as both the free layer and pinned layer in MgO MTJs, but due to the difficulty in obtaining exchange bias in top pinned CoFeB/IrMn bilayers [102; 104; 105], we started with a MgO MTJ stack with one CoFeB as free layer and a top pinned CoFe as the pinned layer having the structure Ta/electrode/CoFeB/MgO/CoFe/IrMn/Ta. The reason to choose the top pinned CoFe/IrMn structure instead of bottom pinned IrMn/CoFe is because the amorphous properties of the as grown CoFeB will provide a smoother surface for the subsequent growth of the layers in the stack which will affect the TMR. The selection of the electrode material is also important as it also has an effect on the smoothness in subsequent layers, which again will affect the TMR ratio of the MTJs. The effect of Cu and CuN electrode materials on TMR will be discussed in the next section 6.2.2 of this Chapter.

As discussed in Chapter 5, we also have investigated the exchange bias in the bottom pinned IrMn/CoFeB system aiming for MgO MTJs with CoFeB as both pinned layer and free layer. MTJ layers are deposited by Nordiko 9550 PVD deposition tool and except for MgO is RF deposited all other layers are deposited by DC power supply.

VSM was initially used to examine the quality of an MTJ stack. The MgO insulating layer should be pinhole free. Fig. 6.1 shows the MH loops of top pinned MTJ stacks with MgO thickness of t =1 nm, 1.5 nm and 2 nm, respectively, for the layer structure of Ta (5 nm)/CuN (30 nm)/Ta (5 nm)CoFeB (3 nm)/MgO (t nm)/CoFe (4 nm)/IrMn (5 nm)/Ta (5 nm). All three samples show two loops, one loop is around the zero field except the one with MgO =1 nm and the other loop is a little bit far away from the the zero field, corresponding to free layer and pinned layer switching. The magnetization switching of the pinned layer and free layer in an MTJ stack should be independent if the quality of the very thin MgO barrier is good. For stack with 1 nm MgO as shown in Fig. 6.1 (a), the magnetization switching of the pinned layer and free layer are not well separated. There may be pinholes existing in such a thin MgO layer or the MgO with 1 nm-thickness is discontinuous and hence the pinned layer and free layer are coupled. This is also why the free layer loop is not around the zero field. As shown in Fig. 6.1 (b) and (c), the loops of the free layer and pinned layer are well separated for MgO barriers with thickness of 1.5 and 2 nm.

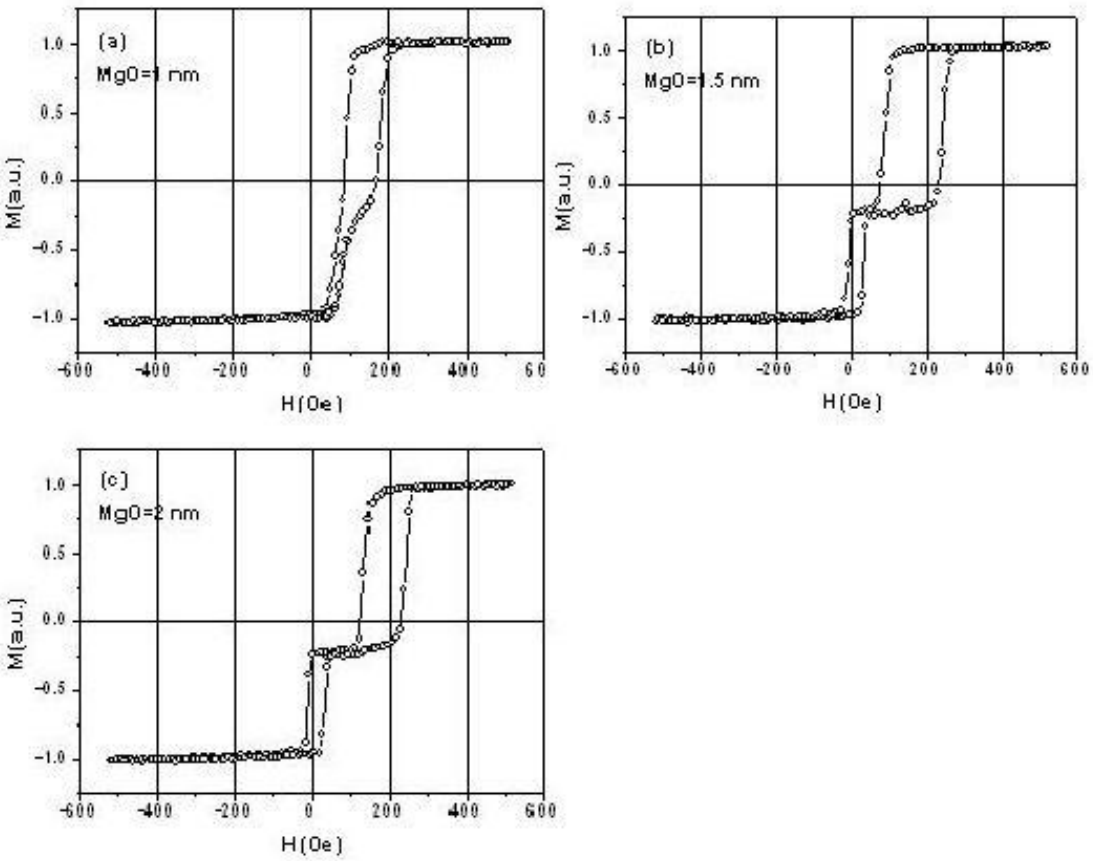

Fig. 6.1. MH loops of MTJ stacks Ta/CuN/Ta/CoFeB/MgO (t=1 nm, 1.5 nm, and 2 nm)/CoFe/IrMn/Ta with different MgO thickness. (a) MgO=1 nm; (b) MgO=1.5 nm; and (c) MgO= 2nm.

For commercial applications, the resistance-area product (RA) of the MTJ device is an important parameter and lower RA is preferred. RA increases exponentially with the thickness of MgO [82]. While we do not discuss much about the RA in this thesis, MgO of 2 nm-thick has been accepted in the following MTJ deposition.

6.2 Effect of bottom electrode material on TMR of top pinned MTJs

The atomically smooth interface of an MTJ stack should start from the bottom electrode and therefore the choice of the bottom electrode material is important in determining the roughness of the thin films deposited subsequently.

Top pinned MTJ films SiO_2/electrode/CoFeB (3 nm)/MgO (2 nm)/CoFe (4 nm)/IrMn (5nm)/Ta (5 nm) with electrode material of Ta (5 nm)/Cu (30 nm)/Ta (5 nm) and Ta (5 nm)/CuN (30 nm)/ (5 nm) were deposited by the Nordiko 9550. We assume the very thin top layers will follow the roughness of the underneath layer although there may be a little change.

The CuN films were deposited by sputtering the Cu target in a mixture of nitrogen and Ar gas. The ratio of the gas flow rate of N_2 and Ar is 1:20 controlled by two mass flow controllers, in which the gas flow is 20 sccm for Ar and 1 sccm for N_2. We aimed to reduce the roughness of Cu by introducing a minimal amount of N_2. An excessive amount of N_2 introduced in the Cu could change the electric properties the Cu. For example, Cu_3N is an insulator according to theoretical calculations [114] and experiments [115; 116], while Cu_4N is believed to be a conductor or semiconductor [114].

The effect of annealing temperature on roughness has also been studied. Roughness of the annealed Ta (5nm)/Cu (30nm)/Ta (5nm) and Ta (5nm)/CuN (30nm)/Ta (5nm) were characterized by AFM. Fig. 6.2 shows a typical measured roughness of Ta/Cu/Ta (a) and Ta/CuN/Ta (b) annealed at 350 ºC for one hour. It can be seen that the average roughness (Ra) of Ta/Cu/Ta is 0.9 nm as shown in Fig. 6.2(a), and by introducing 1sccm N_2, the Ra for Ta/CuN has been dramatically reduced to 0.37 nm. From this point, CuN has better roughness than Cu. All the MTJ samples were prepared on the CuN bottom electrode deposited with this condition.

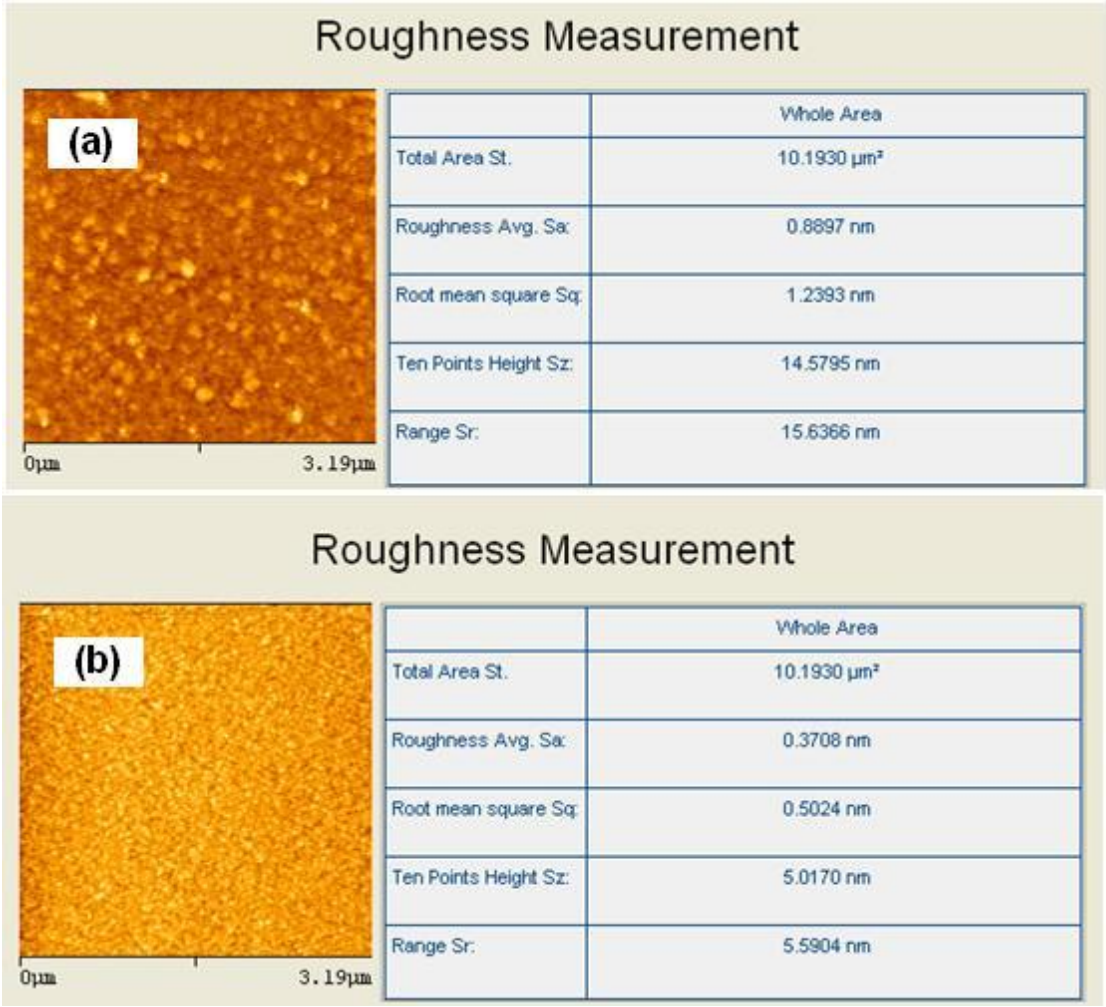

Fig. 6.2. Roughness measured by AFM for (a), Ta (5 nm)/Cu (30nm)/Ta (5nm); and (b), Ta (5 nm)/CuN (30 nm)/Ta (5nm) annealed at 350 °C for 1 hour.

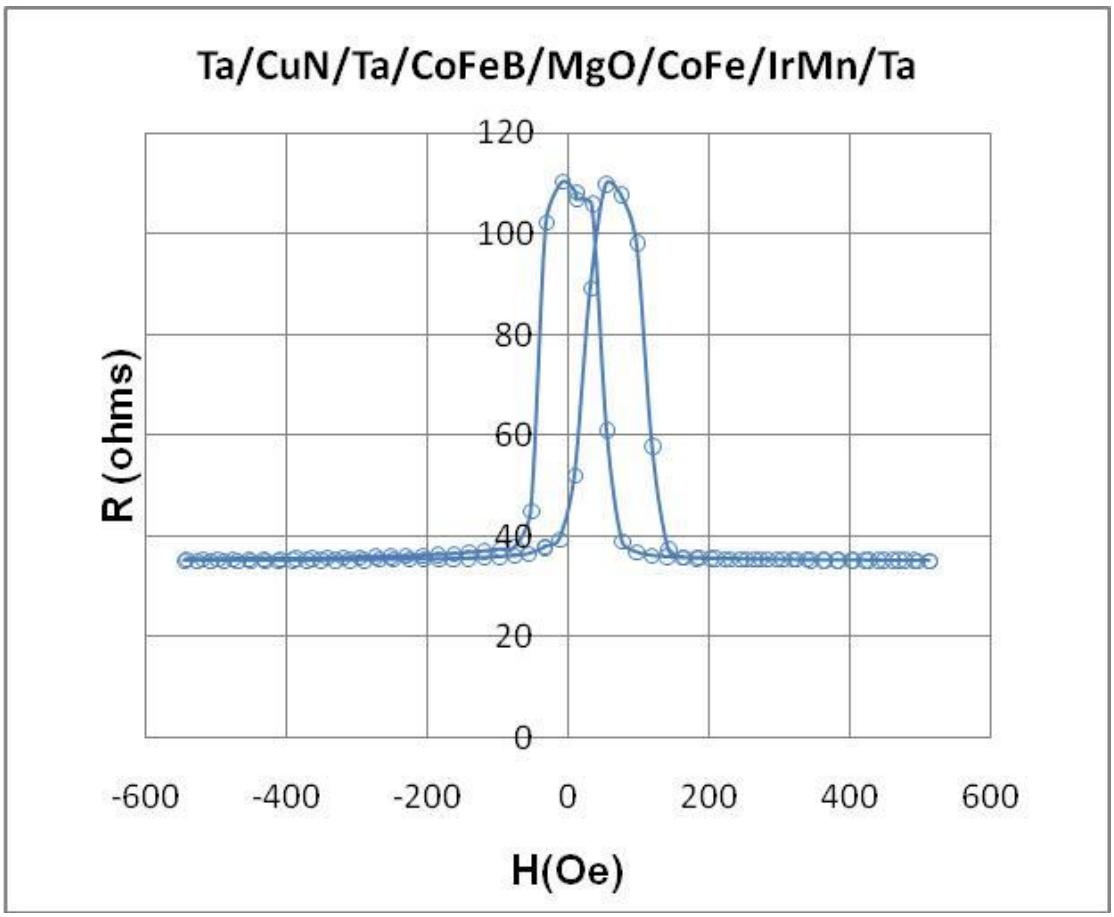

Fig. 6.3. A typical MR(H) curve for an MTJ with layer structure of Ta(5nm)/CuN(30nm)/Ta(5nm)/CoFeB(3nm)/MgO(2nm)/CoFe(4nm)/IrMn(5 nm)/Ta(5nm) and annealed at 350 ^{o}C for 1 hour.

The MTJ stacks were annealed at different temperatures and in an applied field of typically 5 kOe. MTJ devices were fabricated using the microfabrication process described earlier and TMR measured using the four-point probe systems. Fig 6.3 shows a typical MR (H) loop for MTJs with CuN bottom electrode and annealed at 350 ℃ for 1 hour. The dependence of TMR on T_A is also shown in Fig. 6.4. Here we used the best value in each annealing temperature to repesent the TMR value, which probably is the limit we can get based on the equipment or process condition in our lab. For each sample, there are about 30 devices being measured. Some of the show very low TMR, probably due to the uniformity limitation of our miller. Others show lower TMR probably due to some contamination or shorting to the device as it is such a long and

complicated microfabrication process. The TMR ratio initially increases with the annealing temperature to a maximum value of 202% at T_A = 350 ^{o}C. At temperature above 350 ^{o}C, the TMR begins to decrease. Similar dependence of TMR on T_A has been observed by others [117]. The decrease in TMR at higher T_A is perhaps due to the elemental diffusion. The maximum TMR value obtained in this work is still considerably lower than the very higher values (up to 604%) obtained by others [29]. The parameters which may affect the TMR magnitude are numerous, including purity of the target materials, MgO target in particular, base vacuum pressure of the deposition tool, deposition conditions, top and bottom FM electrode materials and crystallographic texture, interface smoothness, the quality of the microfabrication process, and the magnetic field annealing conditions. Considerable work is still required in order to obtain the optimum TMR.

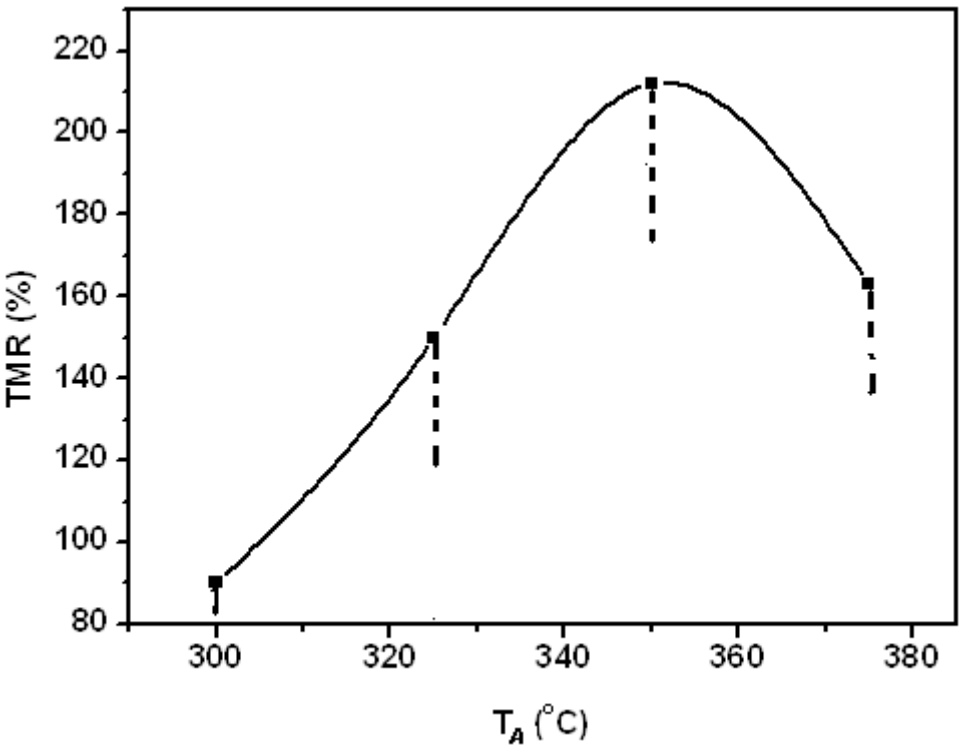

Fig. 6.4. T_A dependence of TMR for MTJs on CuN bottom electrode with layer structure Ta(5nm)/CuN(30nm)/Ta(5nm)/CoFeB(3nm)/MgO(2nm)/CoFe (4nm)/IrMn(5 nm)/Ta(5nm). The line was plotted based on the maximum TMR obtained from 30 devices measurements for each sample.

6.3 Bottom pinned IrMn/CoFeB/MgO/CoFeB films

6.3.1 MH loop of bottom pinned CoFeB/MgO/CoFeB

Based on the results on enhanced exchange bias in the bottom pinned Ta/CoFe/IrMn/CoFeB/Ta system, bottom pinned MTJ stack Ta (5nm)/CuN (30 nm)/Ta (5 nm)/CoFe (3.4nm)/IrMn (5 nm)/CoFeB (3 nm)/MgO (2 nm)/CoFeB (3nm)/Ta (5nm) was prepared by Nordiko 9550 tool. After deposition, magnetic field annealing was carried out for 1 hour at 350 ºC in a magnetic field of 5 kOe. Fig. 6.5 shows the MH loop of this sample measured by VSM. It can be seen that there are three loops and labeled as (a), (b) and (c). Loop (a) near zero field is the magnetization switching of the free layer 3nm CoFeB, loop (b) is seed layer CoFe in CoFe (3.4 nm)/IrMn with a H_{ex} of ~250 Oe and loop (c) is the bottom pined CoFeB in IrMn/CoFeB with a H_{ex} of ~600 Oe. The H_{ex} value of 600 Oe is less than the one obtained in the structure of Ta/CoFe/IrMn/CoFeB with similar thickness. This perhaps is due to the small changes in the interface roughness introduced by the CuN bottom electrode layers. However, the development of this MTJ structure, in particular the microfabrication and characterisation of the MTJs, was seriously delayed due to the breakdown of the cleanroom chiller, which made the Nordiko 9550 deposition tool unavailable for more than a year. By the time the new chiller was installed, my time at Plymouth had reached its end.

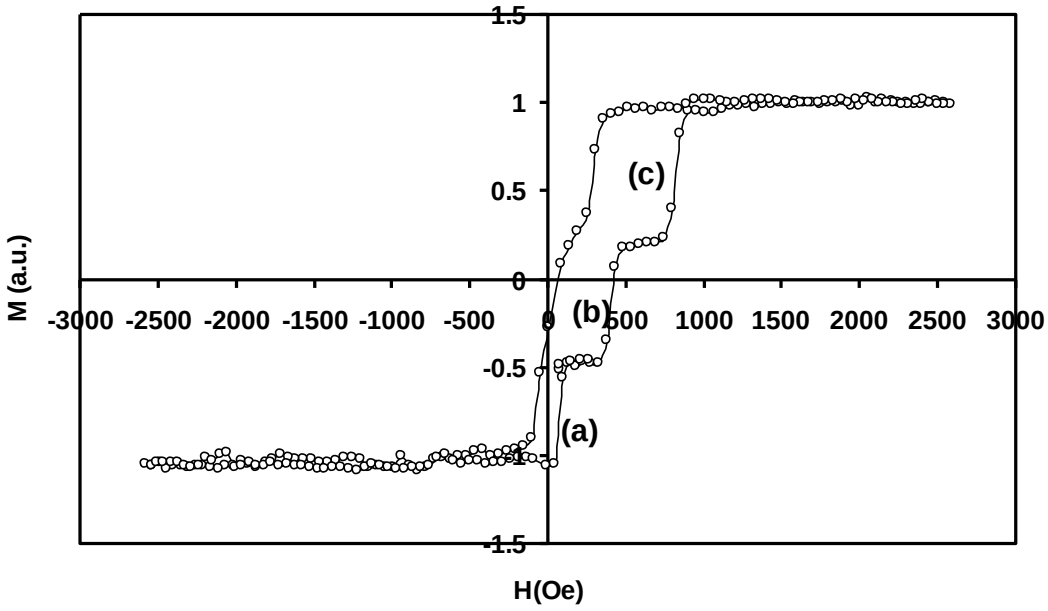

Fig. 6.5. MH loop for bottom pinned MTJ stack with layer structure of Ta(5nm)/CuN(30nm)/Ta(5nm)/CoFe(3.4nm)/IrMn(5nm)/CoFeB(3nm)/MgO(2nm)/ CoFeB(3nm)/Ta(5nm).

6.4 Summary

MTJs with a bottom CoFeB free layer, an MgO barrier and a CoFe/IrMn top pinned FM layers were prepared on CuN bottom electrode layers. The quality of the MTJ stacks was initially assessed by MH loops. The sputtering conditions for the deposition of smooth CuN bottom electrode layers were optimized with the assistance of AFM measurement of the surface roughness. MTJ devices were successfully fabricated and TMR, characterized. The effect of magnetic field annealing temperature on the TMR was studied. A maximum TMR of ~200% was obtained for top pinned MTJs with a 2 nm MgO barrier and annealed at 350 ℃ for 1 hour. Further work on bottom pinned MgO MTJs with CoFeB as both FM electrodes was carried out. The film stacks have been successfully characterized by VSM, which showed clear magnetic switching of each individual layers. However, more work is required for the optimization of the film deposition, device fabrication and characterization.

7 Conclusions and future work

The thin film deposition and device fabrication processes of magnetic tunnel junctions and their exchange bias systems have been studied in this work using two commercial spintronic deposition systems, the Aviza StratIon *fxP* ion beam deposition tool and the Nordiko 9550 PVD tool, together with photolithographic microfabrication techniques and a wide range of nano-scale, magnetic and magneto-transport characterisation techniques such as AFM, SEM, VSM, four-point probe, high resolution cross-sectional TEM and XMCD.

The film deposition and microfabrication processes were optimised when the Nordiko 9550 machine was installed. Two key progresses have been made - the deposition conditions to obtain blister-free films after annealing and the process conditions and techniques for the complete removal of photo-resist after ion milling.

By participating in the DTI MNT project, the author has contributed to the development of the process conditions for the deposition of the MTJs and their associated magnetic layers. The PtMn/CoFe exchange bias systems were systematically studied with magnetic field annealing and VSM MH loop characterization. Exchange bias field of up to 650 Oe was obtained for the Ta (10 nm)/ PtMn (20 nm)/ CoFe (3 nm)/Ta (10 nm) stack after magnetic field annealing at 300 ^{o}C for 2 hours. The photolithographic and ion milling processes for the microfabrication of the MTJs with an Al-O barrier layer was developed and TMR of these devices were successfully measured using the four-point probe system.

Bottom pinned exchange bias systems of IrMn/CoFe and IrMn/CoFeB with CoFe seed layer were studied. Enhanced exchange anisotropy was obtained from samples with

IrMn/CoFeB annealed at 350 °C. The enhancement of H_{ex} is accompanied by a moderate increase in H_c. Cross-sectional HRTEM shows that FM and AFM layers were polycrystalline and textured [110] for CoFe and CoFeB, and [111] for IrMn, respectively. Element specific XMCD spectrum showed a much enhanced uncompensated interfacial spins for IrMn/CoFeB sample with the largest exchange bias field, which may explain the interfacial magnetic origin of the enhanced anisotropy. A quantitative correlation between the XMCD signal strength and the exchange anisotropy constant J_k was observed.

MTJs with a bottom CoFeB free layer, an MgO barrier and a CoFe/IrMn top pinned FM layers were prepared on CuN bottom electrode layers. The quality of the MTJ stacks was initially assessed by MH loops. The sputtering conditions for the deposition of smooth CuN bottom electrode layers were optimized with the assistance of AFM measurement of the surface roughness. MTJ devices were successfully fabricated and TMR, characterized. The effect of magnetic field annealing temperature on the TMR was studied. A maximum TMR of ~200% was obtained for top pinned MTJs with a 2 nm MgO barrier and annealed at 350 ℃ for 1 hour. Further work on bottom pinned MgO MTJs with CoFeB as both FM electrodes was carried out. The film stacks have been successfully characterized by VSM, which showed clear magnetic switching of each individual layers.

This project has successfully demonstrated that the Nordiko 9550 is capable of producing good quality spintronic devices, such as MTJs. As this is the only device scale spintronic deposition tool in a UK university, it has huge potential for research in future spintronic devices. One of the immediate future works is the completion of the fabrication and characterization of the bottom pinned MgO MTJs with CoFeB as both

FM electrodes. Better TMR results are expected due to the stronger exchange bias field of the system, the smoother interfaces and potentially better crystallographic orientation and match between the two electrodes which will facilitate the better coherent tunneling. Other novel spintronic devices, such as spin transistors, may be further developed by employing the coherent tunnelling devices.

List of References

[1] H. Bethe, Zur Theorie der Metalle. Zeitschrift für Physik A Hadrons and Nuclei 71 (1931) 205.

[2] P. Weiss, L'hypothèse du champ moléculaire et la propriété ferromagnétique Journal de Physique 6 (1907) 661.

[3] http://www.fy.chalmers.se/edu/lab/labpm/em4_magnetic_hysteresis.pdf.

[4] H. Nalwa, Handbook of Thin Films, Five-Volume Set, Academic Press, 2002, pp. 520.

[5] J.F.J.a.A.R.W. V. L. Moruzzi, Calculated Electronic Properties of Metals (Pergamon, New York, 1978).

[6] K. Charles, Introduction to Solid State Physics, Wiley, New York, 1996.

[7] R. Meservey, and P.M. Tedrow, Spin-polarized electron tunneling. Physics Reports 238 (1994) 173.

[8] S. Parkin, Xin Jiang, Kaiser, C., Panchula, A., Roche, K., Samant, M. , Magnetically engineered spintronic sensors and memory. Proceedings of IEEE 91 (2003) 661.

[9] L. Hodges, H. Ehrenreich, and N.D. Lang, Interpolation Scheme for Band Structure of Noble and Transition Metals: Ferromagnetism and Neutron Diffraction in Ni. Physical Review 152 (1966) 505.

[10] K. Matsuda, A. Kamijo, T. Mitsuzuka, and H. Tsuge, Exchange-biased magnetic tunnel junctions fabricated with in situ natural oxidation. Journal of Applied Physics 85 (1999) 5261.

[11] I. Giaever, Energy Gap in Superconductors Measured by Electron Tunneling. Physical Review Letters 5 (1960) 147.

[12] B.D. Josephson, Possible new effects in superconductive tunnelling. Physics Letters 1 (1962) 251.

[13] J. Clarke, SQUIDs. Scientific American 271 (1994) 46.

[14] P.M. Tedrow, and R. Meservey, Spin-Dependent Tunneling into Ferromagnetic Nickel. Physical Review Letters 26 (1971) 192.

[15] F. Pérez-Willard, J.C. Cuevas, C. Sürgers, P. Pfundstein, J. Kopu, M. Eschrig, and H.v. Löhneysen, Determining the current polarization in Al/Co nanostructured point contacts. Physical Review B 69 (2004) 140502.

[16] R.J. Soulen, Jr., J.M. Byers, M.S. Osofsky, B. Nadgorny, T. Ambrose, S.F. Cheng, P.R. Broussard, C.T. Tanaka, J. Nowak, J.S. Moodera, A. Barry, J.M.

Coey, nbsp, and D, Measuring the Spin Polarization of a Metal with a Superconducting Point Contact. Science 282 (1998) 85.

[17] M. Julliere, Tunneling between ferromagnetic films. Physics Letters A 54 (1975) 225.

[18] A. Schuhl, and D. Lacour, Spin dependent transport: GMR & TMR. Comptes Rendus Physique 6 (2005) 945.

[19] D. L. Mills, and J.A.C. Bland, Nanomagnetism: Ultrathin Films, Multilayers and Nanostructures, ELSEVIER B. V., Amsterdam, 2006.

[20] T. Miyazaki, and N. Tezuka, Giant magnetic tunneling effect in Fe/Al2O3/Fe junction. Journal of Magnetism and Magnetic Materials 139 (1995) L231.

[21] J.S. Moodera, L.R. Kinder, T.M. Wong, and R. Meservey, Large Magnetoresistance at Room Temperature in Ferromagnetic Thin Film Tunnel Junctions. Physical Review Letters 74 (1995) 3273.

[22] Dexin Wang, C. Nordman, J.M. Daughton, Zhenghong Qian, and J. Fink, 70% TMR at room temperature for SDT sandwich junctions with CoFeB as free and reference Layers. Magnetics, IEEE Transactions on 40 (2004) 2269.

[23] J. Mathon, and A. Umerski, Theory of tunneling magnetoresistance of an epitaxial Fe/MgO/Fe(001) junction. Physical Review B 63 (2001) 220403.

[24] W.H. Butler, X.G. Zhang, T.C. Schulthess, and J.M. MacLaren, Spin-dependent tunneling conductance of Fe|MgO|Fe sandwiches. Physical Review B 63 (2001) 054416.

[25] S. Yuasa, T. Nagahama, A. Fukushima, Y. Suzuki, and K. Ando, Giant room-temperature magnetoresistance in single-crystal Fe/MgO/Fe magnetic tunnel junctions. Nat Mater 3 (2004) 868.

[26] D.D. Djayaprawira, K. Tsunekawa, M. Nagai, H. Maehara, S. Yamagata, N. Watanabe, S. Yuasa, Y. Suzuki, and K. Ando, 230% room-temperature magnetoresistance in CoFeB/MgO/CoFeB magnetic tunnel junctions. Applied Physics Letters 86 (2005) 092502.

[27] Y.M. Lee, J. Hayakawa, S. Ikeda, F. Matsukura, and H. Ohno, Giant tunnel magnetoresistance and high annealing stability in CoFeB/MgO/CoFeB magnetic tunnel junctions with synthetic pinned layer. Applied Physics Letters 89 (2006) 042506.

[28] S. Ikeda, J. Hayakawa, Y.M. Lee, F. Matsukura, and H. Ohno, Dependence of tunnel magnetoresistance on ferromagnetic electrode materials in MgO-barrier

magnetic tunnel junctions. Journal of Magnetism and Magnetic Materials 310 (2007) 1937.

[29] S. Ikeda, J. Hayakawa, Y. Ashizawa, Y.M. Lee, K. Miura, H. Hasegawa, M. Tsunoda, F. Matsukura, and H. Ohno, Tunnel magnetoresistance of 604% at 300 K by suppression of Ta diffusion in CoFeB/MgO/CoFeB pseudo-spin-valves annealed at high temperature. Applied Physics Letters 93 (2008) 082508.

[30] Y. Sakuraba, M. Hattori, M. Oogane, Y. Ando, H. Kato, A. Sakuma, T. Miyazaki, and H. Kubota, Giant tunneling magnetoresistance in Co_2MnSi/Al--O/Co_2MnSi magnetic tunnel junctions. Applied Physics Letters 88 (2006) 192508.

[31] M. Bowen, M. Bibes, A. Barthelemy, J.P. Contour, A. Anane, Y. Lemaitre, and A. Fert, Nearly total spin polarization in $La_{2/3}Sr_{1/3}MnO_3$ from tunneling experiments. Applied Physics Letters 82 (2003) 233.

[32] H. Ibach, Hans Luth, Solid-State Physics, An Introduction to Principles of Materials Science, Springer-Verlag, Aachen, Germany, 2009.

[33] S. Yuasa, and D.D. Djayaprawira, Giant tunnel magnetoresistance in magnetic tunnel junctions with a crystalline MgO(001) barrier. Journal of Physics D: Applied Physics 40 (2007) R337.

[34] S. Yuasa, T. Nagahama, and Y. Suzuki, Spin-Polarized Resonant Tunneling in Magnetic Tunnel Junctions. Science 297 (2002) 234.

[35] T. Nagahama, S. Yuasa, E. Tamura, and Y. Suzuki, Spin-Dependent Tunneling in Magnetic Tunnel Junctions with a Layered Antiferromagnetic Cr(001) Spacer: Role of Band Structure and Interface Scattering. Physical Review Letters 95 (2005) 086602.

[36] Y.M. Lee, J. Hayakawa, S. Ikeda, F. Matsukura, and H. Ohno, Effect of electrode composition on the tunnel magnetoresistance of pseudo-spin-valve magnetic tunnel junction with a MgO tunnel barrier. Applied Physics Letters 90 (2007) 212507.

[37] P. Mavropoulos, N. Papanikolaou, and P.H. Dederichs, Complex Band Structure and Tunneling through Ferromagnet /Insulator /Ferromagnet Junctions. Physical Review Letters 85 (2000) 1088.

[38] J.P. Velev, K.D. Belashchenko, D.A. Stewart, M. van Schilfgaarde, S.S. Jaswal, and E.Y. Tsymbal, Negative Spin Polarization and Large Tunneling Magnetoresistance in Epitaxial Co|SrTiO3|Co Magnetic Tunnel Junctions. Physical Review Letters 95 (2005) 216601.

[39] E.M. Willams, Design and Analysis of Magnetoresistive Recording Heads, John Wiley, 2001.

[40] W.H. Meiklejohn, and C.P. Bean, New Magnetic Anisotropy. Physical Review 102 (1956) 1413.

[41] W.H. Meiklejohn, and C.P. Bean, New Magnetic Anisotropy. Physical Review 105 (1957) 904.

[42] W.H. Meiklejohn, Exchange Anisotropy---A Review. Journal of Applied Physics 33 (1962) 1328.

[43] A.E. Berkowitz, and J.H. Greiner, Exchange Anisotropy and Strain Interactions in the Ni-NiO System. Journal of Applied Physics 36 (1965) 3330.

[44] T.J. Moran, J.M. Gallego, and I.K. Schuller, Increased exchange anisotropy due to disorder at permalloy/CoO interfaces. Journal of Applied Physics 78 (1995) 1887.

[45] D.T. Pierce, J. Unguris, R.J. Celotta, and M.D. Stiles, Effect of roughness, frustration, and antiferromagnetic order on magnetic coupling of Fe/Cr multilayers. Journal of Magnetism and Magnetic Materials 200 (1999) 290.

[46] J. Unguris, R.J. Celotta, D.T. Pierce, and J.A. Stroscio, Biquadratic exchange coupling in Fe/Cr/Fe(100) and Fe/Ag/Fe(100) thin film sandwiches. Journal of Applied Physics 73 (1993) 5984.

[47] J. Unguris, R.J. Celotta, and D.T. Pierce, Oscillatory magnetic coupling in Fe/Ag/Fe(100) sandwich structures. Journal of Magnetism and Magnetic Materials 127 (1993) 205.

[48] M. Tsunoda, T. Nakamura, M. Naka, S. Yoshitaki, C. Mitsumata, and M. Takahashi, Soft x-ray magnetic circular dichroism study of Mn--Ir/Co--Fe bilayers with giant exchange anisotropy. Applied Physics Letters 89 (2006) 172501.

[49] W.J. Antel, T. Hughes, H. Laidler, P.J. Doherty, and A. Johnston, XMCD measurements of exchange biased PtMn/Co bilayers. Journal of Magnetism and Magnetic Materials 242-245 (2002) 961.

[50] H. Ohldag, T.J. Regan, J. Stöhr, A. Scholl, F. Nolting, J. Lüning, C. Stamm, S. Anders, and R.L. White, Spectroscopic Identification and Direct Imaging of Interfacial Magnetic Spins. Physical Review Letters 87 (2001) 247201.

[51] H. Ohldag, A. Scholl, F. Nolting, E. Arenholz, S. Maat, A.T. Young, M. Carey, and J. Stöhr, Correlation between Exchange Bias and Pinned Interfacial Spins. Physical Review Letters 91 (2003) 017203.

[52] M. Tsunoda, S. Yoshitaki, Y. Ashizawa, C. Mitsumata, T. Nakamura, H. Osawa, T. Hirono, D.Y. Kim, and M. Takahashi, Uncompensated antiferromagnetic spins at the interface in Mn--Ir based exchange biased bilayers, 10th JOINT MMM/INTERMAG CONFERENCE, AIP, Baltimore, Maryland (USA), 2007, pp. 09E510-3.

[53] S. Bruck, G. Schutz, E. Goering, X. Ji, and K.M. Krishnan, Uncompensated Moments in the MnPd/Fe Exchange Bias System. Physical Review Letters 101 (2008) 126402.

[54] S. Roy, C. Sanchez-Hanke, S. Park, M.R. Fitzsimmons, Y.J. Tang, J.I. Hong, D.J. Smith, B.J. Taylor, X. Liu, M.B. Maple, A.E. Berkowitz, C.C. Kao, and S.K. Sinha, Evidence of modified ferromagnetism at a buried Permalloy/CoO interface at room temperature. Physical Review B (Condensed Matter and Materials Physics) 75 (2007) 014442.

[55] S. Roy, M.R. Fitzsimmons, S. Park, M. Dorn, O. Petracic, I.V. Roshchin, Z.-P. Li, X. Batlle, R. Morales, A. Misra, X. Zhang, K. Chesnel, J.B. Kortright, S.K. Sinha, and I.K. Schuller, Depth Profile of Uncompensated Spins in an Exchange Bias System. Physical Review Letters 95 (2005) 047201.

[56] M.R. Fitzsimmons, S. Roy, B.J. Kirby, S. Park, I.V. Roshchin, Z.-P. Li, J.B. Kortright, S.K. Sinha, and I.K. Schuller, Combined magnetic X-ray and polarized neutron reflectivity study of the origins of exchange bias in the Co / FeF2 system. Superlattices and Microstructures 41 (2007) 109.

[57] M.R. Fitzsimmons, B.J. Kirby, S. Roy, Z.-P. Li, I.V. Roshchin, S.K. Sinha, and I.K. Schuller, Pinned magnetization in the antiferromagnet and ferromagnet of an exchange bias system. Physical Review B (Condensed Matter and Materials Physics) 75 (2007) 214412.

[58] E. Blackburn, C. Sanchez-Hanke, S. Roy, D.J. Smith, J.I. Hong, K.T. Chan, A.E. Berkowitz, and S.K. Sinha, Pinned Co moments in a polycrystalline permalloy/CoO exchange-biased bilayer. Physical Review B (Condensed Matter and Materials Physics) 78 (2008) 180408.

[59] G. Salazar-Alvarez, J.J. Kavich, J. Sort, A. Mugarza, S. Stepanow, A. Potenza, H. Marchetto, S.S. Dhesi, V. Baltz, B. Dieny, A. Weber, L.J. Heyderman, J. Nogues, and P. Gambardella, Direct evidence of imprinted vortex states in the antiferromagnet of exchange biased microdisks. Applied Physics Letters 95 (2009) 012510.

[60] P. Miltényi, M. Gierlings, J. Keller, B. Beschoten, G. Güntherodt, U. Nowak, and K.D. Usadel, Diluted Antiferromagnets in Exchange Bias: Proof of the Domain State Model. Physical Review Letters 84 (2000) 4224.

[61] J. Keller, P. Miltényi, B. Beschoten, G. Güntherodt, U. Nowak, and K.D. Usadel, Domain state model for exchange bias. II. Experiments. Physical Review B 66 (2002) 014431.

[62] U. Nowak, K.D. Usadel, J. Keller, P. Miltényi, B. Beschoten, and G. Güntherodt, Domain state model for exchange bias. I. Theory. Physical Review B 66 (2002) 014430.

[63] G. Vallejo Fernandez, M. Vopsaroiu, S. Manzoor, and K. O'Grady, Exchange bias control in CoFe/IrMn via grain size control, Magnetics Conference, 2005. INTERMAG Asia 2005. Digests of the IEEE International, 2005, pp. 2031-2032.

[64] N.N. Shams, M.T. Rahman, and C.-H. Lai, Defect mediated tuning of exchange bias in IrMn/CoFe nanostructure, PROCEEDINGS OF THE 53RD ANNUAL CONFERENCE ON MAGNETISM AND MAGNETIC MATERIALS, AIP, Austin, Texas (USA), 2009, pp. 07D722-3.

[65] J.-I. Hong, T. Leo, D.J. Smith, and A.E. Berkowitz, Enhancing Exchange Bias with Diluted Antiferromagnets. Physical Review Letters 96 (2006) 117204.

[66] C. Papusoi, J. Hauch, M. Fecioru-Morariu, and G. Guntherodt, Tuning the exchange bias of soft metallic antiferromagnets by inserting nonmagnetic defects. Journal of Applied Physics 99 (2006) 123902.

[67] J. Nogués, and I.K. Schuller, Exchange bias. Journal of Magnetism and Magnetic Materials 192 (1999) 203.

[68] R. Jungblut, R. Coehoorn, M.T. Johnson, J.a. de Stegge, and A. Reinders, Orientational dependence of the exchange biasing in molecular-beam-epitaxy-grown $Ni_{80}Fe_{20}/Fe_{50}Mn_{50}$ bilayers (invited), 38th Annual Conference on Magnetism and Magnetic Materials, AIP, Minneapolis, Minnesota (USA), 1994, pp. 6659-6664.

[69] A.P. Malozemoff, Random-field model of exchange anisotropy at rough ferromagnetic-antiferromagnetic interfaces. Physical Review B 35 (1987) 3679.

[70] L. Neel, Ann. Phys., Paris, 1967, pp. 61.

[71] D. Mauri, H.C. Siegmann, P.S. Bagus, and E. Kay, Simple model for thin ferromagnetic films exchange coupled to an antiferromagnetic substrate. Journal of Applied Physics 62 (1987) 3047.

[72] K. Takano, R.H. Kodama, A.E. Berkowitz, W. Cao, and G. Thomas, Interfacial Uncompensated Antiferromagnetic Spins: Role in Unidirectional Anisotropy in Polycrystalline Ni81Fe19/CoO Bilayers. Physical Review Letters 79 (1997) 1130.

[73] W.L. Roth, Magnetic Structures of MnO, FeO, CoO, and NiO. Physical Review 110 (1958) 1333.

[74] B. chapman, Glow Discharge Process, John Wiley & sons, 1980.

[75] J.A. Thornton, The microstructure of sputter-deposited coatings. Journal of Vacuum Science & Technology A: Vacuum, Surfaces, and Films 4 (1986) 3059.

[76] J.A. Thornton, Evaporation and sputtering, Noyes Publications, 1984.

[77] A.G. Spencer, C.A. Bishop, and R.P. Howson, The design and performance of planar magnetron sputtering cathodes. Vacuum 37 (1987) 363.

[78] D.M. Mattox, Handbook of physical vapor deposition (PVD) processing, Noyes Publications, 1998.

[79] Y.S. Choi, K. Tsunekawa, Y. Nagamine, and D. Djayaprawira, Transmission electron microscopy study on the polycrystalline CoFeB/MgO/CoFeB based magnetic tunnel junction showing a high tunneling magnetoresistance, predicted in single crystal magnetic tunnel junction. Journal of Applied Physics 101 (2007) 013907.

[80] S. Yuasa, Y. Suzuki, T. Katayama, and K. Ando, Characterization of growth and crystallization processes in CoFeB/MgO/CoFeB magnetic tunnel junction structure by reflective high-energy electron diffraction. Applied Physics Letters 87 (2005) 242503.

[81] T. Dimopoulos, G. Gieres, J. Wecker, N. Wiese, and M.D. Sacher, Thermal annealing of junctions with amorphous and polycrystalline ferromagnetic electrodes. Journal of Applied Physics 96 (2004) 6382.

[82] Jun Hayakawa, Shoji Ikeda, Fumihiro Matsukura, H. Takahashi, and a.H. Ohno, Dependence of Giant Tunnel Magnetoresistance of Sputtered CoFeB/MgO/CoFeB Magnetic Tunnel Junctions on MgO Barrier Thickness and Annealing Temperature. Japanese Journal of Applied Physics 44 (2005) L587.

[83] Shoji Ikeda, Jun Hayakawa, Young Min Lee, Ryutaro Sasaki, Toshiyasu Meguro, F. Matsukura., and a.H. Ohno, Dependence of Tunnel Magnetoresistance in MgO Based Magnetic Tunnel Junctions on Ar Pressure during MgO Sputtering. Japanese Journal of Applied Physics 44 (2005) L1442.

[84] G. Shmalz, Uber Glatte und Eberheit als Physikalisches und physiologishes Problem, Verin Detscher Ingenieure, 1929, pp. 1461.

[85] http://www.chem.ucalgary.ca/research/groups/faridehj/xas.pdf.

[86] http://www-ssrl.slac.stanford.edu/stohr/xmcd.htm.

[87] R. Nakajima, J. Stöhr, and Y.U. Idzerda, Electron-yield saturation effects in L-edge x-ray magnetic circular dichroism spectra of Fe, Co, and Ni. Physical Review B 59 (1999) 6421.

[88] P. Willmott, An Introduction to Synchrotron Radiation: Techniques and Applications, John Wiley and Sons, 2011.

[89] C.T. Chen, Y.U. Idzerda, H.J. Lin, N.V. Smith, G. Meigs, E. Chaban, G.H. Ho, E. Pellegrin, and F. Sette, Experimental Confirmation of the X-Ray Magnetic Circular Dichroism Sum Rules for Iron and Cobalt. Physical Review Letters 75 (1995) 152.

[90] http://en.wikipedia.org/wiki/X-ray_magnetic_circular_dichroism.

[91] L.B. Valdes, Resistivity measurements on Germanium for Transistors. Proceedings of Institute of Radio Engineers 43 (1954) 8.

[92] http://www.avizatechnology.com/investors/releases.html.

[93] G.W. Anderson, Y. Huai, and M. Pakala, Spin-valve thermal stability: The effect of different antiferromagnets. Journal of Applied Physics 87 (2000) 5726.

[94] J.P. Nozieres, S. Jaren, Y.B. Zhang, K. Pentek, A. Zeltser, P. Wills, and V.S. Speriosu, Correlation between lifetime and blocking temperature distribution in spin-valve structures. Journal of Applied Physics 87 (2000) 6609.

[95] J.P. Nozieres, S. Jaren, Y.B. Zhang, A. Zeltser, K. Pentek, and V.S. Speriosu, Blocking temperature distribution and long-term stability of spin-valve structures with Mn-based antiferromagnets. Journal of Applied Physics 87 (2000) 3920.

[96] C. Ji, P. Ladwig, R. Ott, Y. Yang, J. Yang, Y. Chang, E. Linville, J. Gao, and B. Pant, An investigation of phase transformation behavior in sputter-deposited PtMn thin films. JOM Journal of the Minerals, Metals and Materials Society 58 (2006) 50.

[97] R.F.M. R. F. C. Farrow, S. Gider, A. C. Marley, S. S. P. Parkin, and D. Mauri, MnxPt1−x: A new exchange bias material for Permalloy. Journal of Applied Physics 81 (1997) 4986.

[98] K.M. Krishnan, C. Nelson, C.J. Echer, R.F.C. Farrow, R.F. Marks, and A.J. Kellock, Exchange biasing of permalloy films by Mn[sub x]Pt[sub 1 - x]: Role

of composition and microstructure, The 7th joint MMM-intermag conference on magnetism and magnetic materials, AIP, San Francisco, California (USA), 1998, pp. 6810-6812.

[99] P.P.F. M. Rickart, I. G. Trindade, N. P. Barradas, E. Alves, M. Salgueiro, N. Muga, J. Ventura, J. B. Sousa, G. Proudfoot, D. Pearson, and M. Davis Exchange bias of MnPt/CoFe films prepared by ion beam deposition. Journal of Applied Physics 95 (2004) 6317.

[100] Y.K. Kim, S.-R. Lee, S.A. Song, G.-S. Park, H.S. Yang, and K.I. Min, Magnetoresistance and interlayer diffusion in PtMn spin valves upon postdeposition annealing, AIP, 2001, pp. 6907-6909.

[101] S. Cardoso, C. Cavaco, R. Ferreira, L. Pereira, M. Rickart, P.P. Freitas, N. Franco, J. Gouveia, and N.P. Barradas, Characterization of CoFeB electrodes for tunnel junctions. Journal of Applied Physics 97 (2005) 10C916.

[102] M. Fecioru-Morariu, G. Guntherodt, M. Ruhrig, A. Lamperti, and B. Tanner, Exchange coupling between an amorphous ferromagnet and a crystalline antiferromagnet. Journal of Applied Physics 102 (2007) 053911.

[103] C.Y. You, H.S. Goripati, T. Furubayashi, Y.K. Takahashi, and K. Hono, Exchange bias of spin valve structure with a top-pinned $Co_{40}Fe_{40}B_{20}$/IrMn. Applied Physics Letters 93 (2008) 012501.

[104] M. Fujita, K. Yamano, A. Maeda, T. Tanuma, and M. Kume, Exchange coupling in spin-valve structures containing amorphous CoFeB. Journal of Applied Physics 81 (1997) 4909.

[105] T. Feng, and J.R. Childress, Fabrication of exchange-biased spin valves with CoFeB amorphous layers. Journal of Applied Physics 85 (1999) 4937.

[106] M. Mao, S. Funada, C.-Y. Hung, T. Schneider, M. Miller, H.-C. Tong, C. Qian, and L. Miloslavsky, Enhanced exchange biasing in ion-beam sputtered bottom spin valve films. Magnetics, IEEE Transactions on 35 (1999) 3913.

[107] R.M. Oksuzoglu, M. Yildirim, H. Cinar, E. Hildebrandt, and L. Alff, Effect of Ta buffer and NiFe seed layers on pulsed-DC magnetron sputtered $Ir_{20}Mn_{80}/Co_{90}Fe_{10}$ exchange bias. Journal of Magnetism and Magnetic Materials 323 (2011) 1827.

[108] D.N.H. Nam, W. Chen, K.G. West, D.M. Kirkwood, J. Lu, and S.A. Wolf, Propagation of exchange bias in CoFe/FeMn/CoFe trilayers. Applied Physics Letters 93 (2008) 152504.

[109] G. Vallejo-Fernandez, T. Dimopoulos, M. Ruehrig, and K. O'Grady, Annealing effect on thermal stability and microstructure in IrMn/$Co_{60}Fe_{20}B_{20}$ bilayers. Journal of Magnetism and Magnetic Materials 310 (2007) e786.

[110] K.-i. Imakita, M. Tsunoda, and M. Takahashi, Thickness dependence of exchange anisotropy of polycrystalline Mn_3Ir/Co-Fe bilayers, 49th Annual Conference on Magnetism and Magnetic Materials, AIP, Jacksonville, Florida (USA), 2005, pp. 10K106-3.

[111] M. Tsunoda, K.-i. Imakita, M. Naka, and M. Takahashi, L12 phase formation and giant exchange anisotropy in Mn_3Ir/Co-Fe bilayers. Journal of Magnetism and Magnetic Materials 304 (2006) 55.

[112] A. Sakuma, K. Fukamichi, K. Sasao, and R.Y. Umetsu, First-principles study of the magnetic structures of ordered and disordered Mn-Ir alloys. Physical Review B 67 (2003) 024420.

[113] H. Takahashi, K. Yohei, T. Masakiyo, N. Tetsuya, K. Kenji, S. Akimasa, and T. Migaku, Uncompensated antiferromagnetic moments in Mn-Ir/FM (FM = Ni-Co, Co-Fe, Fe-Ni) bilayers: Compositional dependence and its origin. Journal of Applied Physics 110 (2011) 123920.

[114] U. Hahn, and W. Weber, Electronic structure and chemical-bonding mechanism of Cu_3N, Cui_3NPd, and related Cu(I) compounds. Physical Review B 53 (1996) 12684.

[115] F. Fendrych, L. Soukup, L. Jastrabik, M. Sicha, Z. Hubicka, D. Chvostova, A. Tarasenko, V. Studnicka, and T. Wagner, Cu_3N films prepared by the low-pressure r.f. supersonic plasma jet reactor: Structure and optical properties. Diamond and Related Materials 8 (1999) 1715.

[116] J. Wang, J.T. Chen, X.M. Yuan, Z.G. Wu, B.B. Miao, and P.X. Yan, Copper nitride (Cu_3N) thin films deposited by RF magnetron sputtering. Journal of Crystal Growth 286 (2006) 407.

[117] J. Hayakawa, S. Ikeda, Y.M. Lee, F. Matsukura, and H. Ohno, Effect of high annealing temperature on giant tunnel magnetoresistance ratio of CoFeB/MgO/CoFeB magnetic tunnel junctions. Applied Physics Letters 89 (2006) 232510.

APPENDIX 1: List of abbreviations

AFM	anti-ferromagnetic
AFM	atomic force microscopy
bcc	body-centered cubic
DI	de-ionized
DOS	density of states
EBL	electron beam lithography
EDS	energy dispersive x-ray spectroscopy
HAADF	High angle annular dark field
fcc	face-centered cubic
fct	face centered tetragonal
FM	ferromagnetic
HRTEM	high resolution transmission electron microscopy
IBD	ion beam deposition
IPA	isopropyl alcohol
LCP	left circularly polarized
MIS	metal-insulator-superconductor
MR	magneto-resistance
MRAM	magnetic random access memory
MTJ	magnetic tunnel junction
PVD	physical vapor deposition
RCP	right circularly polarized
SAED	selected area electron diffraction
sc	simple cubic
SIS	superconductor-insulator-superconductor

SIF	superconductor-insulator-ferromagnet
SIMS	secondary ion mass spectrometry
ST	substrate target
SEM	scanning electron microscopy
TEM	transmission electron microscopy
TEY	total electrons yield

APPENDIX 2: List of publications

Journal Articles:

1. **Y. Du**, G. Pan, R. Moate, H. Ohldag, A. Kovacs and A. Kohn, "Enhanced exchange anisotropy in IrMn/CoFeB systems and its correlation with uncompensated interfacial spins", Appl. Phys. Lett. 96, 222503 (2010)
2. Y. Zhou, D. Stickler, **Y. Du**, E. Ahmad, Z. Lu, R. Frömter, H. P. Oepen, D. Wilton and G. Pan, "Size effect on magnetic switching and interlayer magnetostatic coupling in spin-valve nanorings exchange-biased by synthetic antiferromagnets", IEEE Trans. Magn. 47, 214(2011)
3. Z. Lu, Y. Zhou, **Y. Du**, D. Wilton, and G. Pan, "Current-assisted magnetization switching in a mesoscopic NiFe ring with nanoconstrictions of a wire", Appl. Phys. Lett., 88, 142507(2006)
4. Z. Lu, Y. Zhou, **Y. Du**, D. Wilton, R. Moate and G. Pan, "Magnetization switching in a mesoscopic NiFe ring with nanoconstrictions of wire", J. Appl. Phys., 99, 08C506(2006)

Conference Posters/Presentations:

1. "Domain wall motion induced magnetisation reversal processes in NiFe nanodevices with different pinning sites", Y. Zhou, D. Stickler, **Y. Du**, E. Ahmad, Z. Lu, W. Li, H. P. Oepen, D. Wilton and G. Pan, session HQ-05, Intermag 2008, Madrid, Spain.
2. "Magnetotransport and current-induced domain wall displacement at the notches in a submicron pseudo-spin-valve stripe", Y. Zhou, Z. Lu, **Y. Du**, D. Wilton and G. Pan, session HQ-02, Intermag 2006, San Diego, USA.

3. "Current induced domain motion in synthetic spin valves", Z. Lu, Y. Zhou, **Y. Du**, D. Wilton and G. Pan, Accepted for presentation at session DC-11, Intermag 2006, San Diego, USA.

4. "Magnetisation switching in mesoscopic NiFe ring with nanoconstrictions of wire", Z. Lu, Yun. Zhou, **Y. Du**, D. Wilton and G. Pan, session BB-07, the 50th Annual Conference on Magnetism and Magnetic materials, San Jose, CA, Oct. 2005.

5. "Current induced domain wall displacement in synthetic spin valves", Z. Lu, Y. Zhou, **Y. Du**, D. Wilton, R. Moate and G. Pan, MISM 2005, Moscow, June 2005